

國立臺灣大學電機資訊學院電機工程學系



博士論文

Department of Electrical Engineering

College of Electrical Engineering and Computer Science

National Taiwan University

Doctoral Dissertation

以利薩茹層疊式局部掃描實現高速大範圍
之原子力顯微鏡

Based on Lissajous Hierarchical Local Scan to Realize High
Speed and Large Range Atomic Force Microscopy

吳俊緯

Jim-Wei Wu

指導教授：傅立成 博士

Advisor: Li-Chen Fu, Ph.D.

中華民國一〇二年十一月

November 2013

摘要



原子力顯微鏡是一種非常有用的精密量測儀器，此儀器具有奈米等級的解析能力並適用於導體與非導體樣本且不受使用環境所限制，為目前不可或缺的微奈米量測工具。然而，傳統原子力顯微鏡所使用的掃描方式，在軌跡上容易造成掃描器的機械共振問題，且無法去除不必要的掃描區域，因此，對於一個大範圍與高解析度的影像要求，必須要以一個更長的掃描時間來達成，無法給予一個有效率的掃描表現，為目前原子力顯微鏡應用上的主要缺陷。在本論文中，將以自行開發之原子力顯微鏡系統從三個不同的層面來克服上述問題。

首先，我們採用順滑式利薩茹軌跡並搭配適合此軌跡的先進控制法則，可在不引起水平掃描器震動的情況下提高掃描速率與精度。其次，針對此順滑軌跡的路徑特徵，撰寫掃描路徑演算法則，並利用探針橫過樣本後迴授的高度資訊去除不必要的掃描區域，藉此減少掃描所需時間。最後，考慮樣本表面形貌的變化情形，在表面劇烈變化的地方提供一個更高解析度的掃描，藉此改善掃描影像的品質，從實際的掃描應用可以證實上述方法之效果。

關鍵字: 原子力顯微鏡; 利薩茹掃描軌跡; 內部模型原理; 互補式順滑模式控制; 類神經網路; 適應性控制

Abstract



Atomic force microscopy (AFM) is a very useful measurement instrument. It can scan the conductive and nonconductive samples and without any restriction in the environments of application. Therefore, it has become an indispensable micro/nano scale measurement tool. However, because the raster scan method of the conventional AFM could easily induce the mechanical resonance of the scanner and cannot remove the scan area which is not our interest. Under a requirement for a large range and high resolution sample image which however needs excessive scan time, how to overcome such hurdles becomes the main challenge for AFM applications. In this thesis, we try to approach and resolve these problems with self-designed AFM system from three aspects.

First, we use a smooth Lissajous scan trajectory, and apply an advanced controller to realize this kind of trajectory. Since vibration of the lateral scanner will not be induced easily, the scan rate and scan accuracy can thus be increased accordingly. Next, based on the path characteristics of the smooth Lisajous trajectory, we propose a suitable scan algorithm, which initially employs the information on the sample height which the probe is traversing the scan area, and then select the sub-areas of our interest for next phase scan. Overall, such two phase scan reduce the scan time. Finally,

considering the varying of sample topography, we provide higher resolution scan on the severe area to improve the scan performance so that a better scan image can be obtained.

To validate the effectiveness of the proposed scan methodology, we have conducted extensive experiments and promising results have been acquired.

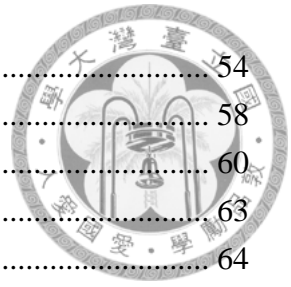
Keywords: Atomic force microscopy; Lissajous scan trajectory; internal model principle; complementary sliding mode control; neural network; adaptive control.

Table of Content



摘要	i
Abstract.....	ii
Table of Content	iv
Table of Acronyms.....	vii
List of Figures.....	viii
List of Tables	xii
Chapter 1 Introduction	1
1.1 Motivation	1
1.2 Literature Survey	3
1.2.1 Large range AFM.....	3
1.2.2 High speed AFM.....	6
1.2.3 Local scan AFM	10
1.3 Contribution.....	13
1.4 Thesis Organization	15
Chapter 2 Preliminary	17
2.1 Fundamentals of Electromagnetic Actuation.....	17
2.1.1 Lorentz force principle	18
2.1.2 Properties of permanent magnet	19
2.2 Fundamentals of Piezoelectric Actuation	23
2.2.1 Piezoelectric effect	23
2.2.2 Hysteresis phenomenon	24
2.3 Basic Principles of CD/DVD Pickup Head	26
2.3.1 Sensing methodology	28
2.3.2 Focusing and tracking actuator.....	30
2.4 Operation Principle of AFM System	31
2.5 Internal Model Principle (IMP)	34
Chapter 3 System Design and Dynamic Modeling	37
3.1 AFM Measuring System.....	38
3.1.1 Probe oscillating system	39
3.1.2 Probe dynamic detection	41
3.2 AFM Scanning System.....	42
3.3 Dynamic Modeling and Formulation	44
3.3.1 Modeling of xy-hybrid scanner	45
3.3.2 AFM scanning disturbance.....	50

3.3.3	System identification	54
3.4	Laser Interferometer Sensing System.....	58
3.5	Hardware Equipments	60
Chapter 4	Lissajous Hierarchical Local Scan (LHLS).....	63
4.1	Scan Trajectory Analysis	64
4.1.1	Conventional raster scan trajectory	65
4.1.2	Smooth Lissajous scan trajectory	67
4.2	Lissajous Scan Trajectory Formulation	68
4.2.1	Trajectory fundamental principle	68
4.2.2	Mapping Lissajous points to raster points	73
4.3	Lissajous Hierarchical Local Scan Algorithm	76
4.3.1	First layer scan.....	78
4.3.2	Second or higher layer scan.....	84
Chapter 5	Controller Design	89
5.1	Scan Trajectory Assignment for xy -Hybrid Scanner	89
5.2	IMP based Adaptive Complementary Sliding Mode Control.....	91
5.2.1	Problem formulation.....	92
5.2.2	Control algorithm	94
5.2.3	Stability analysis.....	97
5.3	IMP based Neural Network Complementary Sliding Mode Control	103
5.3.1	Problem formulation.....	104
5.3.2	Control algorithm	107
5.3.3	Stability analysis.....	110
Chapter 6	Experiments	115
6.1	Experimental Setup	115
6.2	Hysteresis Compensation	117
6.3	Scan Trajectory Tracking.....	118
6.3.1	Triangular waveform with PI control	118
6.3.2	Cosine waveform with PI control.....	120
6.3.3	Cosine waveform with IMP based NNCSMC.....	121
6.4	Numerical Simulation of Lissajous Hierarchical Local Scan.....	123
6.5	AFM Scanning Application	129
6.5.1	Standard Grating with Raster Scan.....	129
6.5.2	Standard Grating with Lissajous Scan.....	131
6.5.3	Human blood cells with Lissajous Hierarchical Local Scan	133
Chapter 7	Conclusions	139
Reference	141



List of Publication 146

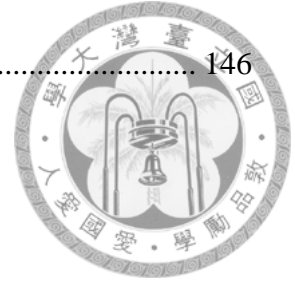


Table of Acronyms



AFM	atomic force microscopy
PPF	positive position feedback
IMP	internal model principle
CD/DVD	Compact disk/ digital versatile disc
PUH	pick-up head
FES	focusing error signal
PZT	plumbum zirconate titanate
DDS	direct digital synthesized
FES	focusing error signal
OEIC	opto-electric integrated circuit
MIMO	multi-input multi-output
DMT	Derjaguin–Muller–Toporov
MMA	MEMS Motion Analyzer
HIL	hardware-in-the-loop
ACSMC	adaptive complementary sliding mode control
NNCSMC	neural network complementary sliding model control
RMS	root-mean-square
2D	three-dimensions (three-dimensional)
3D	three-dimensions (three-dimensional)

List of Figures

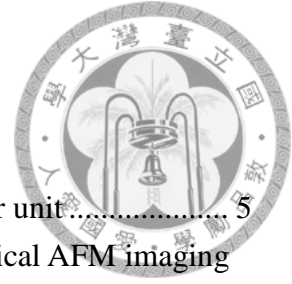


Fig. 1-1 Photograph of the AFM tip placed over the sample-holder unit.....	5
Fig. 1-2 Photograph of homemade enlarged sample holder for optical AFM imaging	5
Fig. 1-3 The concept of a novel metrological AFM.....	5
Fig. 1-4 The photo of a metrological large-range AFM system	6
Fig. 1-5 The Closed-loop system with the integral controller to implement in a piezoelectric tube	7
Fig. 1-6 Experimental configuration of the AFM system for generating scan images by using PPF controller.....	8
Fig. 1-7 The developed scanner by piezo-support mechanism (a) Schematic model and (b) the photograph.....	8
Fig. 1-8 Three-axis serial-kinematic nano-positioning stage.....	9
Fig. 1-9 The cycloid-like scan trajectory	9
Fig. 1-10 The constant linear velocity spiral scan trajectory	9
Fig. 1-11 (a) The Lissajous scan trajectory (b) Time-lapse sequences of the raster and Lissajous imaging processes.....	10
Fig. 1-12 (a) The strategy of local scan based online sensing for cell cutting (b) AFM image before cell cutting (c) AFM image after cell cutting.....	12
Fig. 1-13 (a) Local raster scan and (b) raster scan images of a sinusoidal test curve	12
Fig. 1-14 (a) Local scan of nanoparticles (b) The local-scan-after-operation results of a nanoparticle.....	12
Fig. 1-15 (a) Parallel imaging/nanomanipulation scheme (b) Lateral push results with parallel manipulation	13
Fig. 2-1 Lorentz force principle	19
Fig. 2-2 $B-H$ curve of a typical ferromagnetic material	21
Fig. 2-3 (a) Piezoelectric effect (b) Reverse piezoelectric effect	24
Fig. 2-4 Hysteresis loop	26
Fig. 2-5 Photograph of used CD/DVD pickup head and the total mass is 18g.....	27
Fig. 2-6 Inside buildup and working principle of a typical CD/DVD pickup head ...	30
Fig. 2-7 (a) Off focus, $FES < 0$. (b) On focus, $FES = 0$. (c) Off focus, $FES > 0$. (d) Linear region of FES.....	31
Fig. 2-8 The schematic diagram of contact mode and tapping mode	32
Fig. 2-9 The block diagram of a tapping mode AFM system	32

Fig. 2-10 The schematic diagram of internal model principle based control.....	35
Fig. 3-1 The block diagram of our proposed AFM system.....	38
Fig. 3-2 Photography of the AFM probe.....	39
Fig. 3-3 The CAD figure of the probe oscillating system.....	40
Fig. 3-4 The probe of NanoWorld PointProbe Type-NCHR.....	40
Fig. 3-5 The CAD figure of the mechanism of the AFM sensing system.....	41
Fig. 3-6 The AFM scanning system.....	43
Fig. 3-7 The schematic diagram of the piezoelectric scanner's operation principle..	43
Fig. 3-8 Reality photograph of the piezoelectric xy -scanner.....	44
Fig. 3-9 The schematic diagram of xy -hybrid scanner in x -axis.....	45
Fig. 3-10 The dynamic modeling of parallel structure.....	47
Fig. 3-11 The tip and sample interaction is considered as the disturbance to the stage	51
Fig. 3-12 Geometry employed in the Derjarguin approximation.....	51
Fig. 3-13 The Bode diagram of xy -electromagnetic scanner in x -axis.....	55
Fig. 3-14 The Bode diagram of xy -electromagnetic scanner in y -axis.....	56
Fig. 3-15 The Bode diagram of xy -piezoelectric scanner in x -axis.....	57
Fig. 3-16 The Bode diagram of xy -piezoelectric scanner in y -axis.....	57
Fig. 3-17 The configuration of laser interferometer sensing system.....	59
Fig. 3-17 The schematic diagram of beam path in 10706B interferometer.....	60
Fig. 3-17 The diagram of system hardware structure.....	62
Fig. 4-1 The diagram of raster scan trajectory (a) the signal waveforms of x and y axes (b) the raster scan trajectory by combining both signals.....	65
Fig. 4-2 The frequency spectrum of a triangular waveform with $A = 1$, $f = 220$ Hz	66
Fig. 4-3 The frequency spectrum of a cosine waveform with $A = 1$, $f = 220$ Hz.	68
Fig. 4-4 Schematic of the Lissajous-scan trajectory with $f_x = 25$ Hz, $f_y = 24$ Hz, and A_x, A_y are 1, (a) The first quartered period. (b) The second quartered period. (c) A square formed scan trajectory can be fully generated by a half-period Lissajous scan trajectory.....	70
Fig. 4-5 Each pitch points of the Lissajous scan trajectory with $n = 2$	72
Fig. 4-6 Maximum scan pitch of the Lissajous scan trajectory with $n = 6$	73
Fig. 4-7 Schematic diagram of placing the Lissajous points on top of the raster points	74
Fig. 4-8 The flow chart of the Lissajous hierarchical Local scan method.....	77
Fig. 4-9 (a) The schematic diagram of the Lissajous first layer scan, (b) the amplified diagram of (a) in the nearest sample, (c) the M -th scan line of nearest sample	

with height information.	80
Fig. 4-10 The height variations by calculating the sample grating weighting.....	86
Fig. 4-11 (a) Calculate all sample grating weighting and (b) generate the sub-block by region growing.....	88
Fig. 5-1 The schematic diagram of internal model principle based adaptive complementary sliding mode control.	94
Fig. 5-2 The schematic diagram of internal model principle based neural network complementary sliding mode control	107
Fig. 5-3 Structure of the radial basis function neural network.....	108
Fig. 6-1 Realization of the proposed AFM system	116
Fig. 6-2 The measured noises of laser interferometer and strain gauge sensor	116
Fig. 6-3 Fig. 6-3 The hysteresis effect of xy -piezoelectric scanner in x -axis (a) without control (b) with NNCSMC	117
Fig. 6-4 The hysteresis effect of xy -piezoelectric scanner in y -axis (a) without control (b) with NNCSMC	118
Fig. 6-5 Triangular waveform tracking performance with frequency of (a) 10 Hz, (b) 50 Hz, and (c) 100 Hz using PI control.....	120
Fig. 6-6 Cosine waveform tracking performance with frequency of (a) 10 Hz, (b) 50 Hz, and (c) 100 Hz using PI control	121
Fig. 6-7 Cosine waveform tracking performance with frequency of (a) 10 Hz, (b) 50 Hz, and (c) 100 Hz using IMP based NNCSMC	122
Fig. 6-8 The overall structure of the scan sample (a) 2D image (b) 3D image.....	124
Fig. 6-9 The results of first layer scan.....	125
Fig. 6-10 The results of second layer scan (a) 2D Lissajous scan pattern (b) 3D image.....	127
Fig. 6-11 The results of third layer scan (a) 2D Lissajous scan pattern (b) 3D image	128
Fig. 6-12 The dimensions of standard grating	129
Fig. 6-13 Scanned images of standard grating with raster scan and PI control at different scan frequencies	130
Fig. 6-14 Scanned images of standard grating with Lissajous scan and the proposed IMP based controllers at different scan frequencies	132
Fig. 6-15 (a) First layer scan result with a large scan range of $90\ \mu\text{m}\times 90\ \mu\text{m}$ (b) partial enlarged in the scan area.....	134
Fig. 6-16 Decide the rectangular scan area in the interested samples by weighting	135
Fig. 6-17 AFM scanned image of human blood cells in 2D by the proposed Lissajous	

hierarchical local scan.....	136
Fig. 6-18 AFM scanned image of human blood cells in 3D by the proposed Lissajous	
hierarchical local scan.....	137



List of Tables

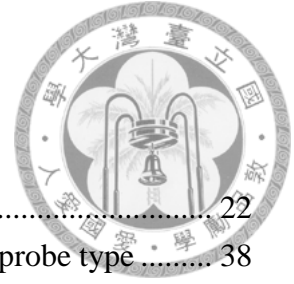


Table. 2-1 Specifications of NdFeB	22
Table. 3-1 Comparison between moving sample type and moving probe type	38
Table. 3-2 Specification of the probe used in the research	40
Table. 3-3 Specifications of the piezoelectric <i>xy</i> -scanners.....	44




Chapter 1

Introduction

1.1 Motivation


Bining *et al.* [1] invented atomic force microscopy (AFM) in 1986 for investigating conductive and non-conductive samples. It utilizes a probe with a sharp tip to scan the sample surface, and the operational principle of AFM is to keep the interaction signal between the sharp tip and the sample surface at a constant value. Compared with common optical microscopy [2], it does not provide an assisting light source and can precisely reconstruct three-dimensional sample's topography information with atomic-level resolution. Therefore, AFM has become an indispensable measurement instrument in many science field's applications [3], [4].

Conventionally, the measured image of the sample is generated by moving the horizontal position of the sample or the probe along a pre-defined raster trajectory, which is achieved with the lateral scanner to track a triangular waveform and staircase waveform. By measuring the interaction between probe tip and the sample surface, a pixel-by-pixel method can produce the AFM image. Since a triangular waveform signal



includes odd harmonics of the fundamental frequency [5], if we wish to track this trajectory ideally, an infinite bandwidth of lateral scanner will be required. However, it is impossible to achieve this requirement for all kinds of finite bandwidth scanners, because they are unable to avoid exciting the mechanical resonance. Generally, the scan speed of an acceptable AFM image under the raster scan is limited to about 1% of the scanner's resonance frequency [6]. Therefore, to select a good scan trajectory without inducing the mechanical vibration of the scanner will contribute to enhancement of the scan speed without sacrificing the image's quality. In addition, notice that the conventional scanning method requires the probe to scan the overall scan area over the sample with a constant velocity. However, for quite a few real AFM application their scan areas typically include some sub-areas which are not our interest and the varying of measured sample surface may not be identical. If those applications take the same scan speed and thus the identical scan pitch, either some unnecessary long time will be spent or a bad AFM image will be produced if the total scan time is upper bounded. In another word, conventional AFMs inevitably need to spend longer time in order to obtain a better AFM image, and this result will restrict the AFM applications in many scientific fields.

The aim of this thesis is to address the aforementioned issues from three aspects.




First, a smooth Lissajous scan trajectory is employed for AFM scan, which permits about a half-order increase in scan rate. Second, for the purpose of dealing with system parameters uncertainties, external disturbance, and hysteresis effect, two advanced controllers are designed so that the scan tip can track the Lissajous scan trajectory precisely. Finally, in order to remove the uninterested area and to achieve a higher resolution image for AFM, a new algorithm based on the characteristic of Lissajous trajectory is proposed. Specifically, by designing the Lissajous scan path and considering the sample's height information, we propose a hierarchical local scan method, which allows us to obtain higher image resolution without increasing the total scan time.

1.2 Literature Survey

Since the small scan range and long scan time of the AFM are the major limitations in many applications, there have been many researches dedicated to improving them. In this section, we will survey the state-of-the-art researches in three topics.

1.2.1 Large range AFM

In recent years, the AFM system with large scanning range has been investigated by



many researchers. In 2007, Sinno *et al.* [7] developed a homemade sample-holder unit, as shown in Fig. 1-1, which includes a coarse linear motor stage and a fine piezoelectric stage for nano-positioning in two dimensions with $1\text{ mm} \times 1\text{ mm}$ traveling range. In 2009, Brian [8] designed a long-range metrological atomic force microscope as shown in Fig. 1-2, which also integrates a motor for large range travelling and a precision piezoelectric actuation for coarse-to-fine motion resulting in a $40\text{ mm} \times 40\text{ mm}$ measurement volume. However, this AFM system has not been explicitly experimented to ours knowledge. In 2010, Werner *et al.* [9] developed a new metrological AFM instrument as shown in Fig. 1-3, which consists of a translation stage by using elastic straight guides and Lorentz actuators with a stroke of $1\text{ mm} \times 1\text{ mm}$, and a custom-designed AFM measurement head. However, only a small scale experiment was carried out to verify the capability of the proposed AFM systems. Furthermore, Dai *et al.* [10] developed a dual stage positioning system by integrating the coarse electro-dynamics motor and the fine piezoelectric stage, which is used as a large area scanning of the AFM with $25\text{ mm} \times 25\text{ mm} \times 5\text{ mm}$ traveling-range in 2009 as shown in Fig. 1-4. In 2012, Guo *et al.* [11] also used the same stage by applying the dual feedback strategy to control the two kinds of the driven actuators, in order to obtain better AFM scanning results in a large measuring range.

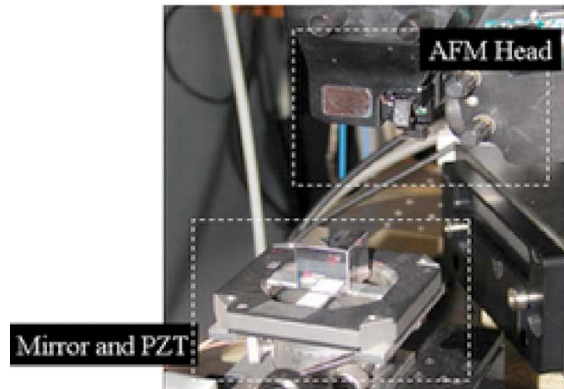


Fig. 1-1 Photograph of the AFM tip placed over the sample-holder unit

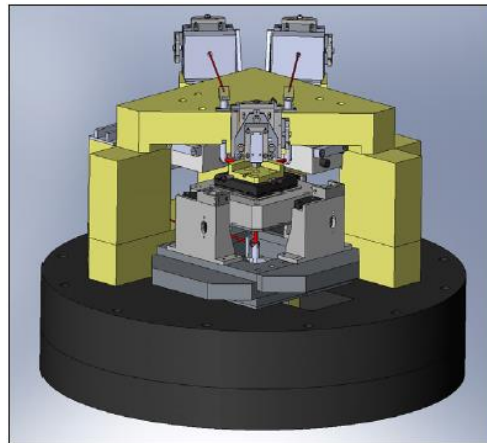


Fig. 1-2 Photograph of homemade enlarged sample holder for optical AFM imaging

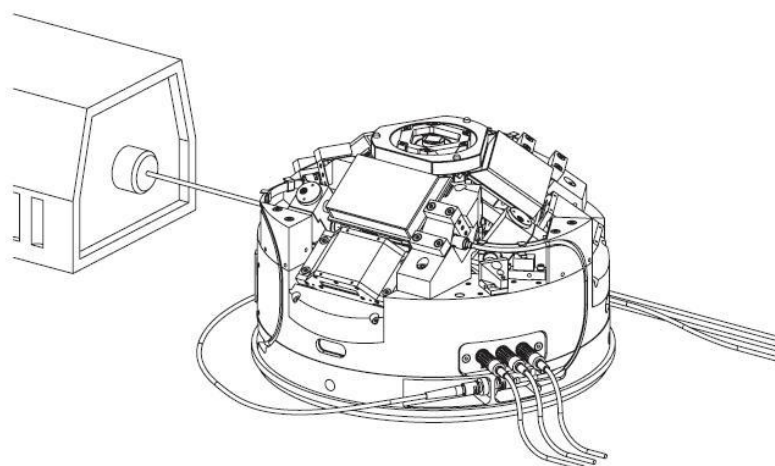


Fig. 1-3 The concept of a novel metrological AFM

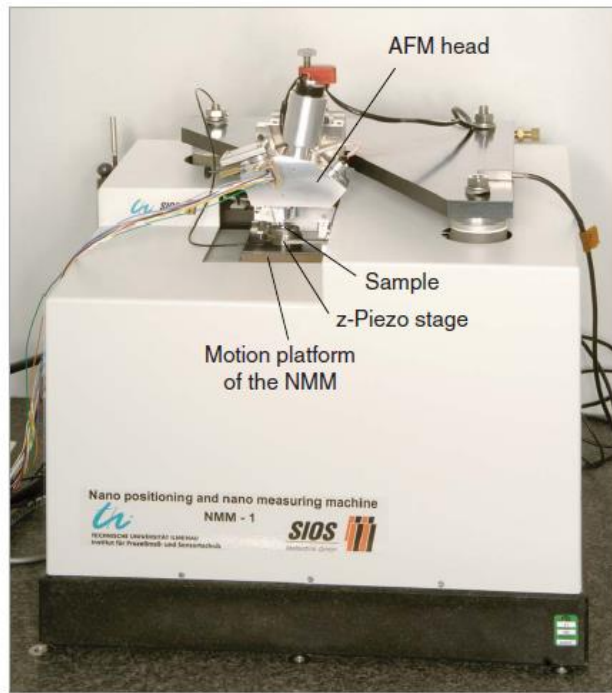


Fig. 1-4 The photo of a metrological large-range AFM system

1.2.2 High speed AFM

A variety of solutions have been proposed to increase the scan speed of AFM system. The first method is to employ feedback to improve the damping ratio of the AFM scanner. In 2008, Bhikkaji *et al.* [12] used an integral resonant control by damping the resonance of a piezoelectric tube to achieve fast tracking performance as shown in Fig. 1-5. In 2010, Yong *et al.* [13] designed a positive position feedback (PPF) controller by damping the scanner's resonance to obtain closed-loop images of a standard grating at 31 Hz scan rates as shown in Fig. 1-6. However, the scan speed of this method is limited based on the mechanical bandwidth of the scanner. In 2008, Fukuma *et al.* [14] developed



a piezo-support mechanism to offer the high resonance frequency of 540 kHz in the z -axis which is shown in Fig. 1-7. In 2011, Kenton *et al.* [15] developed a high-bandwidth three-axis serial-kinematic nano-positioning stage for application in a commercial AFM system, which can provide the scan speed up to a line rate of 7 kHz as shown in Fig. 1-8.

Another method for increasing the scan speed of AFM system employs non-raster scanning, by tracking smooth trajectories on x and y axes of the positioning stage. In 2010, Yong *et al.* [16] designed a smooth cycloid-like scan trajectory to allow higher scan speed instead of applying the raster scan method, as shown in Fig. 1-9. In 2010, Hung [17] realized the spiral trajectory scan with constant linear velocity's method, as shown in Fig. 1-10. In 2012, Tuma *et al.* [18] presented a smooth Lissajous scan trajectory for increasing the scan speed in AFM system. The main advantages of Lissajous trajectory are not only improving the scan speed of the image but also providing the preview result of the scanned area, as shown in Fig. 1-11.

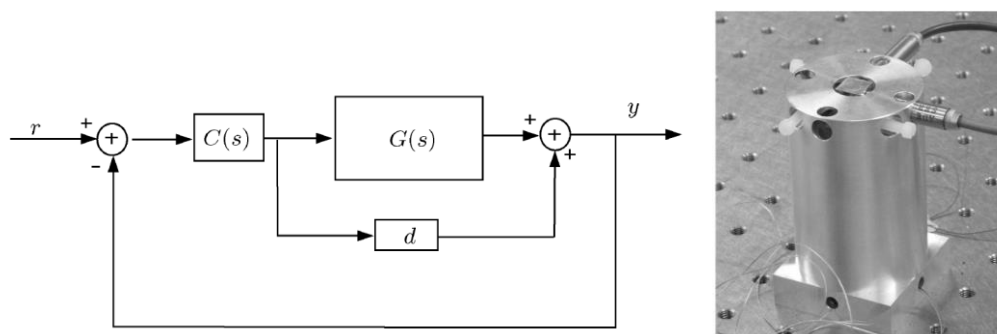


Fig. 1-5 The Closed-loop system with the integral controller to implement in a piezoelectric tube

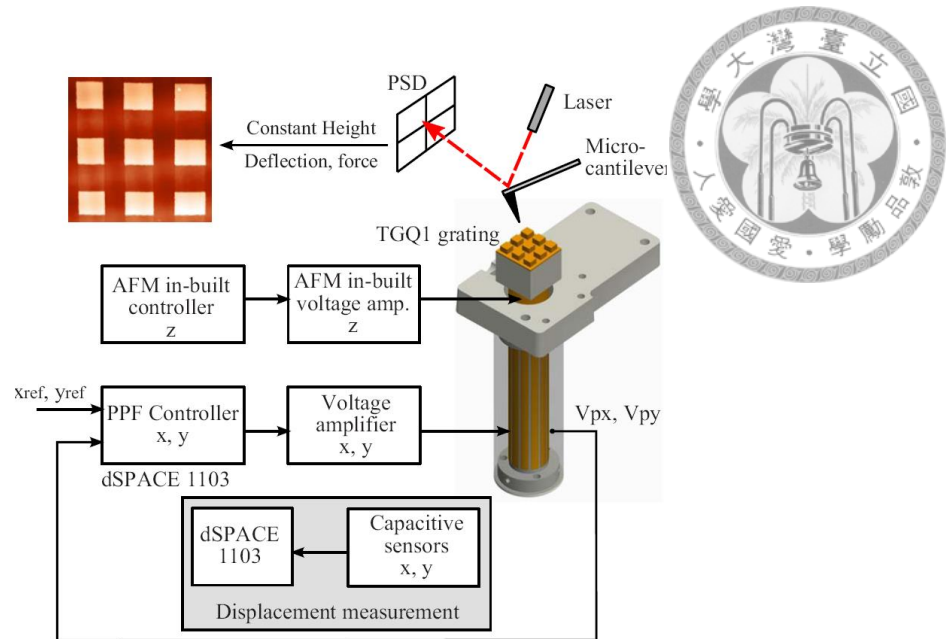


Fig. 1-6 Experimental configuration of the AFM system for generating scan images by using PPF controller

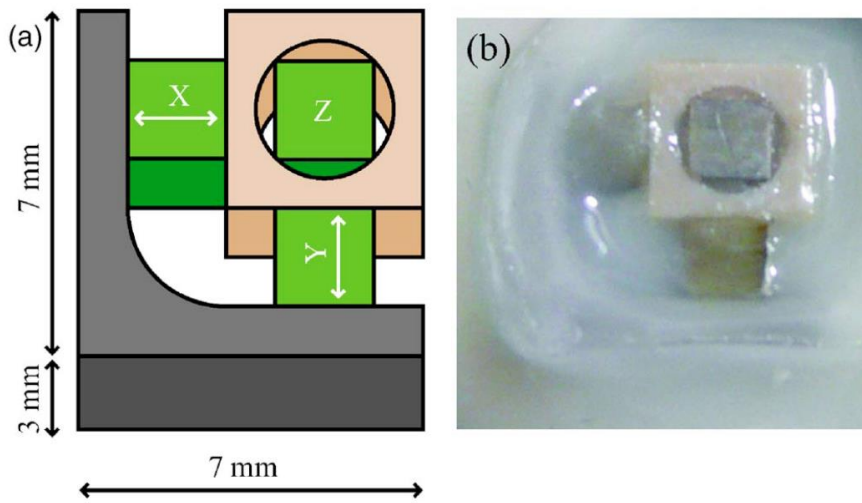


Fig. 1-7 The developed scanner by piezo-support mechanism (a) Schematic model and (b) the photograph

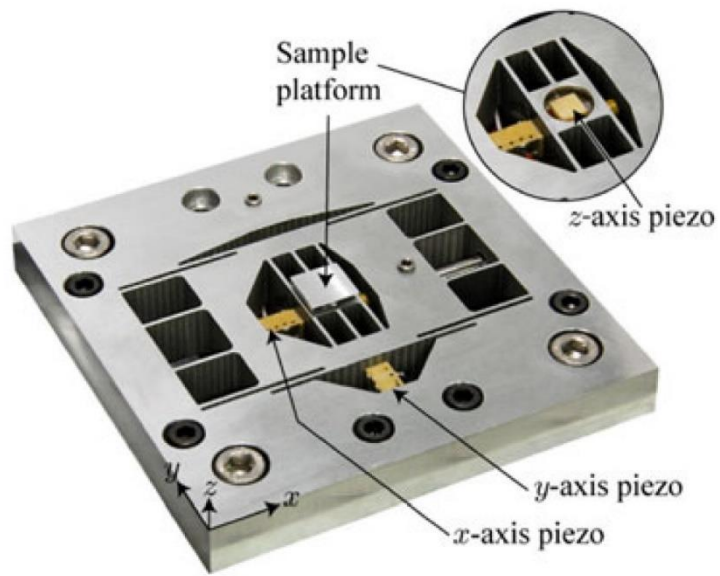


Fig. 1-8 Three-axis serial-kinematic nano-positioning stage

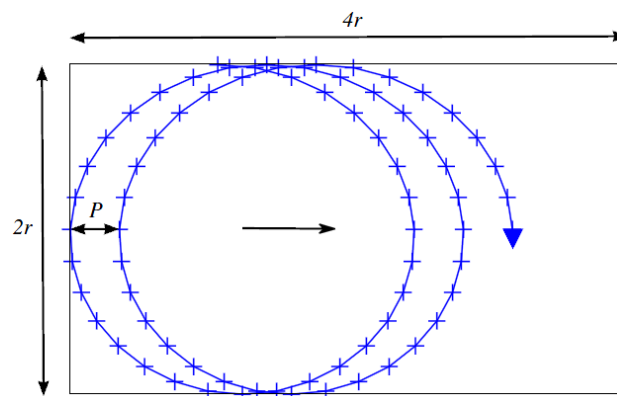


Fig. 1-9 The cycloid-like scan trajectory

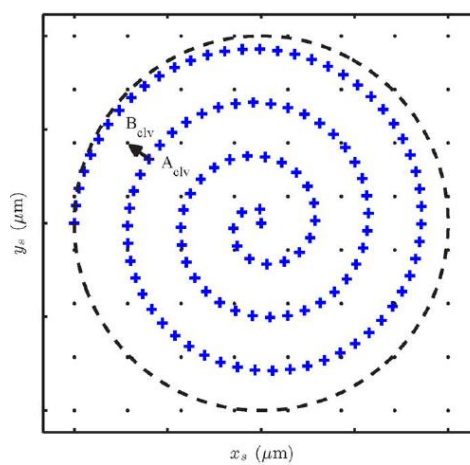


Fig. 1-10 The constant linear velocity spiral scan trajectory

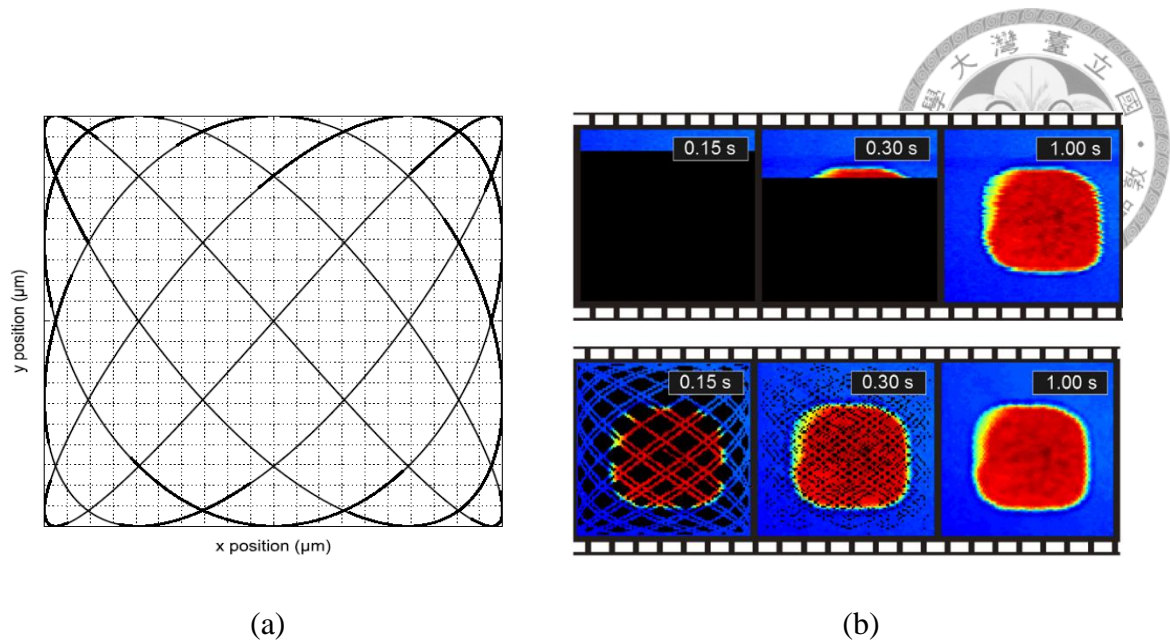



Fig. 1-11 (a) The Lissajous scan trajectory (b) Time-lapse sequences of the raster and Lissajous imaging processes

1.2.3 Local scan AFM

In many AFM applications, such as inspection of biological cells or measurement of nano material, if we can limit the scan region only to the interested area of samples, then such result will definitely shorten the overall scan time. As a result, the local scan AFM has become a new research topic in recent years. In 2010, Song *et al.* proposed an adaptive local scan strategy to provide online sensing for AFM based nano-manipulations [19]. The strategy of local scan based online sensing for cell cutting, as shown in Fig. 1-12. It is to scan the region of manipulation and provides visual feedback for identifying the actual surface topography during the process of manipulation. In 2011, Chang *et al.* presented a local raster scan algorithm for providing



high speed AFM imaging of biopolymers as shown in Fig. 1-13 [20]. This algorithm utilizes the measurement data of the AFM to operate the scanning tip to localize the scan area over the sample of interest in real time. The total scan time can be shortened by reducing the scan area of the sample. However, this local scan method can be used just for simple string-like sample. If the sample is too complex, this method tends to fail.

In 2012, Li *et al.* developed an algorithm incorporating a strategic local scan method to identify and eliminate the drift-induced distortion in the AFM image for nanoparticles [21]. In that research, the local scan method is used to find the center position of the nanoparticle with local scanning a pair of perpendicular lines across the sample as shown in Fig. 1-14. But this algorithm is applicable only for particle-like samples.

In 2012, Xie *et al.* proposed a high-efficiency parallel imaging/manipulation force microscopy [22], which is a two-tip configuration AFM as shown in Fig. 1-15. In that scheme, one tip is responsible for image scanning, and another one is performing the manipulation. In order to find the sample position and decide the manipulation direction quickly, the local scan method is executed by the manipulation tip at first, and then performing the predetermined manipulation.

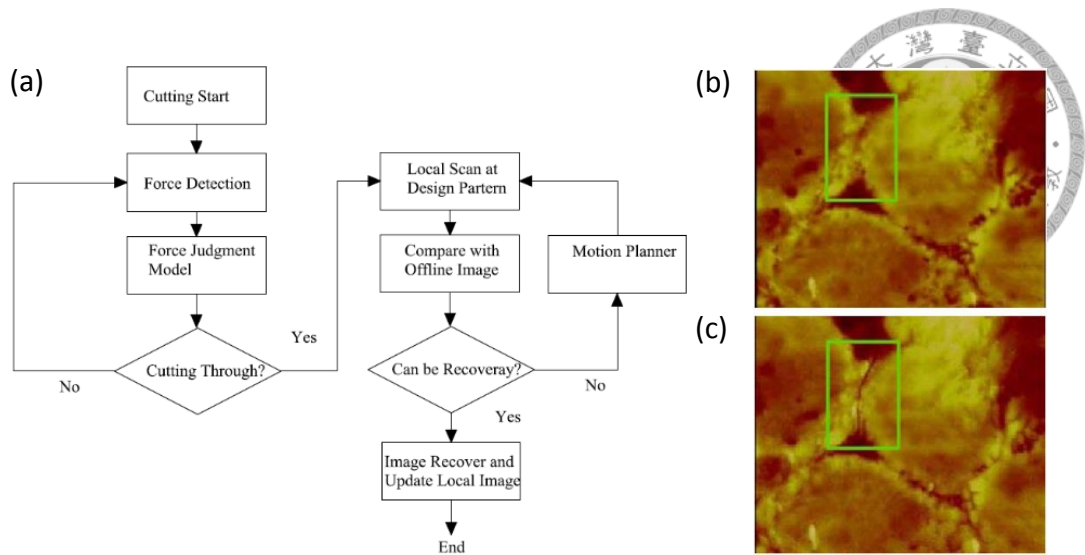


Fig. 1-12 (a) The strategy of local scan based online sensing for cell cutting (b) AFM image before cell cutting (c) AFM image after cell cutting

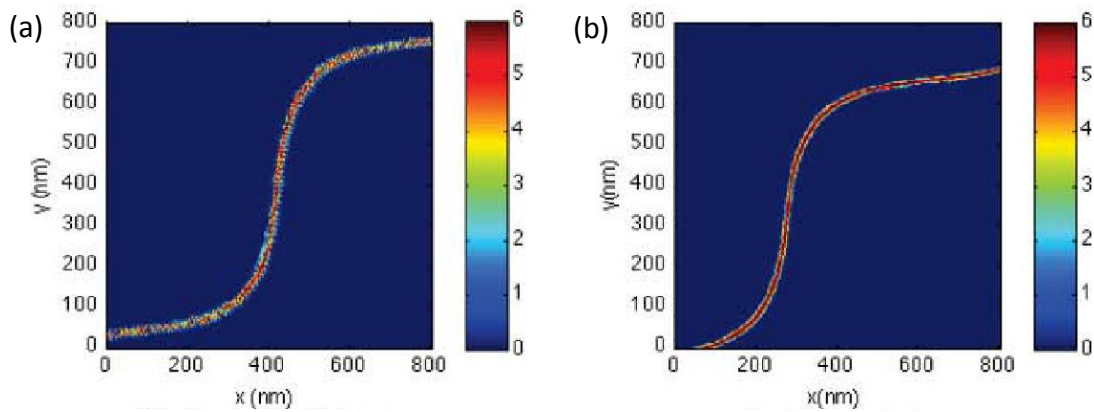


Fig. 1-13 (a) Local raster scan and (b) raster scan images of a sinusoidal test curve

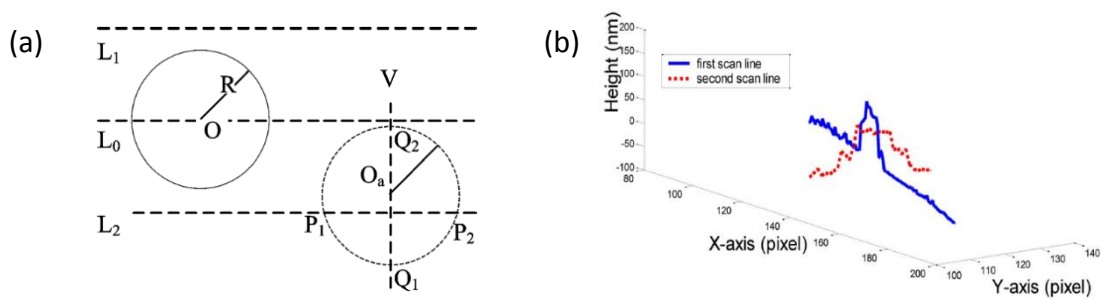


Fig. 1-14 (a) Local scan of nanoparticles (b) The local-scan-after-operation results of a nanoparticle

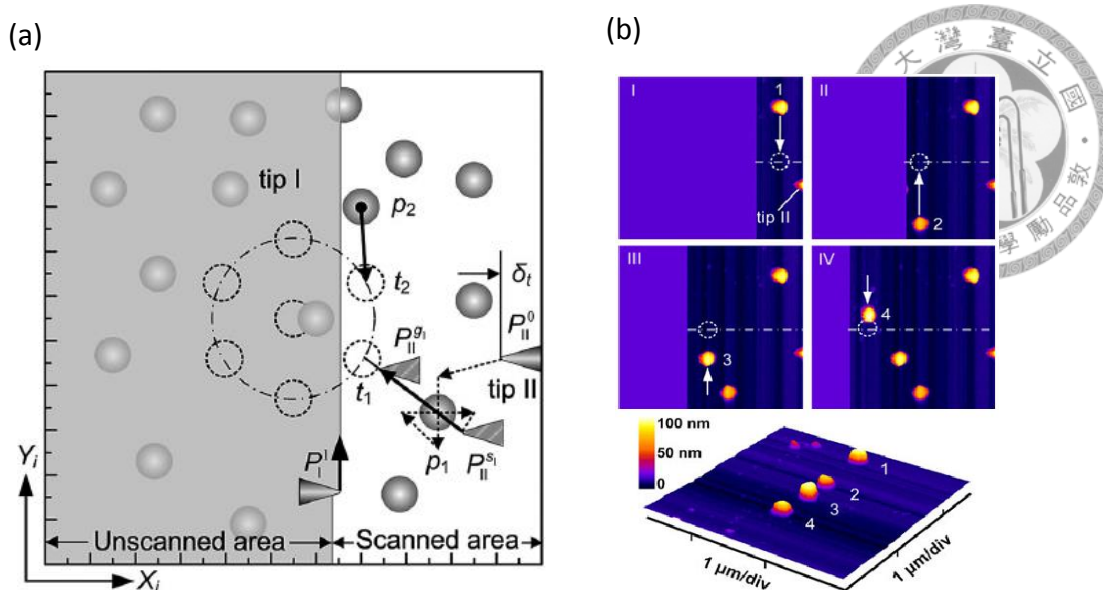



Fig. 1-15 (a) Parallel imaging/nanomanipulation scheme (b) Lateral push results with parallel manipulation

1.3 Contribution

Nowadays, AFM has been widely utilized in the precision biological measurement since it can scan the sample in native environment without damaging it. However, the main drawbacks of AFM measurement are small scan range and slow scan speed.

In this thesis, we develop an instrument that can scan a sample from large to small scales without trading off the precision. To achieve that, a homemade precision hybrid scanner including electromagnetic and piezoelectric scanners is designed. Electromagnetic scanners can provide large travelling-range and piezoelectric scanners with high-bandwidth feature. Besides, in order to increase the allowable scan rate in AFM, we apply a smooth Lissajous trajectory as the desired scan pattern. By exploiting



the well-known dynamics of the Lissajous trajectory, two advanced controllers, namely, neural network complementary sliding mode and adaptive complementary sliding mode controllers, are designed based on internal model principle to track the scan trajectory precisely at high scan speed, which are both theoretically proved and practically implemented. Compared with the most commonly used raster scan method, in which the scan trajectory is non-smooth, the Lissajous scan with the designed controllers allows a half-order increase in AFM scan speed under the same hardware conditions. Furthermore, in order to increase the scan rate of AFM, we design a new scan algorithm based on the characteristics of Lissajous trajectory to realize a new hierarchical local scan method by reducing the redundant scanning of uninterested area and considering the height variations of the scanned samples. This method can save the scan time, provide a high resolution image, and is applicable to scanning of biological cells of any shape in biological applications.

Despite the proposed AFM's scan method is realized in our home-made AFM system, it can be applied to many existing AFM systems without hardware modification as a matter of fact.

In a summary, the main contributions of this thesis are listed as follows:

1. By combining the piezoelectric scanner with an electromagnetic scanner, the




large scan range AFM with high precision can be realized.

2. By using the Lissajous scan trajectory based on the proposed controllers for AFM, a half-order scan speed improvement is achieved compared with the conventional raster scan based on PI controller.
3. A new hierarchical local scan methodology with the aid of Lissajous trajectory is developed to shorten the overall scan time and enhanced the scan resolution for samples of any shape.
4. The proposed scan method for improvement of the AFM scan speed can be implemented in most existing AFM systems without much hardware modification.
5. We successfully perform the scan on human blood cells using the proposed Lissajous hierarchical local scan method with our self-designed AFM system. The imaging quality is satisfactory and the scanning results match the data listed in existing biological literature.

1.4 Thesis Organization

In this thesis, we focus on the development of a new AFM scan method and the design of the AFM system with corresponding controllers. This thesis is organized as



follows. Chapter 1 introduces the motivations for this research and surveys the state-of-the-art studies in AFM scan improvement. In Chapter 2, we initially review several fundamental theories of piezoelectric and electromagnetic actuators, the CD/DVD Pickup head, and scanning principles of AFM system. Chapter 3 describes the overall system configuration, including the AFM measuring system and scanning system, the laser interferometer sensing system and the hardware equipment. Besides, modeling and formulation of the scanner dynamics are derived for the purpose of controller design. Chapter 4 presents the Lissajous hierarchical Local scan trajectory method which is discussed in detail. Chapter 5 proposes the control strategy and two advanced controllers for the hybrid scanner to deal with the external disturbances, model uncertainties, and unknown nonlinear hysteresis behavior. In Chapter 6, extensive experimental results and AFM scanning applications are provided to verify the performance of the proposed scan method. Finally, the conclusions of this thesis are made in Chapter 7.

Chapter2

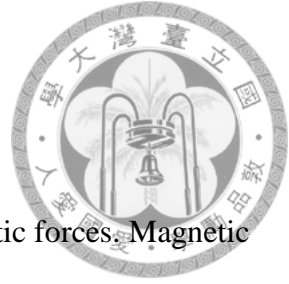
Preliminary



In this chapter, first we will briefly introduce the preliminary knowledge for the electromagnetic and piezoelectric actuators employed in our AFM scanning system. Then we will present the basic principle of CD/DVD pickup head which is used in our AFM measuring system. Next, we will provide the operation principle of the entire AFM system, and preliminary knowledge of the internal model principle (IMP) will also be given since the controllers of the AFM scanner are designed based on that.

2.1 Fundamentals of Electromagnetic Actuation

Since the scan range of traditional AFM can hardly exceed $100\mu\text{m}$, which limits the applications of the AFM. In this research, we combine an electromagnetic actuated scanner and a commercial piezoelectric scanner as a hybrid scanner to improve the AFM scan range, which is developed in our research group [23]. Hence, we will briefly investigate several properties of permanent magnets and the Lorentz force principle in the rest of this section.



2.1.1 Lorentz force principle

The Lorentz force equation is the basis for governing all magnetic forces. Magnetic fields are a description of the relativistic effects that occur among moving charges, which are a direct result of the Lorentz transformation of the Coulomb force.

The force dF on a current element $I \cdot dl$ immersed in a magnetic field B is given as:

$$dF = I \cdot dl \times B \quad (2.1)$$

Note that $I \cdot dl$ cannot exist by itself as it must be part of a complete loop or circuit. In such a loop, the total summed force is

$$F = \oint I \cdot dl \times B \quad (2.2)$$

As shown in Fig. 2-1, in order to simplify Eq. (2.2), a segment with length L of a long straight wire exposed to a uniform magnetic field B that is perpendicular to the wire, where the return path is outside the field, will be subject to the following relation,

$$F = IL \times B \quad (2.3)$$

where I is the current carried on the conduction wires, L is the length of the conduction wires through the magnetic field, and B is the external magnetic flux density. If there are N -turn wires through the magnetic field, then

$$F = NIL \times B$$



It is important to note that the force on the conductor is given only by Eq. (2.4) if the field due to the current I can be neglected.

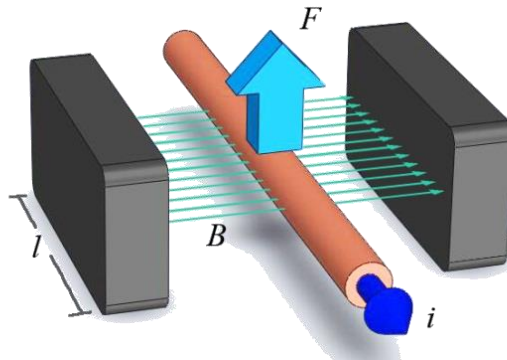


Fig. 2-1 Lorentz force principle

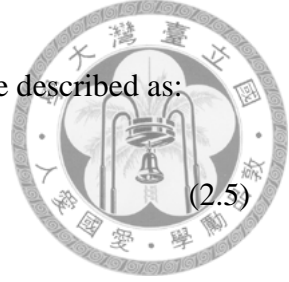
The electromagnetic actuators designed based on Lorentz force principle are often applied when high bandwidth dynamics are to be achieved. Examples are voice coil actuators, loudspeakers, synchronous brushless DC motors, and so on.

2.1.2 Properties of permanent magnet

Since electromagnetic actuators are utilized in the research work, it is crucial to understand the magnet characteristics. In this section, we will briefly review some basic properties of permanent magnets, and then present detailed specifications of the used magnets, such as maximum energy product, coercive force, temperature coefficient, etc.

According to Gauss law, the magnetic flux continuity law can be described as:

$$\nabla_{\mu_0} \vec{H} = -\nabla_{\mu_0} \vec{M} \quad (2.5)$$



When a magnetic field \vec{H} is applied to a ferromagnetic substance, the material will be magnetized with the internal flux density \vec{B} given by

$$\vec{M} = N\vec{m} \quad (2.6)$$

$$\vec{B} = \mu_0(\vec{H} + \vec{M}) \quad (2.7)$$

where \vec{M} is the induced magnetization density, defined as the magnetic dipole moment per unit volume, and N is the number of dipoles per unit volume. By (2.6) and (2.7), we can obtain the B - H curve by varying the field \vec{H} and measuring the flux density \vec{B} . Fig. 2-2 is a typical B - H curve of a ferromagnetic material, the curve OP is the initial magnetizing curve, and point P is the saturation point that means the material reaches its maximum magnetization. Once we vary \vec{H} from positive value to negative value and then back to the positive value again, the B - H curve forms a loop called hysteresis. The intersection of the loop and the \vec{B} axis is known as the remanence, residual magnetization, or residual flux density, denoted as \vec{B}_r , which is the magnetic flux density inside the magnet when the external field \vec{H} is reduced to zero. Moreover, \vec{H}_c is known as the coercivity or coercive force, which is the external field needed to completely demagnetize the substance.

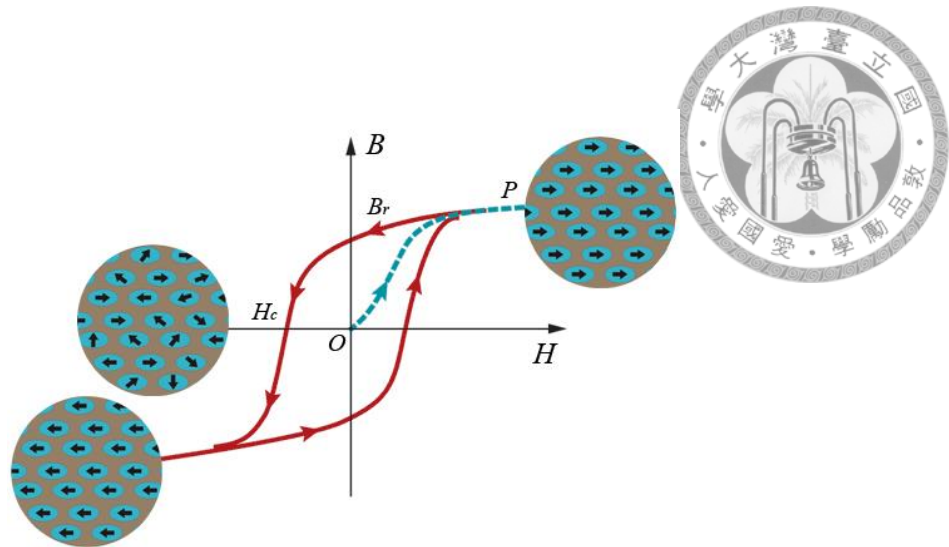


Fig. 2-2 B - H curve of a typical ferromagnetic material

By Eq. (2.5), when external \vec{H} is removed, the residual flux density inside the ferromagnetic material is

$$\vec{B}_r = \vec{M} \quad (2.8)$$

which indicates that the material has become a permanent magnets with residual flux density \vec{M} . Then, the magnetization of this permanent magnets can be expressed as:

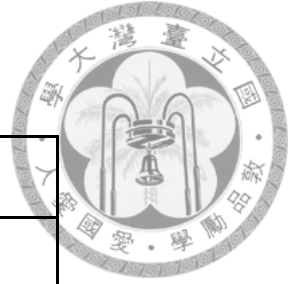
$$\vec{M} = \vec{B}_r \quad (2.9)$$

Therefore, the dipole moment resulting from the definition of magnetization is then given as:

$$\vec{m} = \vec{B}_r V \quad (2.10)$$

where V is the volume of this permanent magnets.

Table 2-1 Specifications of NdFeB



Specifications	NdFeB
Remanence (T)	1.29
Coercivity (kA/m)	990
Maximum energy product (kJ/m ³)	320
Density (g/cm ³)	7.49
Curie temperature (°C)	310
Resistivity (μΩm)	6

Rare-earth elements are the most popular materials used to produce the strong magnets. One of the strong magnets is Samarium Cobalt, which has high \overline{B}_r , high \overline{H}_c , relatively high maximum energy product (BH_{max}), and also higher cost than NdFeB. Commonly, its energy product ranges from 18 *MGOe* (Mega Gauss Oersteds) to about 32 *MGOe*. The most familiar one of the strong magnets is NdFeB or, for more accurately, sintered NdFeB magnet, whose property is similar to that of SmCo but which belongs to the most powerful class and is commercially available today. Its energy product ranges from 2.8 *MGOe* to about 48 *MGOe*. Therefore, NdFeB magnet is the most reliable choice to provide high magnetic force in our system. Table 2-1 indicates several characteristics of the NdFeB magnets.

2.2 Fundamentals of Piezoelectric Actuation



In AFM system, the piezoelectric actuation is the most popular actuation mechanism in the scanning system because of its fast dynamic response, high stiffness, and high positioning resolution. Hence, AFM can provide nano-resolution imaging performance of the sample topography. However, the hysteresis effect of the piezoelectric actuator is an inevitable behavior. In this section, we will investigate the piezoelectric effect and the hysteresis behavior.

2.2.1 Piezoelectric effect

The piezoelectric effect is that materials have the ability to generate electricity when subjected to mechanical stress, and it is first discovered by the brothers Pierre Curie and Jacques Curie in 1880 [24]. Conversely, the reverse piezoelectric effect is that materials deform slightly when an external electric field is applied as shown in Fig. 2-3. In 1922, Langevin proposed the first actuator based on the piezoelectric effect of crystal materials. However, because the piezoelectric effect exhibited by natural materials such as tourmaline, Rochelle salt and quartz are very rare, polycrystalline ferroelectric ceramic materials with the same properties have been developed such as barium titanate

and plumbum zirconate titanate (PZT), and the latter one is the most widely used materials for actuators today.

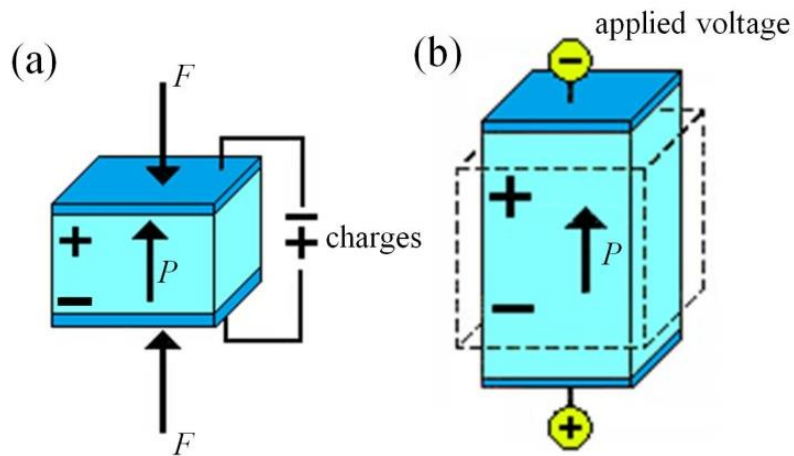
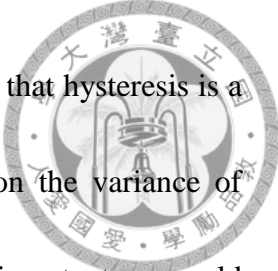


Fig. 2-3 (a) Piezoelectric effect (b) Reverse piezoelectric effect

According to the applied voltage, piezoelectric actuators can provide continuous expansion and retraction motions with high resolution, high stiffness, wide dynamic response range and no backlash. However, there are some disadvantages of piezoelectric actuators such as the small traveling range and nonlinear hysteresis effect which are described in the following section.

2.2.2 Hysteresis phenomenon

Hysteresis is the dependence of the system not only on its current input but also on its past input history. A typical hysteresis loop and a physical explanation for it has been



described by Chen and Montgomery [25] in Fig. 2-4. They presented that hysteresis is a result of grain domain switching, which occurs gradually, based on the variance of applied electric field. Increasing applied voltage to the piezoelectric actuators would cause severe hysteresis effect and the nonlinearity between the applied voltage and the displacement could go up to 10-25 % under large-signal situations. This nonlinearity will result in distortion on obtained images in AFM application.

The hysteresis effect can be reduced by using charge amplifiers; however, the design of charge amplifiers is more difficult than that of voltage amplifiers and it could lead to drift and saturation problems. Another method to overcome the hysteresis effect is building up the hysteresis model, and then designing a suitable controller based on the model to compensate it. There are several approaches to model the hysteresis phenomenon, such as Bouc-Wen model [26], simplified Dahl model [27], backlash-like model [28], Preisach model [29] and Maxwell model [30]. Although these methods are able to provide predictions of the behavior of piezoelectric actuators, they are hard to be applied in practical system controller designs because of the complexity of their hysteresis models.

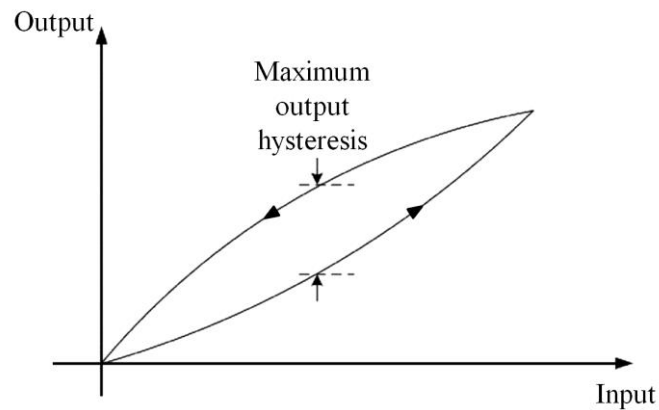


Fig. 2-4 Hysteresis loop

2.3 Basic Principles of CD/DVD Pickup Head

In order to reduce the complicated light path system and minimum the volume of the AFM measuring system, thus a commercial CD/DVD pickup head is used in this research.

In general, the optical pickup head can be divided into two parts: optical system and actuator. The optical system could be subdivided into laser diode, spectroscop, object lens, detection devices, diffraction gratings, and cylindrical lens further. The light emits from the laser diode and passes through the grating, then focuses on the CD/DVD-ROM and forms a spot. After reflecting from the record pothole on the CD/DVD-ROM, the spot will be transferred to the detection device through the optical system, and makes the



photosensitive current increase or decrease. The magnitude of this current is represented by 0 or 1 data.

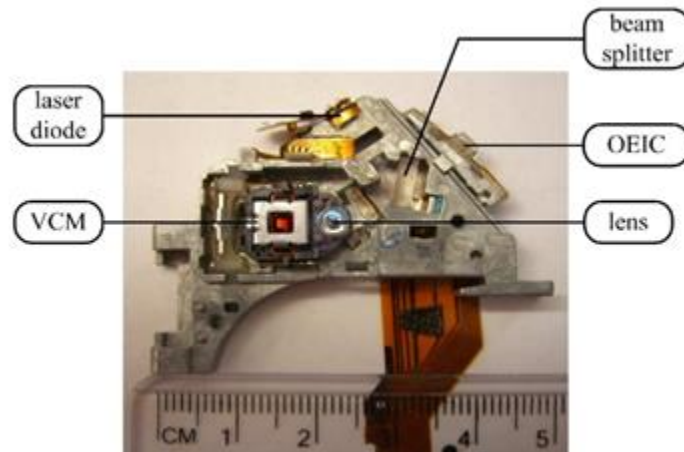


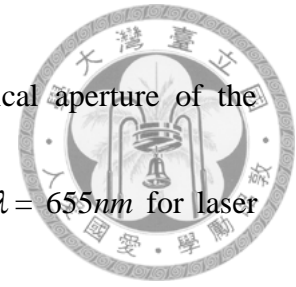
Fig. 2-5 Photograph of used CD/DVD pickup head and the total mass is 18g

The DVD system is chosen in this research rather than CD system because DVD system has better resolution and faster response. This DVD pickup head consists of four parts: laser diodes, lens set, opto-electric integrated circuit (OEIC), and focusing/tracking voice coil motors (VCMs). Fig. 2-5 illustrates the DVD pickup head used in our system (Model: TOP1100S, TopRay Technologies).

The full width at half maximum (FWHM) of focal spot can be derived from the following equation:

$$FWHM = 0.52 \frac{\lambda}{NA} \quad (2.11)$$

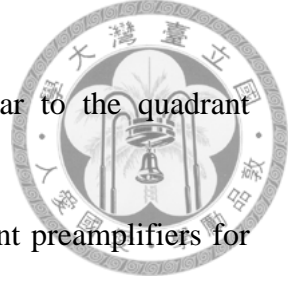
where λ is the wavelength of the laser and NA is the numerical aperture of the objective lens. Referring to the specification, the wavelength is $\lambda = 655nm$ for laser diodes on DVD pickup head and the numerical aperture is $NA = 0.6$ for objective lens.



Hence, the $FWHM$ $D = 568nm$ can be obtained. The width of the cantilever is several tens of micrometers, which is much greater than the $FWHM$. Therefore, the cantilever can block laser energy to prevent its leaking to the reflective sample that may cause sensing errors due to optical interference.

2.3.1 Sensing Methodology

Referring to Figs. 2-5 and 2-6, a laser beam emitted from a laser diode is first diffracted and collimated into three beams, and then focused onto an optical disk by an objective lens controlled by a VCM. After reflecting from the disc and passing through an astigmatic element, the beams will be directed back through the PUH and impinge onto the OEIC. The OEIC is composed of six split photosensors A-F (see Fig. 2-6), which have a current-to-voltage converter to transfer the tiny photocurrent into the voltage signal.



The center of OEIC is four quadrant photosensors (A-D), similar to the quadrant position-sensitive detectors used in traditional AFMs, and six current preamplifiers for the six photosensors. The data recorded on the disc, the focusing and tracking conditions from the summation signal, the focusing error (FE) signal and tracking error (TE) signal can be obtained from Eqs. (2.12)-(2.14) respectively as shown below.

The FE signal is used to measure the cantilever deflection in AFM applications.

$$Data = V_A + V_B + V_C + V_D \quad (2.12)$$

$$FE = (V_A + V_C) - (V_B + V_D) \quad (2.13)$$

$$TE = \text{phase difference between } (V_A + V_C) \text{ and } (V_B + V_D) \quad (2.14)$$

The relation between FE signal and the vertical distance of the disk is the so called S-curve as shown in Fig. 2-7 (d) [31]. When the laser beam is accurately focused on the disk surface, the laser spot on the four central quadrant photosensors (A-D) is circular (see Fig. 2-7 (b)) and is corresponding to the center of the S-curve. At the center of the S-curve, *i.e.* $FE = 0$, the sensitive linear range is about $8 \mu\text{m}$, which is enough for measuring the vertical deflection of the AFM cantilever. The resolution of the focusing



error signal depends on the quality of the output stage amplifier and noise from the environment.

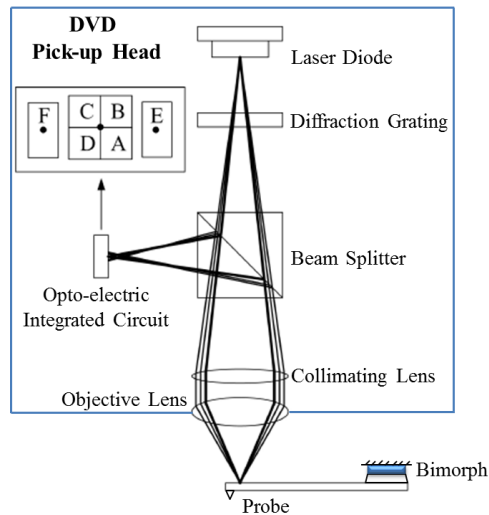


Fig. 2-6 Inside buildup and working principle of a typical CD/DVD pickup head

2.3.2 Focusing and Tracking Actuators

As for the focusing and tracking actuators, there are four suspending metal wires supporting the lens set as shown in Fig. 2-5. There are several benefits of this kind of guiding system: no friction, simple structure, and cost-effectiveness. The position of the lens set in horizontal (tracking) and vertical (focusing) directions can be finely adjusted using the VCM. The main disadvantages of this mechanism are the assemblage difficulty and the low stiffness that make the system easily affected by disturbance from the

environment.

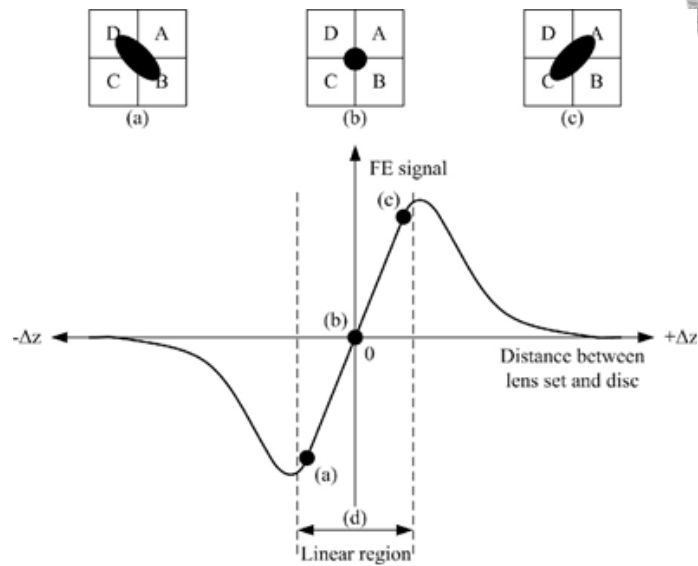


Fig. 2-7 (a) Off focus, $FES < 0$. (b) On focus, $FES = 0$. (c) Off focus, $FES > 0$. (d) Linear region of FES

2.4 Operation Principle of AFM System

Generally, there are two primary operation modes to be applied to measure the topography of sample in an AFM system: contact mode and tapping mode. Fig. 2-8 shows the schematic diagrams of both contact mode and tapping mode in an AFM system. In contact mode, the probe tip of the AFM will scrape across the sample surface along each scan line resulting in the deflection of the cantilever at its free end, which will be measured to reconstruct the topography of sample. The greater the cantilever is bent, the higher the force acts on the sample. However, a significantly deep valley or a significantly high hill on the sample surface cannot be sensed by the probe and brings



about the distortion on the obtained feature. Besides, some samples, like biological materials are often delicate and tenuously immobilized on a surface, and thus the vertical and shear forces exerted on the sample via the tip could damage the sample due to compressing or tearing from the surface in such contact mode.

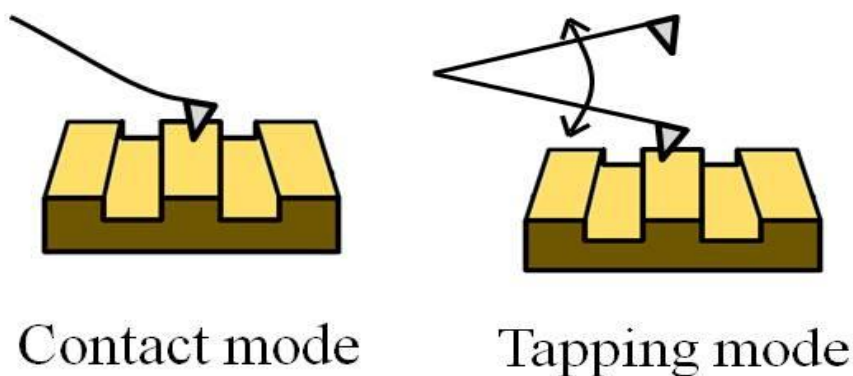


Fig. 2-8 The schematic diagram of contact mode and tapping mode

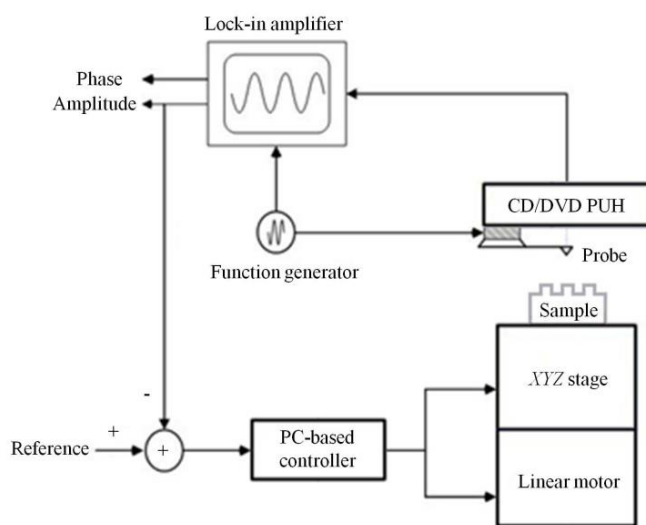



Fig. 2-9 The block diagram of a tapping mode AFM system

In tapping mode, the cantilever with the probe is oscillated vertically by a small piezoelectric material, called bimorph, at its resonant frequency; therefore, the probe tip



of the AFM system makes contact with the sample surface only in each cycle of oscillation. Fig. 2-9 shows the block diagram of a tapping mode AFM system. At the first, the probe and the sample are maintained at a constant distance, which is specified to be the amplitude of the probe's oscillation by a function generator. When the sample is moved by the *xyz* stage in scanning process, the probe offsets its height which is detected by the non-conventional CD/DVD pickup head sensor. The measured signal passing through a lock-in amplifier will be compared with the input signal from the function generator and then the difference is transmitted to a PC-based controller to keep the constant amplitude. The three dimensional voltage signals applied to control the *xyz* stage are collected to construct the topography of the corresponding sample.

Since the interaction force between probe tip and sample is about $10^{-10} \sim 10^{-12}$ N, the tapping mode AFM systems significantly reduce irreversible destructions on sample surfaces [30] and have been widely used for non-destructive measuring of soft or easily damaged materials such as polymers and biological samples [32]. The lateral forces are also significantly reduced compared with contact mode AFM systems, which minimizes positioning disturbance of the stage. Besides, the amplitude of the cantilever oscillation in tapping mode is typically several tens of nanometers, which ensures that the tip would not be stuck in a water layer resulting from surface tension force.

2.5 Internal Model Principle (IMP)

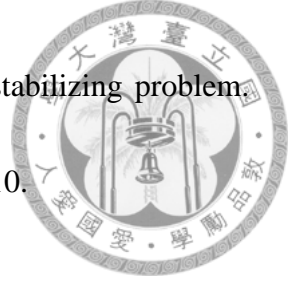


Generally, the control systems for reference tracking and disturbance rejection are two important control goals. In some scenarios, the reference or disturbances signals have known dynamics structure, and thus they can be considered as an external system. Then, the controller can track the reference or reject the disturbance by incorporating the model of the reference or disturbance signal within itself. This approach is known as internal model principle (IMP), and was first proposed by Francis and Wonham in 1976 [33].

The IMP states that if the reference $r(t)$ or the disturbance $d(t)$ has $\Psi(s)$ as the generating polynomial, then the controller $C(s)$ with the form:

$$C(s) = \frac{P(s)}{\Psi(s)L(s)} \quad (2.15)$$

It can ensure that to track the reference and to reject the effect of the disturbance can be achieved asymptotically. Here, $\Psi(s)$ is obtained from the dynamics of the reference or disturbance, and $P(s)$ and $L(s)$ need to be designed so that the closed-loop system is stable. From the viewpoint of linear time-invariant system, the IMP implies that the internal model is used to supply closed-loop transmission zeros which cancel the unstable poles of the reference or disturbance signals. Therefore, we can find that it



turns the tracking or disturbance rejection problem into a simple stabilizing problem.

The schematic diagram of the IMP based control is shown in Fig. 2-10.

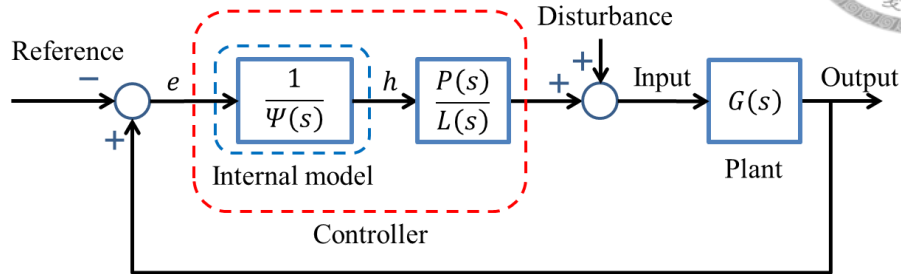


Fig. 2-10 The schematic diagram of internal model principle based control

However, the IMP is basically developed for LTI system with the concept of transfer function, which belongs to frequency-domain approaches and can hardly be applied to time-domain control scheme directly. In order to design the controller based on time-domain analysis or for nonlinear systems, we can consider the internal model from another viewpoint. Suppose the reference signal or disturbance satisfies some differential equation, *e.g.*,

$$\frac{d^n}{dt^n} r(t) + a_{n-1} \frac{d^{n-1}}{dt^{n-1}} r(t) + \dots + a_1 \frac{d}{dt} r(t) + a_0 r(t) = 0, \quad (2.16)$$

Then by taking Laplace transform, we obtain

$$[s^n + a_{n-1}s^{n-1} + \dots + a_1s + a_0]R(s) = f(0, s) \quad (2.17)$$

where $R(s)$ is the Laplace transform of the reference signal $r(t)$, $f(0, s)$ is a polynomial in s accounting for effects of the initial conditions, $r(0)$, $\dot{r}(0)$, $\ddot{r}(0)$, etc.

Let $\Psi(s)$ be the generating polynomial, then the internal model $G_I(s)$ can be

expressed as:

$$G_I(s) = \frac{1}{\Psi(s)} = \frac{1}{[s^n + a_{n-1}s^{n-1} + \dots + a_1s + a_0]} \quad (2.18)$$



Taking the internal model into Fig. 2-10, we can easily find the relationship between the tracking error e and the internal model state h in time-domain as:

$$e = h^{(n)} + a_{n-1}h^{(n-1)} + \dots + a_1\dot{h} + a_0h \quad (2.19)$$

Therefore, design of the controller in time-domain can proceed with this internal dynamics.

So far, there are many related researches in recent years, such as IMP-based sliding mode control [34], IMP-based state feedback control [35], IMP-based Kalman filter [36], etc. From Eq. (2.19), we can find that the reference tracking, or disturbance rejection now becomes a stabilizing problem since we just need to regulate the internal state to zero, and then the tracking error will be zero accordingly as well.

Chapter 3

System Design and Dynamics

Modeling



The overall AFM system based on tapping mode scheme is shown in Fig. 3-1. The design concept of the system is in accordance with the demand for fast and precision scanning of the sample's topography spread over a large range area. Generally speaking, both moving sample type and moving probe type AFMs have their own suitable applications and advantages. The comparison between these two types of AFM is arranged in Table 3-1. In order to obtain a good imaging quality of the sample and to simplify the optical complexity, we thus choose the moving sample type AFM in our system. The AFM system to be designed is mainly decomposed into two parts: the measuring system and the scanning system. The main function of the measuring system is detecting the tip-sample interaction from probe behavior (deflection, amplitude, phase, frequency, etc.). Additionally, we need a scanning system for the sake of understanding the whole sample topography. The entire AFM system will be described in the following sections.

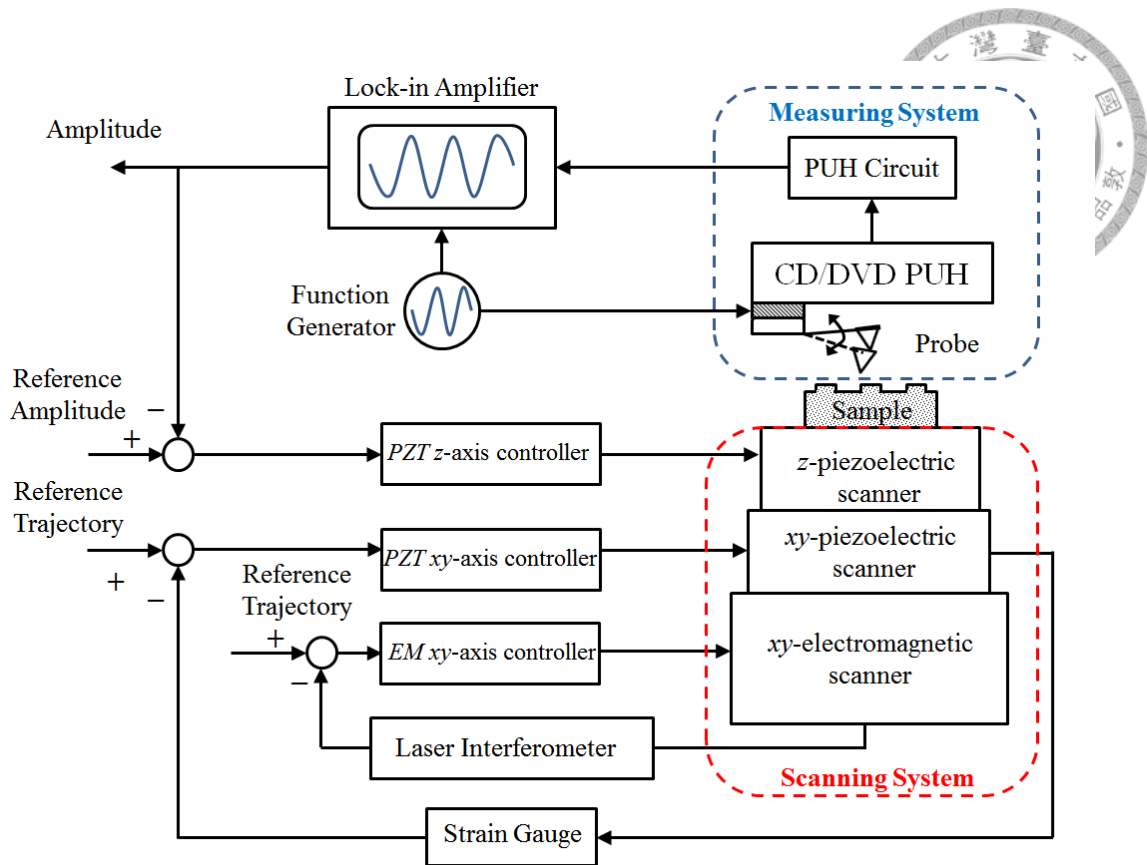


Fig. 3-1 The block diagram of our proposed AFM system

Table 3-1 Comparison between moving sample type and moving probe type

	Moving Sample Type	Moving Probe Type
Sample size	Small	Large
Scanning speed	Slow	Fast
Optical complexity	Simple	Complex
Image quality	Good	Normal

3.1 AFM Measuring System

For the scanning application, we need to excite the scanning probe at its first resonant frequency and detect the tip-sample interactions. Therefore, the AFM



measuring system must consist of two parts, which are probe oscillating system and probe dynamics detection.

3.1.1 Probe oscillating system

The probe used in an AFM consists of a cantilever and a tip, as depicted in Fig. 3-2. The choice of the probe in fact depends on the sample properties and the operation mode of AFM. Here, we will use function generator based on direct digital synthesized (DDS) technology to provide stable sinusoidal energy to a bimorph attached to probe, and thus providing stable scanning environments. When the energy enters the bimorph, the probe oscillates simultaneously. In practical implementation, the probe will be located on a magnetic circle mount, and the bimorph is attached to the mount, as shown in Fig. 3-3.

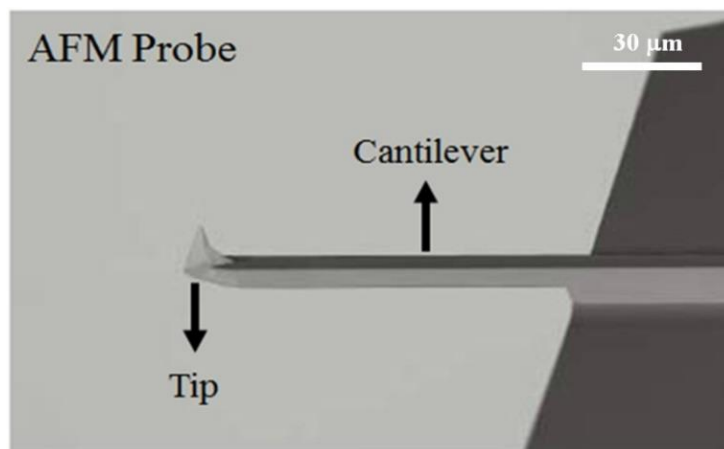


Fig. 3-2 Photograph of the AFM probe

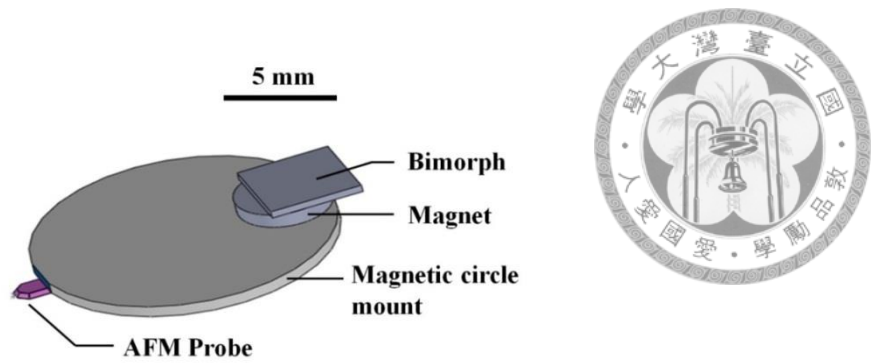


Fig. 3-3 The CAD figure of the probe oscillating system

Here, the probe we choose in this research is NanoWorld PointProbe Type-NCHR, which is designed for tapping mode AFM as shown in Fig. 3-4. The resonant frequency of the probe is about 250 kHz to 390 kHz. According to the manufacturing deviation, each probe has its own spectrum. The radius of curvature of this probe tip is less than 8 *nm* and the relevant specification of the probe is shown in Table 3-2.

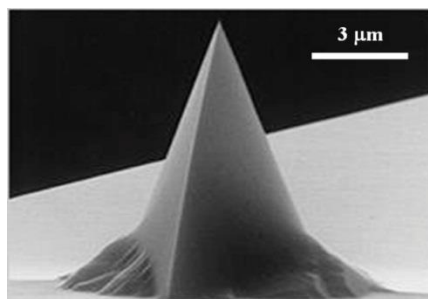


Fig. 3-4 The probe of NanoWorld PointProbe Type-NCHR

Table 3-2 Specification of the probe used in the research

Technical Data	Nominal Value	Specified Range
Thickness (μm)	4	3.0 - 5.0
Mean Width (μm)	30	22.5 - 37.5
Length (μm)	125	115 - 135
Force Constant (N/m)	42	10 - 130
Resonant Frequency (kHz)	330	204 - 497



3.1.2 Probe dynamics detection

The detailed structure of the AFM measuring system is shown in Fig. 3-5. In this system, we use the CD/DVD pickup head to measure the probe deflection for the compact system design. The CD/DVD pickup head is fixed on the frame and the probe beam is aligned by a precision tuning mechanism. The focusing error signal (FES) signal is the most important information for understanding the probe dynamics behavior. During the scanning process, since the bimorph is used a sinusoidal signal drive, thus the probe's cantilever beam will be excited in a sinusoidal motion, and thus the FES signal is also sinusoidal, which can be captured by the opto-electric integrated circuit (OEIC).

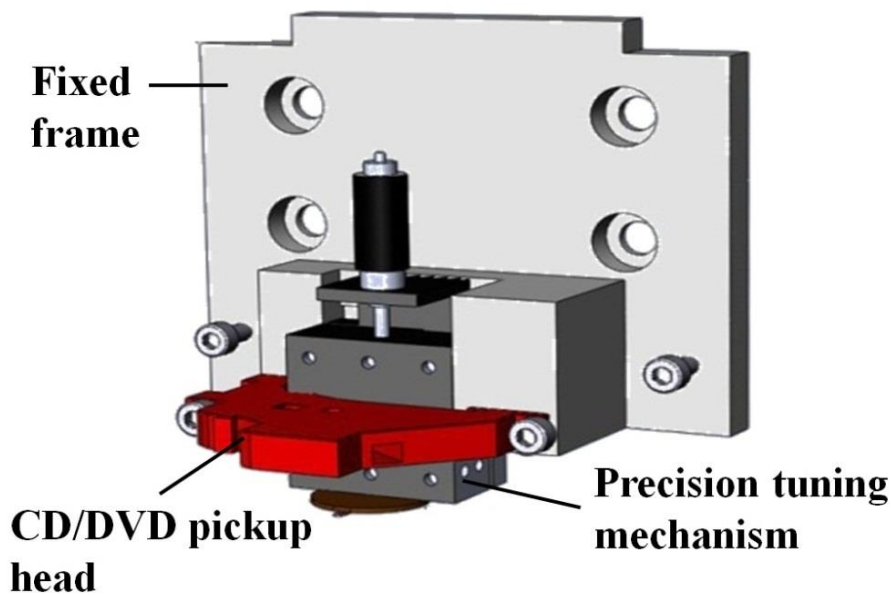


Fig. 3-5 The CAD figure of the mechanism of the AFM sensing system

3.2 AFM Scanning System



Generally, the AFM scanning system consists of two parts, which are the xy -scanner and the z -scanner. The xy -scanner moves the sample in xy -plane along the assigned scan trajectory, and the z -scanner is used to maintain the tip-sample interaction at the desired state. The detailed structure of our AFM scanning system is shown in Fig. 3-6. In order to achieve large scan range and high resolution imaging performance, the xy -scanner in our AFM system is a xy -hybrid scanner, including an xy -electromagnetic scanner and an xy -piezoelectric scanner. The xy -electromagnetic scanner is a homemade scanner with $2\text{ mm} \times 2\text{ mm}$ traveling range which has been developed in our research group [23]. It is composed of a monolithic xy parallel compliant mechanism, an eddy current damper, and four sets of electromagnetic actuator. To obtain the position information of the electromagnetic scanner, a 90° gold-coated mirror is mounted on the position base to reflect the laser beams emitted from the laser interferometer. On the other hand, the xy -piezoelectric scanner is a commercial scanner (Piezosystem jena PXY 38 SG), which has traveling range of $32\text{ }\mu\text{m}$ in x and y axes respectively with built-in strain gauge sensors. Fig. 3-7 shows the schematic diagram of the xy -piezoelectric scanner's operation principle, which utilizes the stacked piezoelectric



actuator with parallelogram flexure configuration composed of solid state hinge to provide parallel motion in xy -plane. The realistic photograph of the xy -piezoelectric scanner is shown in Fig. 3-8, and the relevant specification of this scanner is given in the Table 3-3.

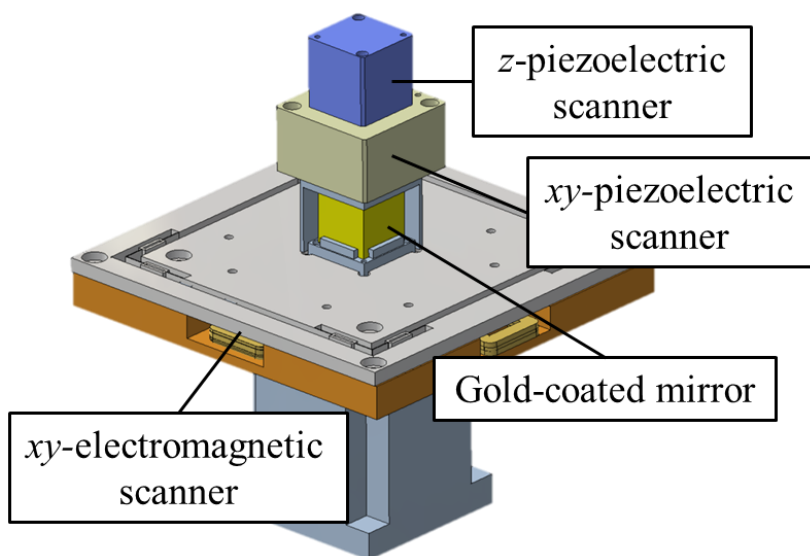


Fig. 3-6 The AFM scanning system

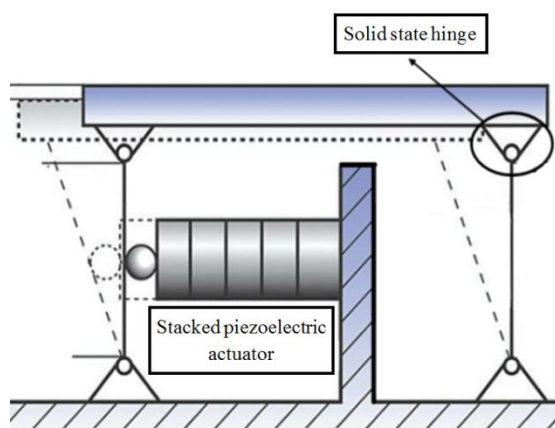


Fig. 3-7 The schematic diagram of the piezoelectric scanner's operation principle



Fig. 3-8 Realistic photograph of the piezoelectric *xy*-scanner

Table 3-3 Specifications of the piezoelectric *xy*-scanners

	PXY 38 SG
Motion ($\pm 10\%$)	32 μm
Capacitance per axis ($\pm 20\%$)	0.7 μF
Resonant frequency	0.73/1.09 kHz
Stiffness	2 N/ μm
Max. push force	59/53 N
Max. pull force	6/5 N
Dimensions	40mm \times 40mm \times 23mm

3.3 Dynamic Modeling and Formulation

In order to obtain good AFM imaging quality, design of advanced controller is necessary for improving the positioning precision of scanner. Before proceeding to the controller design, we need to understand the governing dynamics of the plant at first. In this section, we will derive the dynamic modeling of the *xy*-hybrid scanner according to



physical characteristics of mechanics and point the possible disturbance source during AFM scanning process. In this research, the controllers for the xy -hybrid scanner will be designed based on adaptive control and neural network, and thus we do not need to find parameter values of the plant model precisely. However, the system identification would also be addressed at the end of this section to confirm the preciseness of our dynamics modeling and formulation.

3.3.1 Modeling of Dual Lateral xy -Scanner

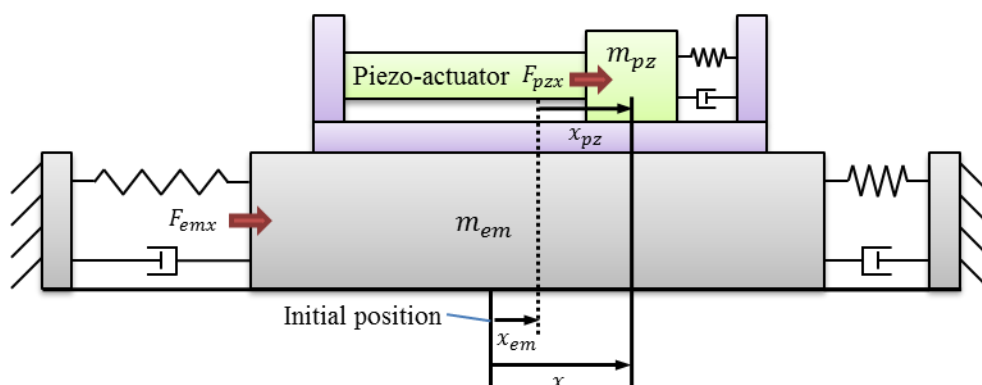


Fig. 3-9 The schematic diagram of xy -hybrid scanner in x -axis

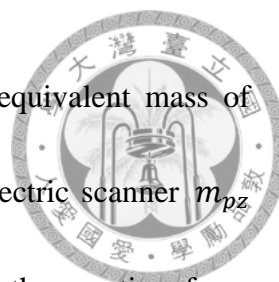
Fig. 3-9 shows the schematic diagram of xy -hybrid scanner in x -axis. In the dynamic analysis, since the xy -electromagnetic scanner is composed of the flexure parallel compliant mechanism with four sets of electromagnetic actuator, it can be reasonably modeled as a second order system [37]. On the other hand, the commercial xy -piezoelectric scanner consists of piezoelectric actuators with parallelogram flexure



configuration, as shown in Fig. 3-6, and it has been shown that a mass-spring-damper system is a reasonable model for the dynamics of piezoelectric scanner [38]. However, due to the piezoelectric actuation mechanism, the piezoelectric actuator will have hysteresis phenomenon and exhibits highly nonlinear dynamic motion. Therefore, taking the hysteresis effect into the dynamic model of piezoelectric scanner is very crucial for describing the positioning behavior correctly. Furthermore, because the piezoelectric scanner is stacked on the electromagnetic scanner, the piezoelectric scanner will impart reaction forces on the electromagnetic scanner. Hence, the motion behavior of xy -hybrid scanner in x -axis can be described by the following dynamic equations:

$$\begin{aligned}
 (m_{em} + m_{pz})\ddot{x}_{em} &= F_{emx} - k_{emx}x_{em} - b_{emx}\dot{x}_{em} + w_{pzx} \\
 m_{pz}\ddot{x}_{pz} &= F_{pzx} - r_{pzx}(x_{pz}, \dot{x}_{pz}) - k_{pzx}x_{pz} - b_{pzx}\dot{x}_{pz}
 \end{aligned}
 \tag{3.1}$$

where m_{em} and m_{pz} are the unknown equivalent masses of electromagnetic and piezoelectric scanner, respectively. The notations k_{emx} , k_{pzx} are the unknown equivalent spring coefficients, and b_{emx} , b_{pzx} are the unknown equivalent damping coefficients. F_{emx} and F_{pzx} represent the total applied forces generated by electromagnetic and piezoelectric actuators. w_{pzx} is the reaction force from piezoelectric actuator and r_{pzx} is the unknown nonlinear restoring force which results



in the hysteresis effect of the piezoelectric scanner. Because the equivalent mass of electromagnetic scanner m_{em} is much greater than that of piezoelectric scanner m_{pz} and the traveling range of piezoelectric scanner is very limited, the reaction force generated by piezoelectric actuator w_{pzx} can be assumed to be a small and bounded value compared to the forces generated by electromagnetic actuator F_{emx} in the first equation of Eq. (3.1). Hence, we can consider the reaction force w_{pzx} as part of disturbance in the dynamic model of electromagnetic scanner, and the modeling of the xy -hybrid scanner can thus be decomposed into two sub-systems.

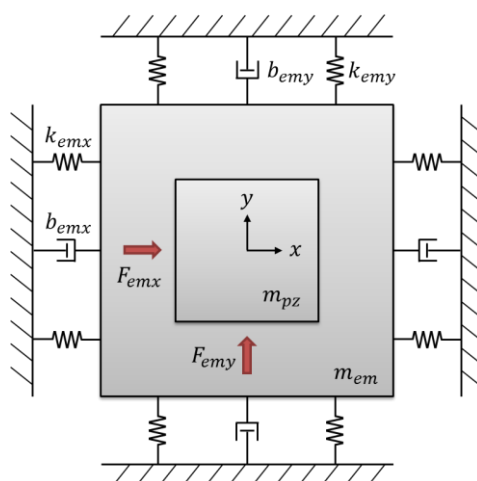
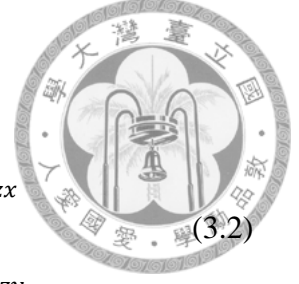


Fig. 3-10 The dynamic modeling of parallel structure

For the electromagnetic scanner, due to the parallel compliant flexure mechanism and eddy current damper, it can be modeled as a mass-spring-damper system as shown in Fig.3-10, the definition of x and y are the displacements along x - and y -axis, respectively. By Newton's Law, the system dynamics can be written in the following

form:

$$\begin{aligned} (m_{em} + m_{pz})\ddot{x}_{em} &= F_{emx} - k_{emx}x_{em} - b_{emx}\dot{x}_{em} + w_{pzx} \\ (m_{em} + m_{pz})\ddot{y}_{em} &= F_{emy} - k_{emy}y_{em} - b_{emy}\dot{y}_{em} + w_{pzy} \end{aligned} \quad (3.2)$$



According to the Lorentz force principle, the applied forces F_{emx} and F_{emy} are proportional to the input currents. Besides, taking the scanning disturbance into consideration, the dynamics of the electromagnetic scanner in Eq. (3.2) can be reformulated follows:

$$\begin{aligned} (m_{em} + m_{pz})\ddot{x}_{em} &= -k_{emx}x_{em} - b_{emx}\dot{x}_{em} + C_{emx}u_{emx} + w_{pzx} + d_{emx} \\ (m_{em} + m_{pz})\ddot{y}_{em} &= -k_{emy}y_{em} - b_{emy}\dot{y}_{em} + C_{emy}u_{emy} + w_{pzy} + d_{emy} \end{aligned} \quad (3.3)$$

where u_{emx} , u_{emy} are the input currents for the electromagnetic scanner, C_{emx} , C_{emy} are the force constants, and d_{emx} , d_{emy} represent the scanning disturbances.

To make the representation of the above dynamic equations more concise, we define the variable vector $X_{em} = [x_{em} \quad y_{em}]^T$ and rewrite the dynamical equations as a multi-input multi-output (MIMO) system:

$$\ddot{X}_{em} = K_{em}X_{em} + B_{em}\dot{X}_{em} + C_{em}U_{em} + D_{em} \quad (3.4)$$

The definition of the related parameters is shown in the following form:

$$K_{em} = \begin{bmatrix} \frac{-k_{emx}}{m_{em}+m_{pz}} & k_{emxy} \\ k_{emyx} & \frac{-k_{emy}}{m_{em}+m_{pz}} \end{bmatrix}, B_{em} = \begin{bmatrix} \frac{-b_{emx}}{m_e+m_p} & b_{emxy} \\ b_{emyx} & \frac{-b_{emy}}{m_{em}+m_{pz}} \end{bmatrix} \quad (3.5)$$

$$C_{em} = \begin{bmatrix} \frac{c_x}{m_{em}+m_{pz}} & 0 \\ 0 & \frac{c_y}{m_{em}+m_{pz}} \end{bmatrix}, U_{em} = \begin{bmatrix} u_{emx} \\ u_{emy} \end{bmatrix}, D_{em} = \begin{bmatrix} \frac{w_{pzx}+d_{emx}}{m_{em}+m_{pz}} \\ \frac{w_{pzy}+d_{emy}}{m_{em}+m_{pz}} \end{bmatrix}$$



Here, we introduce the off-diagonal terms in K_{em} and B_{em} to account for the coupling effect between x - and y -axis motions.

For the piezoelectric scanner, although the mass-spring-damper system is also a reasonable model to describe the dynamic behavior of it, an additional term that represents the hysteresis effect should be taken into account. The system dynamics can be written in the following form:

$$\begin{aligned} m_{pz}\ddot{x}_{pz} &= F_{pzx} - r_{pzx}(x_{pz}, \dot{x}_{pz}) - k_{pzx}x_{pz} - b_{pzx}\dot{x}_{pz} \\ m_{pz}\ddot{y}_{pz} &= F_{pzy} - r_{pzy}(y_{pz}, \dot{y}_{pz}) - k_{pzy}y_{pz} - b_{pzy}\dot{y}_{pz} \end{aligned} \quad (3.6)$$

where r_{pzx} , r_{pzy} represent the restoring forces which are both nonlinear functions, and F_{pzx} , F_{pzy} represent the applied forces which are proportional to the input voltage of the piezoelectric actuator. Often taking the external disturbances into consideration in the dynamic formulation of the piezoelectric scanner, then Eq. (3.6) can be rewritten in the following form:

$$\begin{aligned} m_{pz}\ddot{x}_{pz} &= C_{pzx}u_{pzx} - r_{pzx}(x_{pz}, \dot{x}_{pz}) - k_{pzx}x_{pz} - b_{pzx}\dot{x}_{pz} + d_{pzx} \\ m_{pz}\ddot{y}_{pz} &= C_{pzy}u_{pzy} - r_{pzy}(y_{pz}, \dot{y}_{pz}) - k_{pzy}y_{pz} - b_{pzy}\dot{y}_{pz} + d_{pzy} \end{aligned} \quad (3.7)$$

where C_{pzx} , C_{pzy} denote the piezoelectric force coefficient in x - and y -axis, respectively, and u_{pzx} , u_{pzy} are the input voltages for the piezoelectric actuators.



To simplify the representation of dynamic equation, we define the variable vector

$X_{pz} = [x_{pz} \quad y_{pz}]^T$ and rewrite Eq. (3.7) as a MIMO system:

$$\ddot{X}_{pz} = K_{pz}X_{pz} + B_{pz}\dot{X}_{pz} + C_{pz}U_{pz} - R_{pz} + D_{pz} \quad (3.8)$$

The definition of related parameters is shown in the following form:

$$\begin{aligned} K_{pz} &= \begin{bmatrix} \frac{-k_{pzx}}{m_{pz}} & k_{pzxy} \\ k_{pzyx} & \frac{-k_{pzy}}{m_{pz}} \end{bmatrix}, B_{pz} = \begin{bmatrix} \frac{-b_{pzx}}{m_{pz}} & b_{pzxy} \\ b_{pzyx} & \frac{-b_{pzy}}{m_{pz}} \end{bmatrix}, \\ C_{pz} &= \begin{bmatrix} \frac{c_{pzx}}{m_{pz}} & 0 \\ 0 & \frac{c_{pzy}}{m_{pz}} \end{bmatrix}, U_{pz} = \begin{bmatrix} u_{pzx} \\ u_{pzy} \end{bmatrix}, R_{pz} = \begin{bmatrix} \frac{r_{pzx}}{m_{pz}} \\ \frac{r_{pzy}}{m_{pz}} \end{bmatrix}, D_{pz} = \begin{bmatrix} \frac{d_{pzx}}{m_{pz}} \\ \frac{d_{pzy}}{m_{pz}} \end{bmatrix} \end{aligned} \quad (3.9)$$

Similarly, the off-diagonal terms of K_{pz} and B_{pz} represent the coupling effect between x - and y -axis motions.

3.3.2 AFM scanning disturbance

In tapping-mode AFM, the interaction forces are mainly contributed by Van der Waals force [39] and adhesion force by Derjarguin-Muller-Toporov (DMT) [40], which are consequently considered to be the major disturbance introduced to the stage while scanning (as shown in Fig. 3-11). Therefore, these forces will be analyzed in the following paragraph. In order to model the interaction force between the probe tip and the sample in the AFM system, the interactions between objects need to be studied. Assuming the potential is additive, the interaction energies between macroscopic bodies



can be obtained via integration. In the case of two interacting spheres with radius R_1 and R_2 at a distance D (as shown in Fig. 3-12), according to Derjarguin approximation [41], the force $F(D)$ between two spheres is given by

$$F(D) = \int_D^{\infty} 2\pi \frac{R_1 R_2}{R_1 + R_2} f(Z) dz = 2\pi \frac{R_1 R_2}{R_1 + R_2} W(D) \quad (3.10)$$

where $W(D)$ is the interaction potential energy between two flat surfaces. This formula holds whenever the interaction range and the separation D are much less than radii R_1 and R_2 .

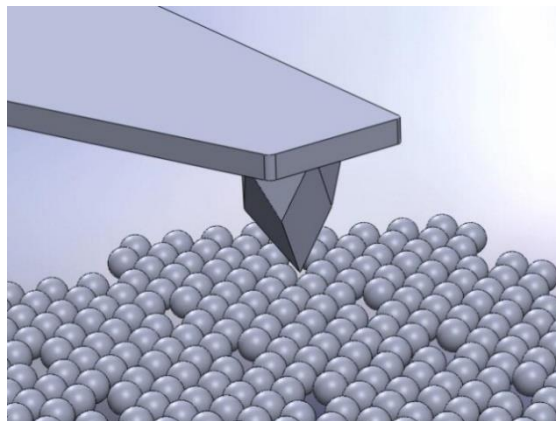


Fig. 3-11 The tip and sample interaction is considered as the disturbance to the stage

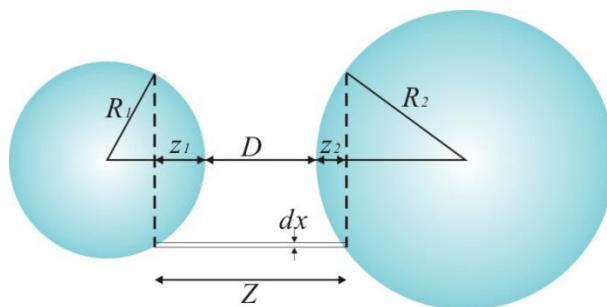
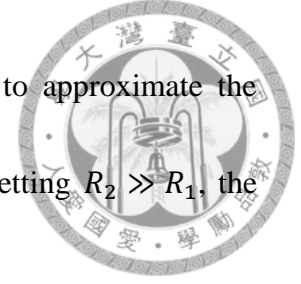


Fig. 3-12 Geometry employed in the Derjarguin approximation



Some previous researches have shown that it is reasonable to approximate the tip-sample geometry to sphere-flat in AFM application [42]. By setting $R_2 \gg R_1$, the force between a sphere and a flat surface can be obtained:

$$F(D) = 2\pi R_1 W(D) = -\frac{H}{6D^2} R_1 \quad (3.11)$$

where the Hamaker constant H , which includes all physical and chemical information shown as follows:

$$H = \pi^2 C \rho_1 \rho_2 \quad (3.12)$$

where C is the constant in the atom-atom pair potential, and ρ_1 and ρ_2 are the numbers of atoms per unit volume in two molecules, respectively. The Hamaker constant of condensed phases in vacuum is typically about $10^{-19} J$.

The interaction between tip and sample is determined by the attractive and repulsive surface potentials. The distance between tip and sample is $D = z_s + z$. The scalar z is the tip deflection and the scalar z_s is the distance between the undeflected cantilever and the sample. Van der Waals forces dominate the interaction in the attractive region ($D \geq a_0$). The tip-sample forces are calculated from Derjaguin–Muller–Toporov (DMT) model when D is in the repulsive region ($D \leq a_0$). The DMT model describes a situation where the energy dissipation due to tip-sample contact is negligible. To avoid an unphysical divergence, the parameter a_0 is introduced,

corresponding to the interatomic distance [41]. The tip sample forces are given by

$$F_{ts}(z) = \begin{cases} -HR/[6(z_s + z)^2] & D \geq a_0 \\ -HR/6a_0^2 + \frac{4}{3}E^*\sqrt{R}(a_0 - z_s - z)^{3/2} & D \leq a_0 \end{cases} \quad (3.13)$$

where R is the radius of the tip. The effective contact stiffness is calculated from $E^* = [\frac{1-\nu_t^2}{E_t} + \frac{1-\nu_s^2}{E_s}]^{-1}$, where E_t and E_s are the elastic moduli, and ν_t and ν_s are the Poisson ratios of the tip and the sample, respectively. It should be mentioned that the choice of bulk material parameters for the nano-scale simulations can only be a rough estimation. It has been shown that hardness of a material at nanometer scale is significantly different from its micro-hardness. Besides, the silicon tips are typically covered by a silicon oxide layer. Despite these, numerical simulations based on these bulk parameters provide useful predictions of the system dynamics. For very small oscillations around an equilibrium position z_0 , Eq. (3.13) can be linearized, leading to

$$k_{ts}^* = -\frac{\partial}{\partial z} F_{ts}(z)|_{z=z_0} = \begin{cases} -HR/[3(z_s + z_0)^3] & D \geq a_0 \\ 2E^*\sqrt{R}(a_0 - z_s - z)^{1/2} & D \leq a_0 \end{cases} \quad (3.14)$$

and the contact stiffness k_{ts}^* is normalized to the cantilever spring constant k by $\hat{k}_{ts} = k_{ts}^*/k$. After all these parameters are taken into account, the interaction force while scanning is calculated to be between $10^{-10} \sim 10^{-12}$ N, and is then considered as a scanning disturbance bounded by a constant.



3.3.3 System identification

In this research, the xy -hybrid scanner is controlled using adaptive control and neural network schemes, thus knowing the exact values of system parameters is not so necessary compared with some model-based control methods. However, in order to know the characteristics of the system and verify the correctness of the system dynamic modeling, we also identify the system and construct a mathematical model based on the measured input-output signals. Here, the system identification is performed for the xy -electromagnetic scanner and the xy -piezoelectric scanner separately.

For xy -electromagnetic scanner, since the first resonant frequency is small, we can obtain its mathematical model based on the subspace method by applying functions of system identification toolbox in MATLAB. With broadband knowledge of arbitrary number of white noise input and output data, five constant matrices A , B , C , D , and K of the state space representation in continuous time are estimated by command “n4sid”, as shown in the follows:

$$\begin{aligned} \dot{x}(t) &= Ax(t) + Bu(t) + Ke(t) \\ y(t) &= Cx(t) + Du(t) + e(t) \end{aligned} \tag{3.15}$$

The state space system representation can be transformed into continuous-time transfer function by using the command “ss2tf” in MATLAB.



By searching through the 1st-10th order models, the best model for xy -electromagnetic scanner in x -axis is computed to be a 2nd order one, and the continuous-time transfer function is given by:

$$G_{emx}(s) = \frac{-0.001402s + 2.468}{s^2 + 3.756s + 16553} \quad (3.16)$$

The Bode diagram of xy -electromagnetic scanner in x -axis is shown in Fig. 3-13. We can find that the first resonant frequency is about 129 rad/sec (20.53 Hz), and the bandwidth is about 131 rad/sec (20.85 Hz).

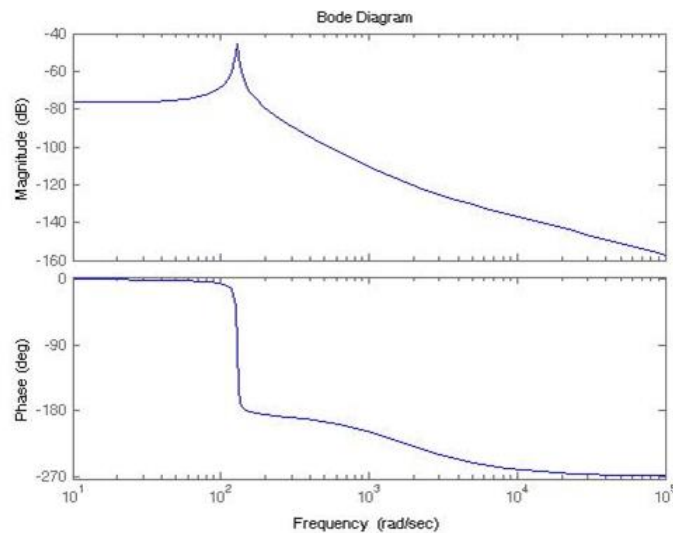


Fig. 3-13 The Bode diagram of xy -electromagnetic scanner in x -axis

Similarly, the best model for xy -electromagnetic scanner in y -axis is also computed to be a 2nd order model, and the continuous-time transfer function is given by:

$$G_{emy}(s) = \frac{-0.001475s + 2.603}{s^2 + 2.171s + 14319} \quad (3.17)$$

Fig. 3-14 shows the Bode diagram of xy -electromagnetic scanner in y -axis. The first



resonant frequency is about 120 rad/sec (19.10 Hz), and the bandwidth is about 122 rad/sec (19.42 Hz).

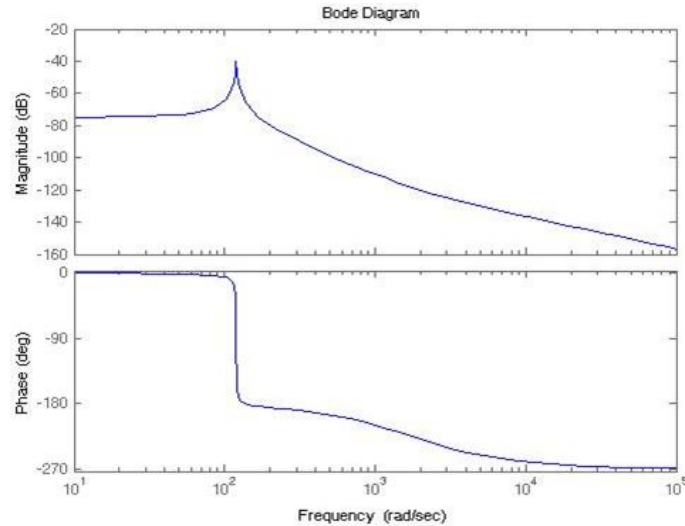
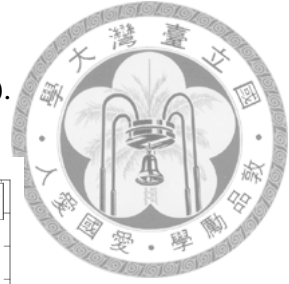


Fig. 3-14 The Bode diagram of *xy*-electromagnetic scanner in *y*-axis

For the *xy*-piezoelectric scanner, because the resonant frequency is high, it can hardly be identified with the previous method. We employ the MEMS Motion Analyzer (MMA) System supported by National Chip Implementation Center to implement system identification of the *xy*-piezoelectric scanner. The obtained frequency response of the *xy*-piezoelectric scanner in *x*-axis is shown in Fig. 3-15. By using the command “invfreqs” in MATLAB and choose 2nd order to calculate the matched model, the continuous-time transfer function is given by:

$$G_{pzx}(s) = \frac{4.058 \times 10^{-4}s + 11.436}{s^2 + 986.321s + 5.136 \times 10^7} \quad (3.18)$$

The resonant frequency appears at 7043 rad/sec (1121 Hz), the bandwidth is about 7326



rad/sec (1166 Hz), and the DC-gain is 2.26×10^{-7} m/V (-132.9 dB).

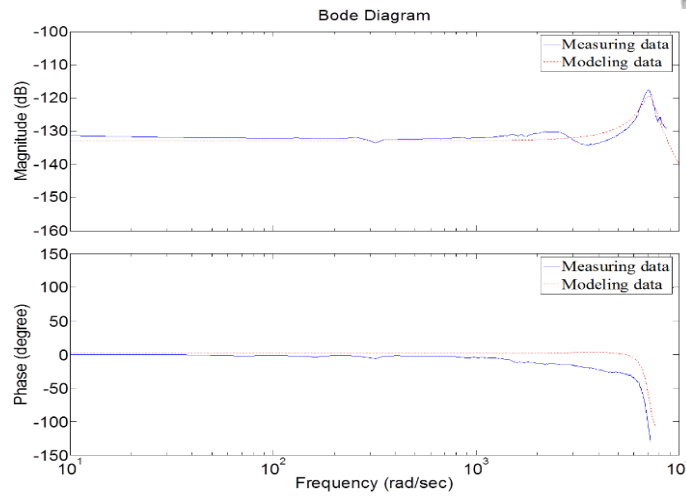


Fig. 3-15 The Bode diagram of xy -piezoelectric scanner in x -axis

Similarly, the obtained frequency response of the xy -piezoelectric scanner in y -axis is shown in Fig. 3-16, and is matched to a 2nd order continuous-time transfer function:

$$G_{pzy}(s) = \frac{4.497 \times 10^{-4}s + 13.214}{s^2 + 414.117s + 6.193 \times 10^7} \quad (3.19)$$

The resonant frequency appears at 7860 rad/sec (1251 Hz), the bandwidth is at 8049 rad/sec (1281 Hz), and the DC-gain is 2.14×10^{-7} m/V (-133.4 dB).

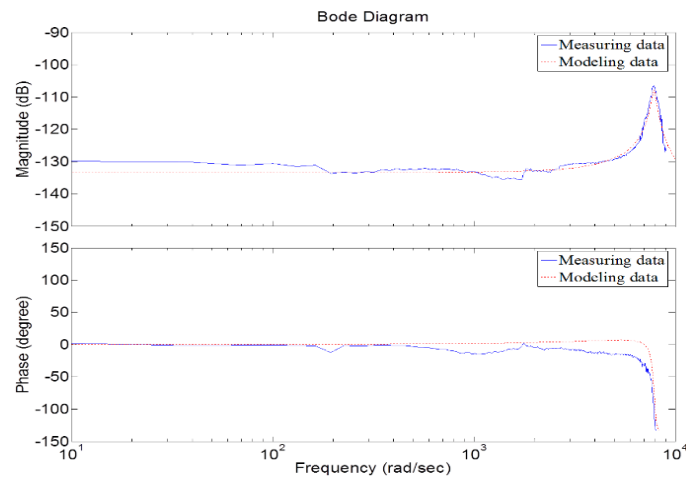


Fig. 3-16 The Bode diagram of xy -piezoelectric scanner in y -axis

3.4 Laser Interferometer Sensing System



Laser interferometer sensing system is an advanced tool which provides highly accurate measurement in the field of precise metrology. Laser beam has several advantages such as high intensity, high directionality, well spatial coherence, narrow bandwidth and monochromaticity [43]. Basically, the resolution of Laser interferometer sensing system is limited only by the sampling rate of electronics and noise level of the whole measuring-decoding system [44], [45]. Fig. 3-17 shows the overall system set-up including a 5517D laser head manufactured by Agilent Technologies emitting HeNe laser with wavelength of 633 nm. The diameter of the laser beam is 6 mm and the minimum output laser power is 180 μ W. The emitted laser beam will encounter a 10701A 50% beam splitter also made by Agilent technologies, in which laser beam is separated into two beams. The two spilt beams having equal-energy are directed into 10706B interferometer with turned configuration respectively. Moreover, we design the up-down structure of the beam path instead of left-right one, so that the beam path can be as short as possible in the limited space to reduce the effect resulting from the environment.

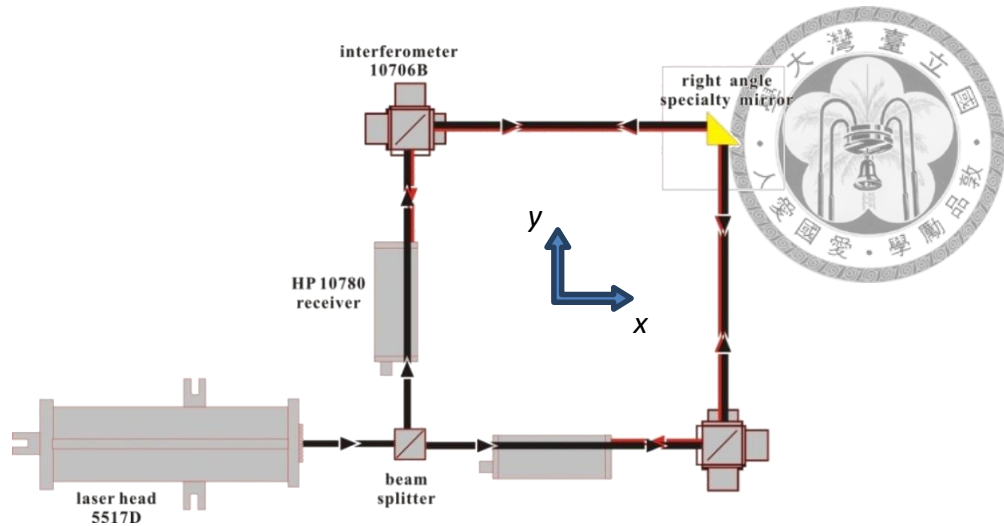


Fig. 3-17 The configuration of laser interferometer sensing system

In the 10706B interferometer, the incident laser beam is separated into a measurement beam and a reference beam. The measurement beam passes through the interferometer and then it is reflected by the plane mirror mounted on the xy -electromagnetic scanner to combine with the reference beam, which travels inside of the interferometer. A gold-coated right angle specialty mirror with ± 2 arcmins angle tolerance, as shown in the Fig. 3-6, is applied to ensure that the measured two axes are orthogonal in a traceable way. The protected gold allowing 96% average reflection is the most efficient reflective coating. Finally, both measurement and reference beams are received by the 10780C receiver of Agilent Technologies. Fig. 3-18 shows the beam path inside the 10706B interferometer, there are two laser beams with frequencies f_A and f_B entering the interferometer. These two laser signals with equal lengths and energies are received by the N1231B A/D card of Agilent Technologies, and then are compared with a



reference laser signal which is provided from the laser head to interpret the differential signal into displacement. According to designed interferometry beam path, the measured displacement is two times larger than the real one.

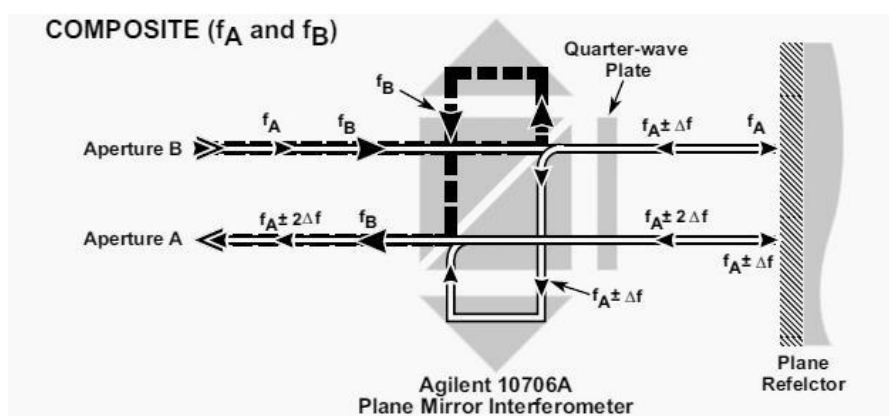


Fig. 3-18 The schematic diagram of beam path in 10706B interferometer

3.5 Hardware Equipment

The xPC Target developed by MathWorks Inc is a solution for testing real-time systems. Simulink® and Stateflow® models built on target computer can be executed for hardware-in-the-loop (HIL) simulation, rapid control prototyping, and real-time testing applications. By using target PC hardware, the xPC target can connect a real-time system to a non-real-time system which is usually under Windows operating system. Moreover, every hardware configuration needs to be constantly checked by real-time operating system for regular operation. With high sampling rate A/D, D/A cards and high speed

computing CPU, we can achieve 20 kHz real-time sampling rate at most without influential timing latency.



The xPC Target software provides users to generate an executable code from the model built in Matlab/Simulink and C/C++ command code in the host PC, for example, typical signal processing and arithmetic blocks as well as I/O blocks, and then the code is uploaded and executed in the target PC. The dual lateral xy -scanner and dual vertical z -scanner perform commands sent by National Instrument PCI 6733 16-bit D/A card. Through the sampling and decoding processes of two laser axis board N1231B made by Agilent technologies, we can obtain position data of xy -electromagnetic scanner per axis with 32-bit resolution. Besides, the position data of xy -piezoelectric scanner is acquired by strain gauge sensor, amplifier, and an A/D card Measurement Computing PCI-DAS 1602/16 with 16-bit resolution. Then, the digital data are processed in the target PC, computing the position errors and sending feedback to the xy -hybrid scanner by A/D card Measurement Computing PCI-DAS 1602/16. The diagram of system hardware structure is shown in Fig. 3-19.

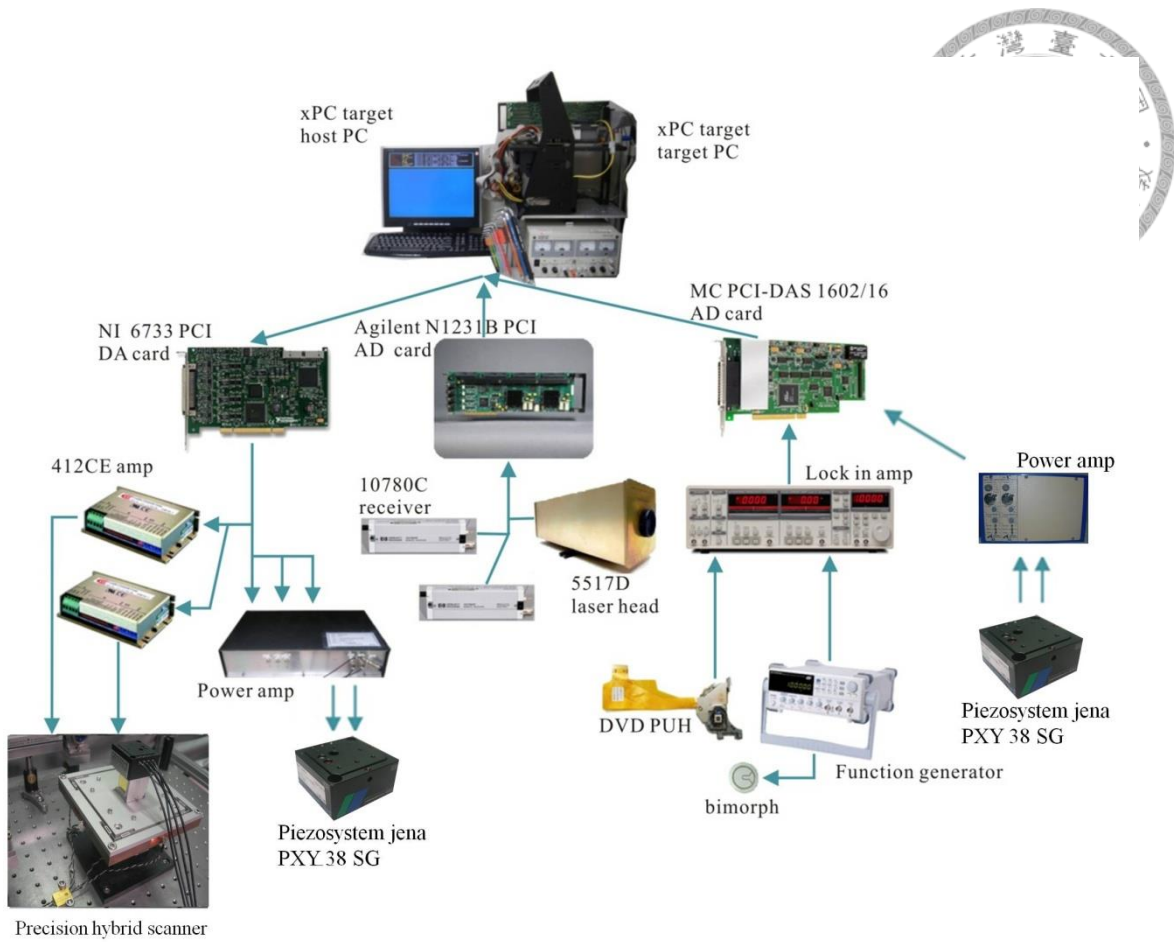


Fig. 3-19 The diagram of system hardware structure

Chapter 4



Lissajous Hierarchical Local Scan

In the AFM scanning process, the sample is measured by moving the sample or scan probe in xy -plane along a given scan trajectory. Conventional AFM scan trajectory uses a raster pattern throughout a rectangular scan region, and then collect measured data along a standard grid to build the image of the sample topography with pixel-by-pixel method. However, due to the dynamics characteristic of the raster scan trajectory, it will induce the mechanical vibration of the scanner, and therefore the scan speed is restricted. In order to improve the scan speed of the scanner, we replace the raster scan trajectory by a smooth Lissajous scan trajectory in this research. In addition, since the scan region mostly contain some uninterested areas, which lead to redundant scan time. For the purpose of reducing the scan time and reaching the desired scan resolution of interested sample, we propose a new hierarchical local scan based on Lissajous scan trajectory. By using Lissajous scan points in previous layer to decide Lissajous scan area in next layer, which can effectively reduce the scan area and improve the scan resolution with this type of hierarchical scan. In this chapter, we first discuss both raster and Lissajous scan trajectories, and then formulate the Lissajous

trajectory from the fundamental principle which simultaneously describes how Lissajous points are mapped to raster points. Finally, the proposed new Lissajous hierarchical local scan method will be introduced.



4.1 Scan trajectory Analysis

Generally speaking, raster scan trajectory has been the standard trajectory used in AFM system. During the AFM scanning process, the lateral scanner has to track a triangle waveform in one axis, and a staircase waveform in another axis. By combining both, we can produce a raster scan trajectory. Although this kind of scanning method can provide acceptable solutions during slow scan speed, it cannot give a good performance in faster scan process due to using the non-smooth scan trajectory. For an acceptable scanning quality, the frequency of the raster scan is typically limited to about 1% of the first resonance frequency of the scanner. It is a main constraint to the scanning speed of AFM system. As a result, a smooth Lissajous scan trajectory has been applied to AFM scanning [18], [46], and it has been shown that such scan trajectory can effectively reduce the vibration phenomenon of the lateral scanner during scanning process. The detailed analysis of raster and Lissajous scan trajectory are introduced in the following sections.



4. 1. 1 Conventional raster scan trajectory

The raster scan trajectory can be generated by tracking a triangular waveform in the x -axis and staircase waveform in the y -axis respectively, and the waveform signals are described as follows:

$$\begin{aligned} x_{raster}(t) &= \frac{4A_r}{T_r} \left(t - \frac{T_r}{2} \left[\frac{2t}{T_r} + \frac{1}{2} \right] \right) (-1)^{\left[\frac{2t}{T_r} + \frac{1}{2} \right]} \\ y_{raster}(t) &= P_r \left[\frac{2t}{T_r} + \frac{1}{2} \right] \end{aligned} \quad (4.1)$$

where A_r is the amplitude of triangular signal, T_r is the period of signals, P_r is the scan pitch, the symbol $[n]$ represents the floor function of n , and t is a time constant.

The signal waveforms in x - and y -axes and the raster scan trajectory are shown in Fig.

4-1.

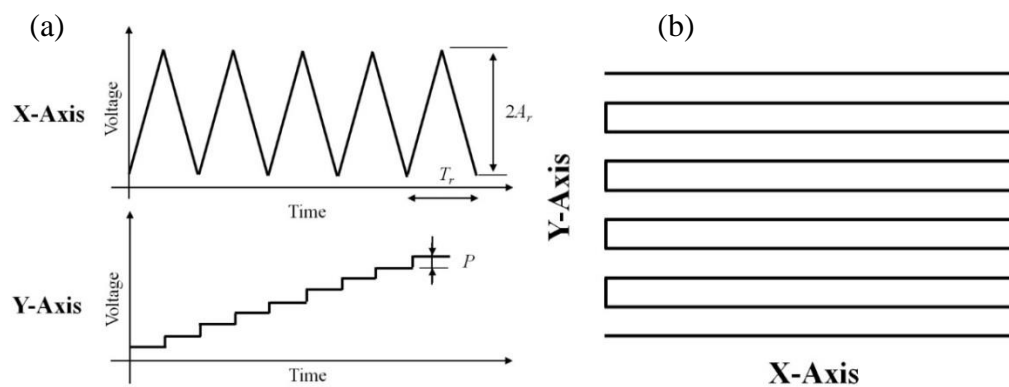


Fig. 4-1 The diagram of raster scan trajectory (a) the signal waveforms of x and y axes (b) the raster scan trajectory by combining both signals.

In general, a high speed raster scan has to use a high frequency triangular waveform for the scanner. It is well known that a triangular waveform can be



approximated with additive synthesis by adding all odd harmonics of the fundamental mode, and thus the triangular waveform can be described by an infinite Fourier series as shown below:

$$x_{raster}(t) = \frac{8A_r}{\pi^2} \sum_{k=0}^{\infty} (-1)^k \frac{\sin(2\pi f_r(2k+1)t)}{(2k+1)^2} \quad (4.2)$$

where f_r is the scan frequency equals to $1/T_r$. The frequency spectrum of a triangular waveform with $A = 1$ and $f = 220$ Hz is shown in Fig. 4-2. We can find that the triangular waveform contains all odd harmonic signals of its fundamental frequency, and the amplitudes of these harmonic signals attenuate as $1/(2k+1)^2$, where $2k+1$ is the harmonic number. Therefore, when a fast triangular waveform is applied to the scanner, it will inevitably excite the mechanical resonance of the scanner. Such result will vibrate the scanner and cause a distorted triangular trajectory in scanner, and indirectly affect the scanning performance.

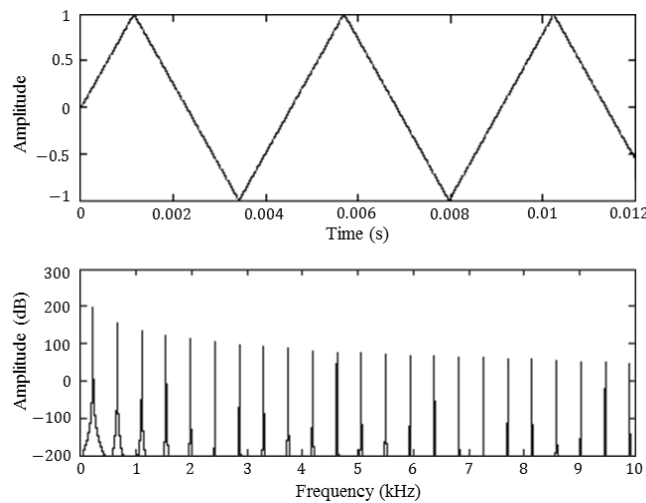


Fig. 4-2 The frequency spectrum of a triangular waveform with $A = 1$, $f = 220$ Hz



4. 1. 2 Smooth Lissajous scan trajectory

Unlike the aforementioned non-smooth raster scan trajectory, in this section, we will describe a smooth Lissajous scan trajectory used to increase the scan speed of the lateral scanner. The Lissajous scan trajectory can be constructed by tracking the following signals in the x and y axes:

$$\begin{aligned}x_{Lissajous}(t) &= \frac{A_x}{2} \cos(2\pi f_x t) \\y_{Lissajous}(t) &= \frac{A_y}{2} \cos(2\pi f_y t)\end{aligned}\tag{4.3}$$

where f_x , f_y are the frequencies of the cosine signals and A_x , A_y are the amplitudes of the cosine signals.

A major advantage here compared with the raster scan trajectory is that the Lissajous scan trajectory is a smooth one by using the two cosine waveforms for x - and y -axis scans. Fig. 4-3 shows the frequency spectrum of a cosine waveform with $A = 1$ and $f = 220$ Hz. We can find that the cosine waveform contains single frequency signal, whose frequency can in fact be set closer to the scanner's first resonance frequency. Because their smooth scan trajectory contains no other high frequency signal, it will not excite the resonant mode to induce the vibration phenomenon of the scanner. In addition, another axis motion of raster scan trajectory is a staircase waveform, which is also a non-smooth trajectory for the scanner. Therefore, by using signals of two



smooth cosine waveforms to replace the non-smooth triangular and staircase waveforms, the result will effectively improve the tracking performance of the lateral scanner conceivably.

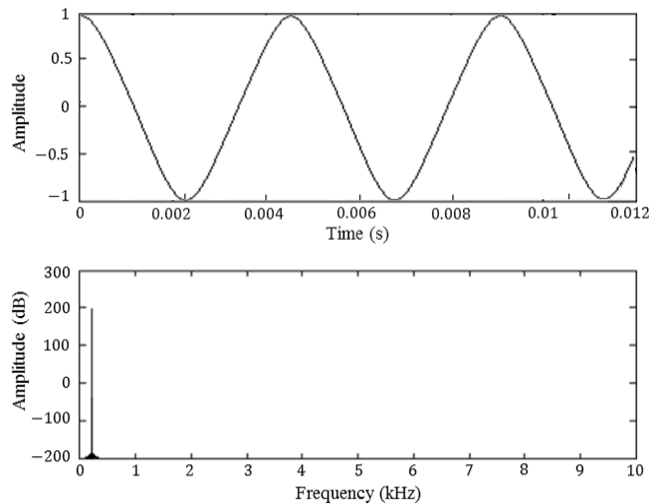


Fig. 4-3 The frequency spectrum of a cosine waveform with $A = 1$, $f = 220$ Hz

4.2 Lissajous Scan Trajectory Formulation

In this section, we will focus on the Lissajous scan trajectory from two parts: The Lissajous scan trajectory principle is described at first, and then how to mapping Lissajous points to raster points are discussed.

4.2.1 Trajectory fundamental principle

The Lissajous scan trajectory for scanning application must calculate the half-period scanning time and maximum scanning pitch. In the following, we will focus



on these two aspects to perform the detailed discussion.

Half-period scan time

In Eq. (4.3), the frequency difference between f_x and f_y will determine the period of scan time and the form of the Lissajous scan trajectory. Generally, we can describe the relationship between f_x and f_y by a constant n and a fundamental frequency f as follows:

$$\begin{aligned} f_x &= 2nf \\ f_y &= (2n - 1)f \end{aligned} \quad (4.4)$$

Since the reciprocal of the fundamental frequency is the fundamental period T , we can find the fundamental period T by Eq. (4.4) as [47]:

$$T = \frac{1}{f_x - f_y} = \frac{1}{f} \quad (4.5)$$

Next, we will investigate the relation between the period and the form of the Lissajous trajectory. For better grasp of the idea, we start with a simple example as shown in Fig. 4-4, where we use the $n = 12$ such that the frequencies $f_x = 24$ Hz, $f_y = 23$ Hz, and assign the amplitudes A_x, A_y as 1, and the resulting Lissajous scan trajectory is shown to be confined in a square region. By Eq. (4.5), the fundamental period of the Lissajous scan trajectory in this example can be calculated, which is equal to 1 second.

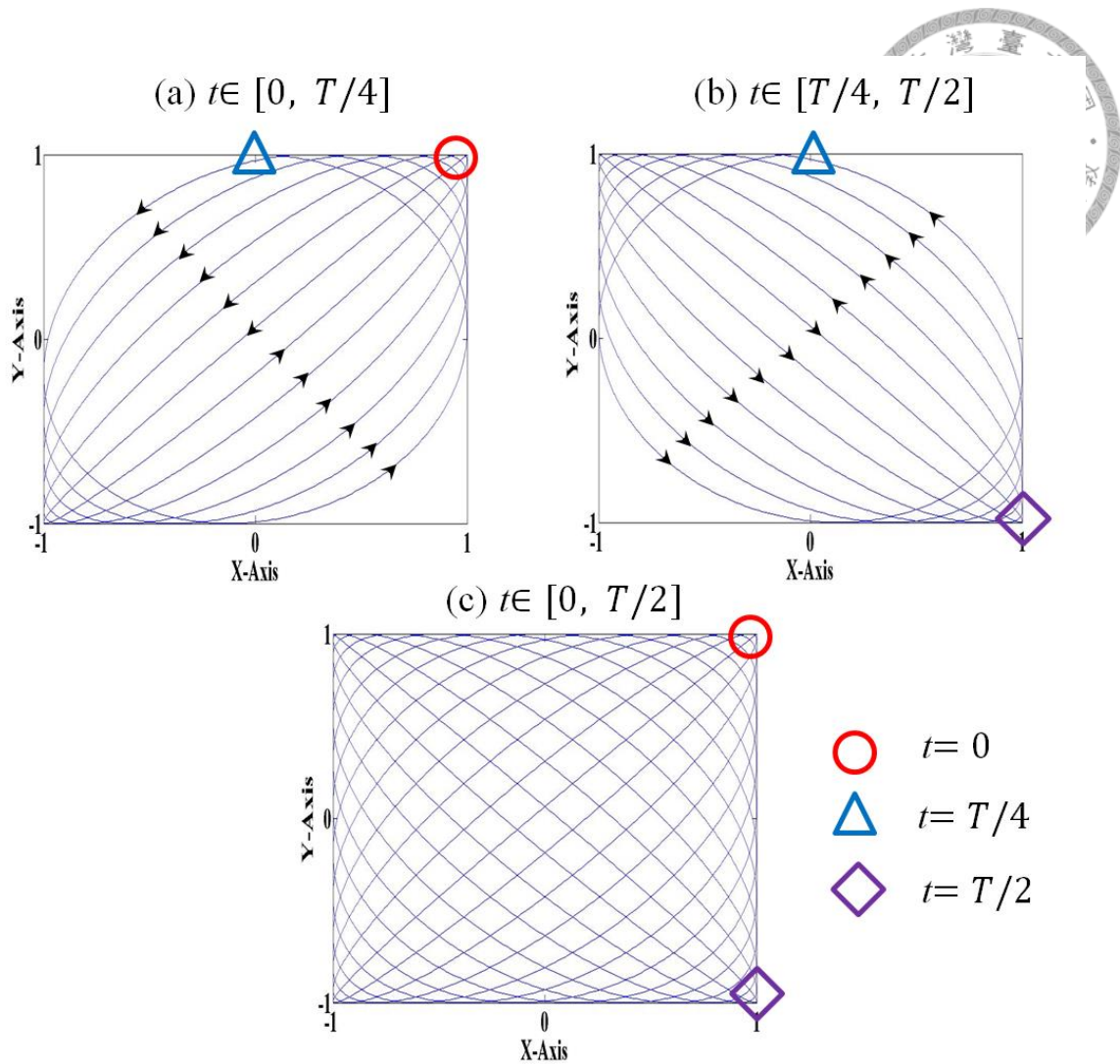


Fig. 4-4 Schematic of the Lissajous-scan trajectory with $n = 12$, and A_x, A_y are 1, (a) The first quartered period. (b) The second quartered period. (c) A square formed scan trajectory can be fully generated by a half-period Lissajous scan trajectory.

Fig. 4-4 (a)-(b) shows the change of the Lissajous scan trajectory. During the first quarter period ($0 \leq t \leq T/4$), the trajectory scans counter clockwise from an almost-diagonal line to multiple ellipse-like curves, as shown in Fig. 4-4 (a). Under the second quarter period ($T/4 \leq t \leq T/2$), the trajectory is back to a different diagonal and then traverse counter-clockwise to multiple ellipse-like curves similar to previous fashion, as shown in Fig. 4-4 (b). Besides, during the third and fourth quarter periods, it



will perform a reverse trajectory of that in the 2nd quarter period and then that in the 1st quarter period. Now, if we overlap the trajectory of the first quarter period and that second quarter period as shown in Fig. 4-4 (c), then we obtain a complete Lissajous scan trajectory which is formed over a square region using a half-period scan time ($0 \leq t \leq T/2$). Thus, in the sequel we will apply only half-period Lissajous trajectory for the square Lissajous scan result in our AFM system.

Maximum scan pitch

Since the Lissajous trajectory is composed of two cosine waveforms, its scan pitches is not uniform. In general, the sampling time is usually designed shorter than the time interval associated with the scan pitch, so that we can determine the appropriate image resolution in x and y axes by calculating the maximum scan pitch of the scan trajectory. To calculate the maximum scan pitch, we first obtain the time interval of scan pitch δ , defined as follows [46]:

$$\delta = \frac{1}{2} \left(\frac{1}{f_y} - \frac{1}{f_x} \right) = \frac{1}{4n(2n-1)f} \quad (4.6)$$

For easy understanding, we use an example of Lissajous trajectory with $n = 2$. From Eq. (4.4), we can get that $f_x = 4 \text{ Hz}$ and $f_y = 3 \text{ Hz}$, and then construct the scan trajectory on xy -plane as shown in Fig. 4-5. In the figure, red circle is the starting point, and purple rhombus is the ending point, and all black triangles are pitch points of



Lissajous trajectory. The time interval of scan pitch is defined as the time elapse for traversing from an arbitrary pitch point to its next pitch point along the trajectory.

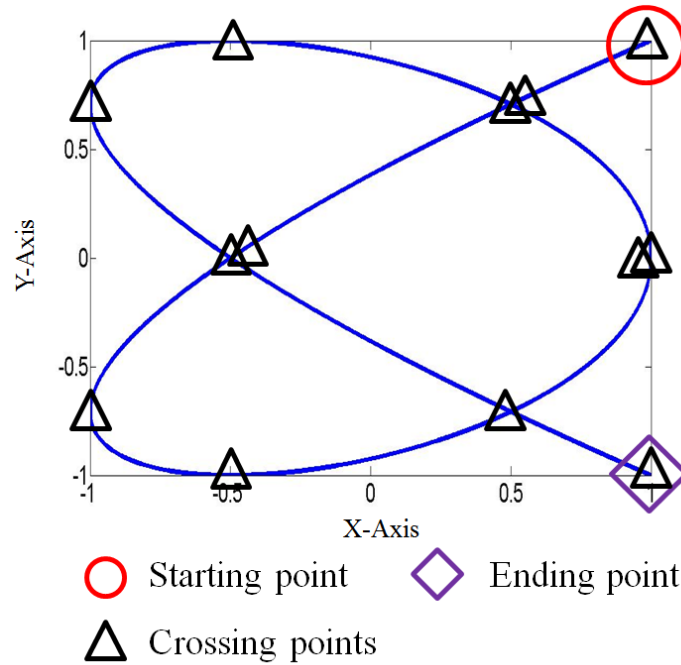
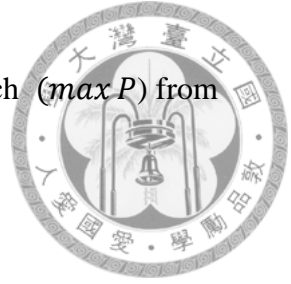


Fig. 4-5 Pitch points of the Lissajous scan trajectory with $n = 2$

For actual scanning applications, we must use higher values of n to generate sufficiently dense Lissajous trajectory, and an example with $n = 6$ is shown in Fig. 4-6. Because the lowest resolution of trajectory will occur at the center of the scanning area, and its shape is almost straight line, the maximum scan pitch satisfies the condition at the time $t = (n - 1)\delta$, $t = n\delta$ [46]. Thus, given the frequencies f_x and f_y , the coordinates of the two pitch points can be derived from Eqs. (4.3), (4.6) as follows:

$$\begin{cases} x_L|_{(n-1)\delta} \\ y_L|_{(n-1)\delta} \end{cases} \quad \text{and} \quad \begin{cases} x_L|_{n\delta} \\ y_L|_{n\delta} \end{cases} \quad (4.7)$$



Under such circumstance, we can obtain the maximum scan pitch ($max P$) from geometric computing by Eq. (4.7), and that can be formulated as:

$$max P = \sqrt{(x_L|_{n\delta} - x_L|_{(n-1)\delta})^2 + (y_L|_{n\delta} - y_L|_{(n-1)\delta})^2} \quad (4.8)$$

For an appropriate image resolution with $max P$ to project in x - and y -axis, which will satisfy the results of $max P_x$ and $max P_y$, as also shown in Fig. 4-6.

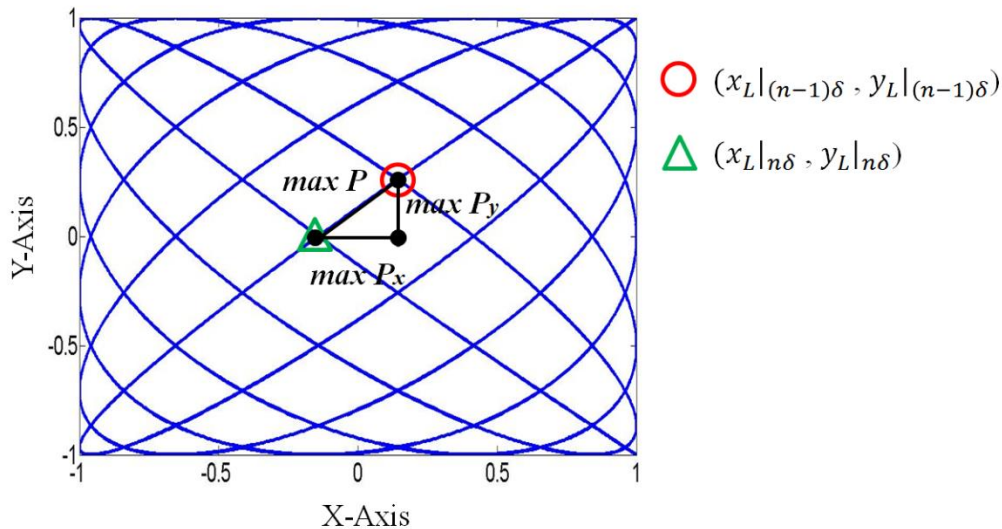


Fig. 4-6 Maximum scan pitch of the Lissajous scan trajectory with $n = 6$

4.2.2 Mapping Lissajous points to raster points

For raster scan trajectory, the image of sample surface topography can be generated from the measured data with pixel-by-pixel method by image processing software. However, unlike the raster trajectory, the linear velocity of Lissajous trajectory is not



identical, and thus the distance between two adjacent points of this scan method is variable along the scan path. In order to utilize image processing software for Lissajous scan trajectory, we need to map the Lissajous points along the Lissajous trajectory to the raster points or pixels along a standard grid. Fig. 4-7 shows a schematic diagram of placing the Lissajous points on top of the raster points.

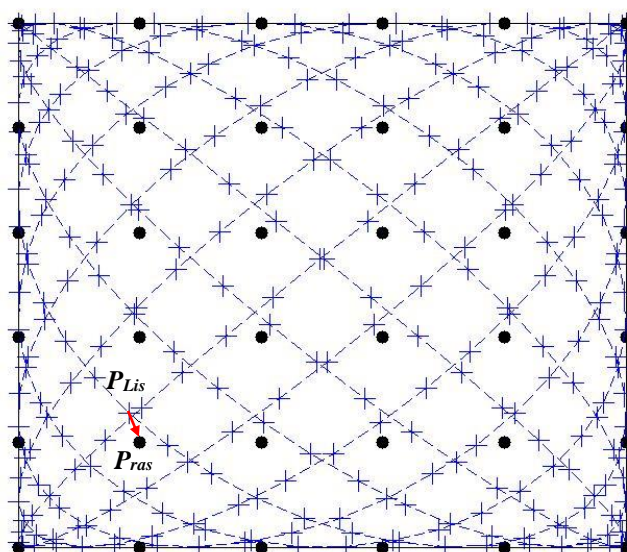
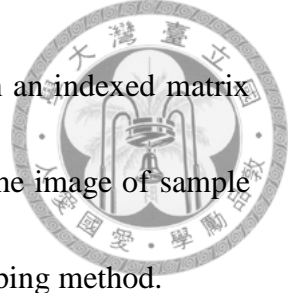


Fig. 4-7 Schematic diagram of placing the Lissajous points on top of the raster points

In the mapping procedure, the scan amplitude A and scan pitch P of both scan methods are set to be the same. Hence, the number of lines in the Lissajous trajectory will be equal to the number of lines in the raster scanned image. Then, each Lissajous point is mapped to the nearest raster point. Because the positions of raster and Lissajous points are known for every scan frequency and dimension, the corresponding nearest



Lissajous point of each raster point can be determined and saved in an indexed matrix before the scanning process. When the scan of sample is finished, the image of sample surface topography can thus be generated pixel-by-pixel by this mapping method.

Next, we need to analyze the mapping error when we map the Lissajous points to the raster points. The mapping error can be obtained by computing the magnitude of the position vector from the corresponding nearest Lissajous point to the raster point. An example of the position vector between a Lissajous point P_{Lis} and a raster point P_{ras} with coordinate index of (2,2) is shown in Fig. 4-7. The magnitude of this position vector can be calculated as

$$|\overrightarrow{P_{Lis}P_{ras}}(i,j)| = \sqrt{(P_{Lis}^x - P_{ras}^x)^2 + (P_{Lis}^y - P_{ras}^y)^2} \quad (4.9)$$

where $i = 2$ and $j = 2$. Since the image resolution is determined by the maximum pitch distance of the Lissajous trajectory to project in x - and y -axis, this mapping error can be neglected if which is less than the image resolution. Therefore, we can construct an image from the Lissajous sampled data by utilizing image processing software with this mapping procedure, and have the same resolution as that of the raster scanned image.

4.3 Lissajous Hierarchical Local Scan Algorithm



Conventionally, the scan region of AFM is a rectangular area, and the scanning probe must cross the overall location of scan area by an acceptable constant scan velocity. However, in many AFM applications, such as biological cells inspecting or nano-material measuring, there usually exists a large ratio of uninterested area in the scan region. Notice that the uninterested portion of the scan area implies the wasted time in unnecessary scanning. Besides, for constant velocity scanning without considering the situation where the sample topography many vary, this result lead to a bad image when the sample is subject to severe height variation. In this research, we propose a new Lissajous hierarchical Local scan method, with the aid of Lissajous scan trajectory, to remove the uninterested scan area in the first layer scan, followed by subsequent hierarchical scan strategy considering the height variation of sample topography in order to meet the demand of the image resolution. By employing this proposed method, we can effectively improve the scan image quality without substantially increasing the overall scan time. In this section, we will describe how to decide the necessary scan area by first layer scan algorithm. Furthermore, we consider the height varying of the scan area and then imitate the second or even higher layer scan algorithm to achieve higher image resolution.

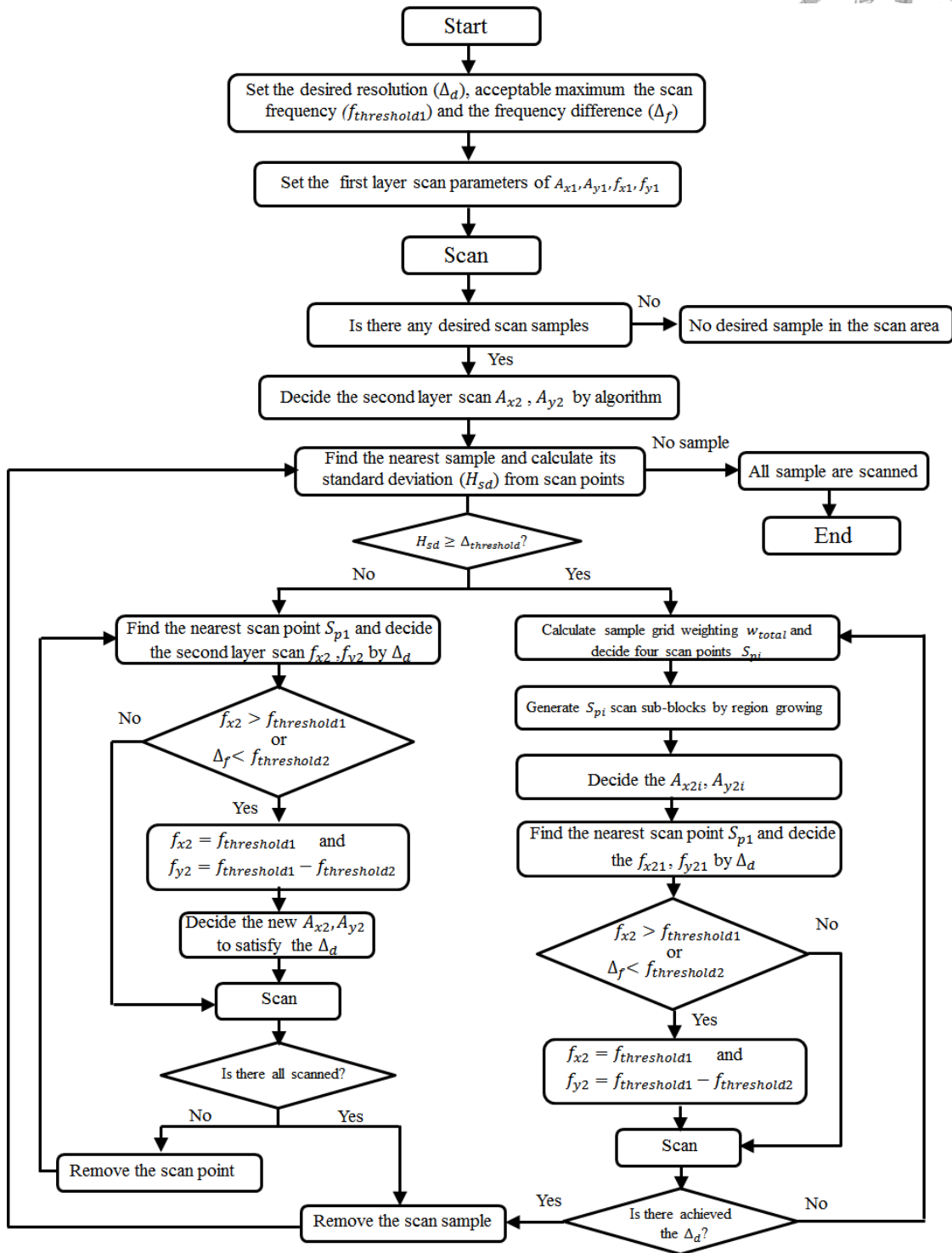
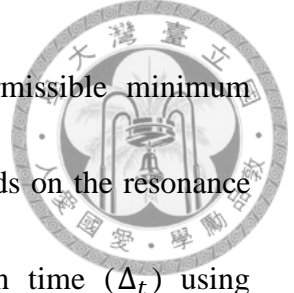


Fig. 4-8 The flow chart of the Lissajous hierarchical Local scan method

The flow chart of the Lissajous hierarchical Local scan method is shown in Fig. 4-8.

The purpose of this scan method is to obtain the desired resolution (Δ_d) given the



permissible maximum scan frequency ($f_{threshold1}$) and the permissible minimum frequency difference threshold ($f_{threshold2}$). The $f_{threshold1}$ depends on the resonance frequency of the x -scanner, and $f_{threshold2}$ will affect the scan time (Δ_t) using Lissajous trajectory, which can be divided into two parts for discussion. The first part is first layer scan for the desired sample size in the preset scan region, and the second part is to satisfy Δ_d in an acceptable $f_{threshold1}$ and $f_{threshold2}$ of the xy -hybrid scanner by second or higher layer scan. The detailed descriptions of the proposed scan algorithm will be presented in the next sub-sections.

4.3.1 First layer scan

Traditionally, we must set the probe tip close to the sample of interest during the AFM scanning. In order to scan every sample completely, the preset scan region must set to be large enough to cover all samples, and it turns out some unnecessary scan time is usually wasted. In this section, we will focus on the above-mentioned problem to improve seek possible improvement using our proposed first layer scan algorithm. According to Eq. (4.3), the first layer scan path can be planned as:

$$\begin{aligned}x_1(t_1) &= \frac{A_{x1}}{2} \cos(2\pi f_{x1} t_1) \\y_1(t_1) &= \frac{A_{y1}}{2} \cos(2\pi f_{y1} t_1)\end{aligned}\tag{4.10}$$



Over a reasonable preset scan region, there is a minimum size of the interested sample, say, Δ_s . In order to collect sufficient scan information to judge the variations of the sample topography, we choose sufficiently dense scan line such that the relationship between Δ_s and $\max P$ (the maximum scan pitch) is given as:

$$\frac{\Delta_s}{\max P} \geq 3 \quad (4.11)$$

By Eq. (4.3), we can reality determine the parameters f_{x1} and f_{y1} for performing the first layer scan. Under such circumstance, the maximum scan pitch which satisfies Eq. (4.11) indicates that each scan sample of interest can be crossed at least by six scan lines of a rectangular Lissajous scan trajectory. Intuitively, more scan line crossing the sample surface means that longer scanning time will be needed at the first layer scan. In the other hand, if there are too few scan line will unable to judge the height variation of the sample topography. Thus, we use the surface fitting method to estimate the height topography of a sample, which suggest that six or more scan lines will provide a reasonably good resolution for height information of the sample's topography. For this reason and considering the scan time, we barely so that design the Lissajous scan trajectory six scan lines will cross minimum size sample of interest in the first layer scan algorithm, but this density number is actually a design parameter for user in our scan algorithm.

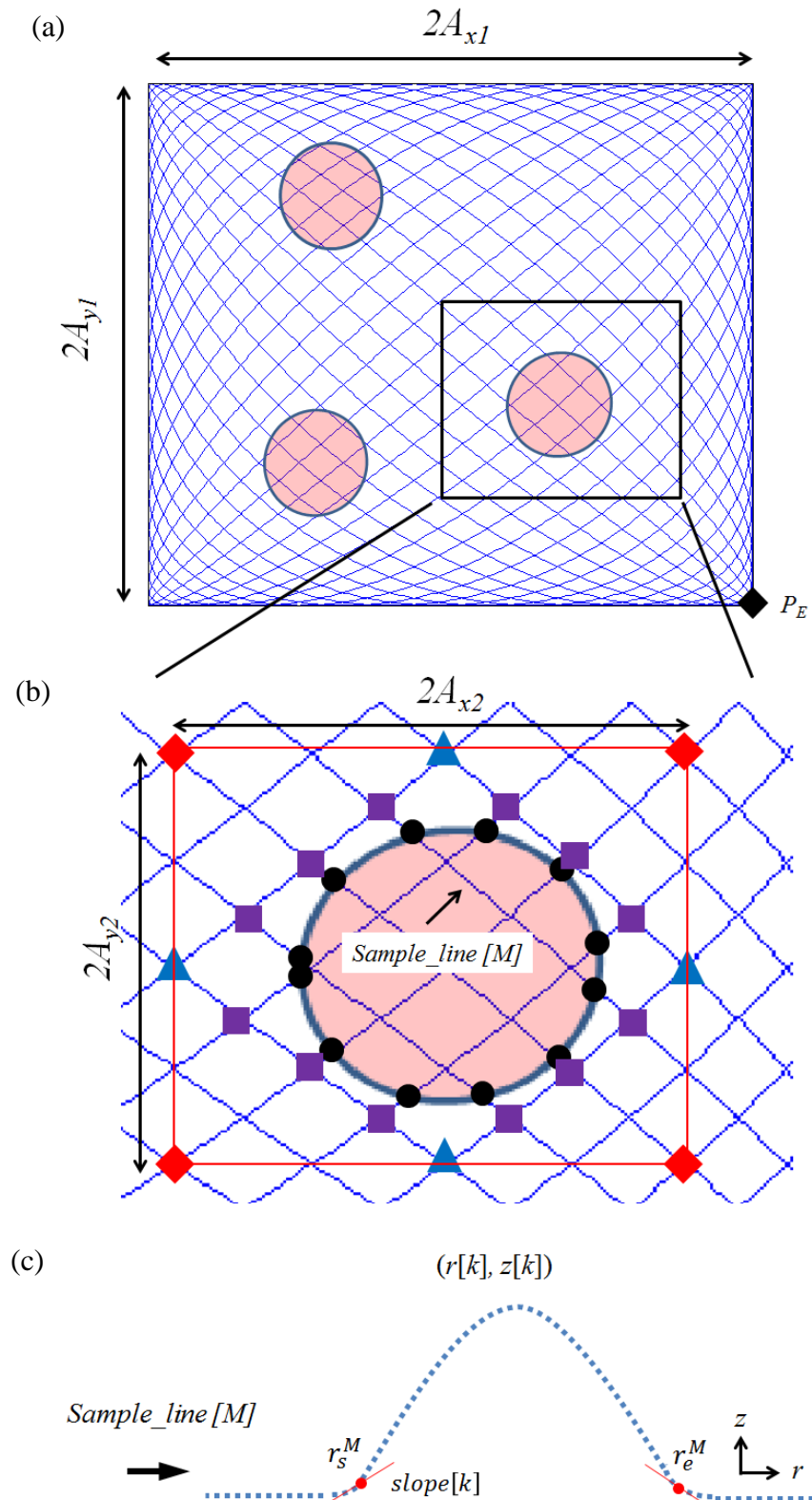
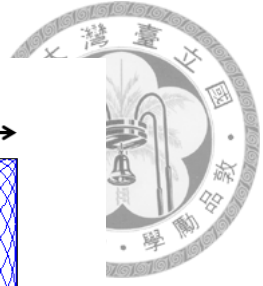


Fig. 4-9 (a) The schematic diagram of the Lissajous first layer scan, (b) the amplified diagram of (a) in the nearest sample, (c) the M -th scan line of nearest sample with height information.



In Fig. 4-9 (a), we show the scan plot of the first layer scan satisfying Eqs. (4.10) and (4.11), and Fig. 4-9 (b) shows a zoom-in plot of an interest sample nearest to the terminal point P_E of the first layer scan. In Fig. 4-9 (b), we choose in particular scan line with number M ($sample_{line[M]}$), which crosses that sample, and illustrate the scanned height profile along that scan line in Fig. 4-9 (c), where the profile is in the zr -plane, and r represents the distance variable along the scan line. Let the height information measured in z -axis be composed of a series of discrete measurement points, and the slope of the height profile at every discrete point, say, $slope[k]$, is approximated by:

$$slope[k] = \frac{z[k+1]-z[k]}{r[k+1]-r[k]}, \quad k \in 1, 2, \dots, n_k \quad (4.12)$$

where $slope[k]$ indicates the slope at the k -th sampling point of the scan line and n_k is the number of sampling points in one scan line. By this definition, when the tip does not contact the sample, the slope is close to zero, but the slope starts to vary when contact with is made. Therefore, all sampling points whose magnitudes of their slopes are greater than a preset threshold value will be marked as the margin points of the sample, denoted as $r^M[j]$, *i.e.*,

$$r^M[j] = r^M[k], \quad \text{for } |slope[k]| \geq \rho_m \text{ and } z[k] \leq \Delta_m, \quad j \in 1, 2, \dots, n_j \quad (4.13)$$

In whose ρ_m and Δ_m are the preset threshold values of the slope and the height, and



they are also the design parameters for user. Besides, along the line with number M the starting and the ending points respectively satisfying Eq. (4.13) can be described as:

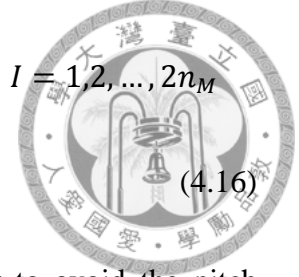
$$\begin{aligned} r_s^M &= r^M[1] \\ r_e^M &= r^M[n_j] \end{aligned} \quad (4.14)$$

where r_s^M and r_e^M serve as rising point and falling point, respectively, referring to Fig. 4-9 (c). From Eq. (4.11), every interested sample has at least six scan lines crossing its topography surface within the Lissajous rectangular scan area. Furthermore, each scan line contains the aforementioned rising point (r_s^M) and the falling point (r_e^M), which are marked by circles on the contour of the sample as shown in Fig. 4-9 (b). From sub-section 4.2.1, the Lissajous trajectory of first layer scan can obtain the coordinates of all pitch points (P_l) as shown below:

$$P_l = (x|_{l\delta_1}, y|_{l\delta_1}), \quad l \in 1, 2, \dots, n(n+1) + 1 \quad (4.15)$$

where δ_1 represents the time interval of scan pitch. Apparently, we will be able to find the coordinates of a pitch point outside the sample but nearest to every rising point or falling point on the contour of the sample. In other words, let r_u^M denote one of rising points or falling points, then:

$$P_I (r_u^M) = (x_I, y_I) = \underset{P_I}{\operatorname{argmin}} \|P_I - r_u^M\|_2, \quad \text{for } z(P_I) \leq \Delta_m, \quad I = 1, 2, \dots, 2n_M \quad (4.16)$$



where P_I is marked by square symbol in Fig. 4-9 (b). In order to avoid the pitch points selected are inside the sample, we design Δ_m as the threshold value for Eq. (4.16). By collecting P_I , we identify four of them, namely, $(\min x_I, y_I)$, $(\max x_I, y_I)$, $(x_I, \min y_I)$, $(x_I, \max y_I)$ and call each of the four P_I^* for destination. Finally, for the scan pitch P_I^* , we can readily search for the scan pitch points symbolized as P_{II} satisfying:

$$P_{II} = (x_{II}, y_{II}) = \underset{P_I}{\operatorname{argmin}} \|P_I - P_I^*\|_2, \quad \text{for } z(P_I) \leq \Delta_m, \quad II = 1 \sim 4 \quad (4.17)$$

which are marked by triangle symbols in Fig. 4-9 (b). Now, if we further define the four points, $(\max x_{II}, \min y_{II})$, $(\min x_{II}, \min y_{II})$, $(\min x_{II}, \max y_{II})$, $(\max x_{II}, \max y_{II})$ by the diamond symbols, then it is not hard to see from Fig. 4-9 (b) that these four pitch points span a rectangular region completely enclosing the sample.

To sum up in the first layer scan algorithm, we can get a minimum rectangle area to cover each interested sample based on the scan pitch points of the Lissajous trajectory, and further we can determine all scan amplitudes of the samples based on Lissajous scan trajectory in second layer scan as shown below:

$$A_{x2} = \frac{1}{2}(\max x_{II} - \min x_{II})$$

$$A_{y2} = \frac{1}{2}(\max y_{II} - \min y_{II})$$



(4.20)

The detailed description for second or higher layer scan will follow in the next section.

4.3.2 Second or higher layer scan

In the second layer scan, we consider the height variations of the samples at the scan points. Typically, the standard deviation is a good evaluation method to the varying degree of the sample topography. First, we assume the standard deviation of nearest sample at the scan points to be H_{sd} . Let the standard deviation threshold be set as $\Delta_{threshold}$. When $H_{sd} \leq \Delta_{threshold}$, it means the sample topography is smooth. On the contrary, when $H_{sd} > \Delta_{threshold}$ it implies the sample topography varies severely. Next, we will focus on these two situations.

Situation one: $H_{sd} \leq \Delta_{threshold}$

Since the sample topography is smooth, we do not need to consider the height variation of this sample at the scan points. For a quick scan in this situation, we first use the coordinates of the four scan points (P_{III}), and then, find the minimum distance between four scan points and ending point of first layer scan (P_E), the coordinate point can be defined as:

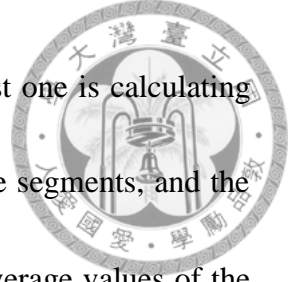
$$S_{n1} = \underset{P_{III}}{argmin} \|P_{III} - P_E\|_2 \quad (4.21)$$



By the specified A_{x2}, A_{y2} , and Δ_d , we can readily determine the scan frequency f_{x2} and f_{y2} in the second layer scan. Assume there exists a permissible the maximum scan frequency ($f_{threshold1}$) and the permissible minimum frequency difference threshold ($f_{threshold2}$). Since $f_{x2} > f_{y2}$ by Eq. (4.4), if $f_{x2} \leq f_{threshold1}$ and $\Delta_f \geq f_{threshold2}$, which means that the desired resolution (Δ_d) can be achieved within the acceptable maximum scan time (Δ_t) by the scan amplitude (A_{x2}, A_{y2}) and the scan frequency (f_{x2}, f_{y2}). Additionally, If $f_{x2} > f_{threshold1}$ or $\Delta_f < f_{threshold2}$, the desired Δ_d cannot be achieved. Therefore, for an acceptable scan performance, we use $f_{x2} = f_{threshold1}$, $f_{y2} = f_{threshold1} - f_{threshold2}$, and regulate the parameters of A_{x2}, A_{y2} with the new parameters of $A_{x2}(i), A_{y2}(i)$ by Eqs. (4.3) and (4.8) to meet the demand for achieving Δ_d . In this situation, the sample will be completely scanned until $A_{x2} = \sum_{i=1}^a A_{x2}(i)$ and $A_{y2} = \sum_{i=1}^a A_{y2}(i)$. The detailed scan procedure is shown in Fig. 4-8.

Situation two: $H_{sd} > \Delta_{threshold}$

When $H_{sd} > \Delta_{threshold}$, it means the variation of sample topography is out of our tolerance. Therefore, we need to consider the height variations by calculating the sum of all grating weighting of the sample (W_{total}). To explain grating weighting, referring to Fig. 4-10, it neglects the variation of the height information over the diamond shape confined by the four scan lines $line_{[1m]}^1, line_{[1m]}^2, line_{[1m]}^3, line_{[1m]}^4$, and it is donated



as W_{11} here. To compute W_{11} , there are two ways in general: First one is calculating the standard deviations of the height samples over the four scan line segments, and the results are H_{1m}^{sd1} , H_{1m}^{sd2} , H_{1m}^{sd3} , H_{1m}^{sd4} ; second one is calculate the average values of the same height samples over the four scan line segments, and obtain the results H_{1m}^{av1} , H_{1m}^{av2} , H_{1m}^{av3} , H_{1m}^{av4} .

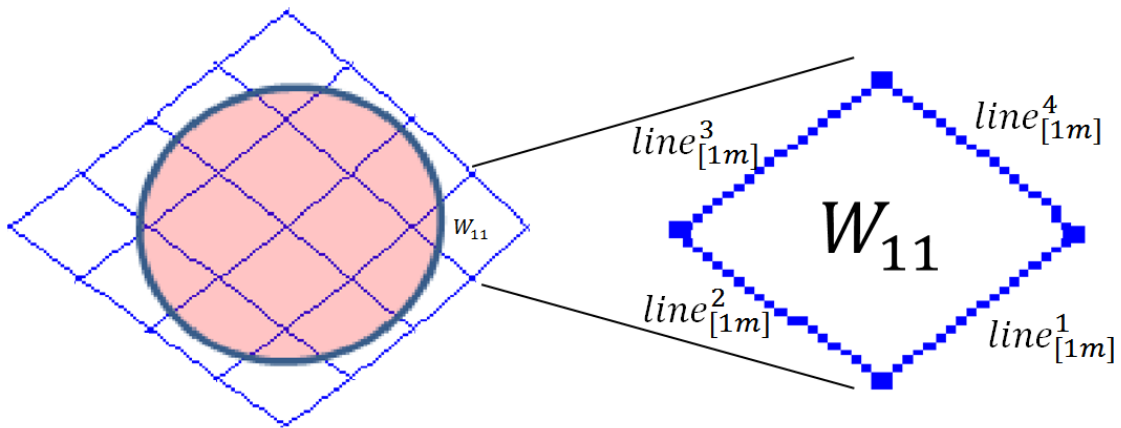


Fig. 4-10 The height variations by calculating the sample grating weighting.

For our system, prefer to use a mixed W_{11} to represent the grating weighting, *i.e.*,

$$W_{11} = \alpha H_{1m}^{sdw} + \beta H_{1m}^{avw} \tag{4.21}$$

where $H_{1m}^{sdw} = \frac{(H_{1m}^{sd1} + H_{1m}^{sd2} + H_{1m}^{sd3} + H_{1m}^{sd4})}{4}$ and $H_{1m}^{avw} = \frac{|H_{1m}^{av1} - H_{1m}^{av3}| + |H_{1m}^{av2} - H_{1m}^{av4}|}{2}$, and α and β are parameters to be designed by the user. By Eq. (4.21), we can obtain all weighting values of the sample as displayed in Fig. 4-11 (a).

Now, we try to sum all the weighting values of the sample and denote it as W_{total} , which can be expressed by $W_{total} = \sum_{d=1 \sim n}^{c=1 \sim n} W_{cd}$. By referring to the four vertex



points denoted as P_{III} , we can determine the coordinates of the middle points as S_{c1} , S_{c2} , S_{c3} , S_{c4} as shown in Fig. 4-11. Then, it is not hard to find the scan pitch points S_{pi} , such that S_{pi} is closest to S_{ci} , $i = 1 \sim 4$. Next, we try to choose one of the four scan pitch points to the ending points of the 1st layer scan, namely, and let it be the P_E as starting scan point for the 2nd layer scan. But incidentally we further employ the region growing method [48] by a pre-specified threshold Δ_W , which can be lead to the sub-block with a rectangular scan area $(2A_{x21}, 2A_{y21})$, as show in Fig. 4-11 (b). By A_{x21}, A_{y21} , and Δ_d , we can determine the scan frequency f_{x21} and f_{y21} in the sub-block. Assuming there exist an acceptable the maximum scan frequency ($f_{threshold1}$) and the minimum frequency difference ($f_{threshold2}$). If $f_{x2} \leq f_{threshold1}$ and $\Delta_f \geq f_{threshold2}$, the desired resolution Δ_d can be achieved within the maximum scan time (Δ_t) with the scan amplitude (A_{x21}, A_{y21}) and the scan frequency (f_{x21}, f_{y21}) . However, if $f_{x2} > f_{threshold1}$ or $\Delta_f < f_{threshold2}$, the resolution Δ_d cannot be achieved. In order to achieve an acceptable scan performance, we use $f_{x2} = f_{threshold1}$ and $f_{y2} = f_{threshold1} - f_{threshold2}$, which can acquire the scan resolution as Δ_{s1} in the second layer scan. In order to meet the desired resolution Δ_d , we must perform third or higher layer scan until the condition of $\Delta_{si} \geq \Delta_d$. The entire scan procedure can be found in Fig. 4-8.

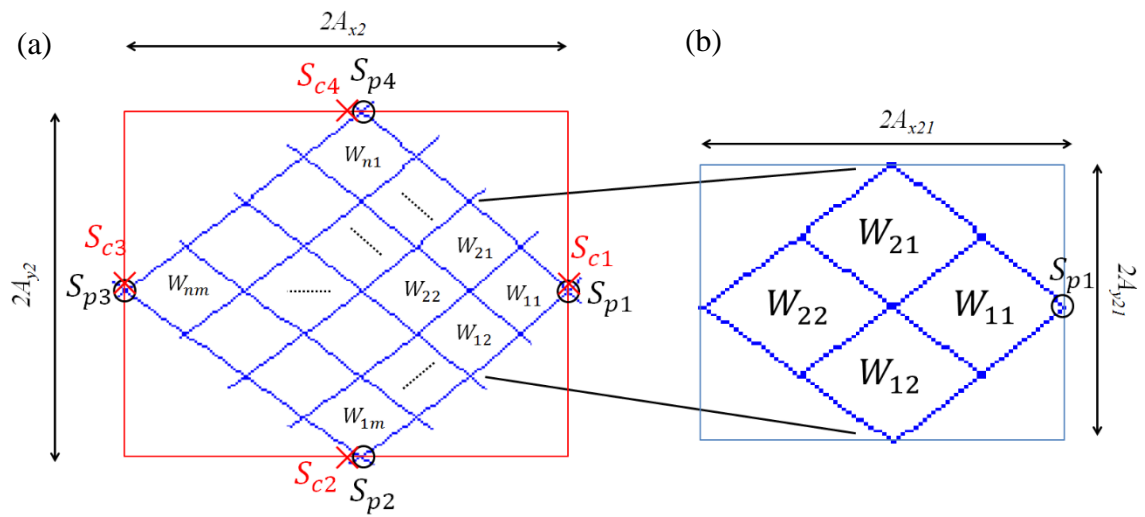


Fig. 4-11 (a) Calculate the sample all grating weighting and (b) generate the sub-block (blue rectangular area) by region growing

Chapter 5

Controller Design



In this chapter, the advanced controllers of the hybrid scanner, which consists of an xy -electromagnetic scanner and an xy -piezoelectric scanner, will be designed to realize the proposed hierarchical local scan method so as to achieve good AFM scanning performance. Since the characteristics of the Lissajous scan trajectory is well-known and simple, we can incorporate the internal model principle (IMP) into the design procedures of these controllers for tracking the scan trajectory well.

5.1 Scan Trajectory Assignment for xy -hybrid scanner

For the proposed Lissajous hierarchical local scan method as discussed in Chapter 4, by moving the sample and scan probe with xy -scanner, we achieve scanning of the sample surface with the assigned scan trajectory. The hybrid xy -scanner in our AFM system is composed of a large scan-range xy -electromagnetic scanner and a high bandwidth xy -piezoelectric scanner. However, from the system identification in



sub-section 3.3.3, although the xy -electromagnetic scanner has the advantage of large scan range, its scan bandwidth is only about 20 Hz. Contrarily, although the xy -piezoelectric scanner has the advantage of high bandwidth, its scan range is only $32\mu\text{m}\times 32\mu\text{m}$. For the purpose of obtaining both of the above advantages, the scan trajectory needs to be divided into two parts with respective permissible scan ranges in the xy -electromagnetic scanner and xy -piezoelectric scanner. According to Fig. 3-9, the Lissajous hierarchical local scan trajectory with i -th scan layer in half-period scan time (t_i) can be described as:

$$\begin{aligned}x(t_i) &= x_{em}(t_i) + x_{pz}(t_i) = x_{0i} + \frac{A_{xi}}{2} \cos(2\pi f_{xi} t_i) \\y(t_i) &= y_{em}(t_i) + y_{pz}(t_i) = y_{0i} + \frac{A_{yi}}{2} \cos(2\pi f_{yi} t_i)\end{aligned}\quad (5.1)$$

During the scan process, (x_{0i}, y_{0i}) donates the initial scan point. Among allowable motions of scan trajectory for xy -hybrid scanner, when the scan range is greater than $32\mu\text{m}$, it is the xy -electromagnetic scanner which will be employed to track the scan trajectory. In other word, if the scan range is less than $32\mu\text{m}$, it is the xy -piezoelectric scanner which will be need for high bandwidth tracking of the assigned scan trajectory. Therefore, the scan trajectory based on scan range (L_s) for i -th scan layer to xy -electromagnetic scanner and xy -piezoelectric scanner can be arranged as follows:



Scenario one: $L_s > 32\mu\text{m}$

$$\begin{cases} x_{em}(t_i) = x_{0i} + \frac{A_{xi}}{2} \cos(2\pi f_{xi} t_i) \\ y_{em}(t_i) = y_{0i} + \frac{A_{yi}}{2} \cos(2\pi f_{yi} t_i) \end{cases}, \quad \begin{cases} x_{pz}(t_i) = 0 \\ y_{pz}(t_i) = 0 \end{cases} \quad (5.2)$$

Scenario two: $L_s \leq 32\mu\text{m}$

$$\begin{cases} x_{em}(t_i) = x_{0i} \\ y_{em}(t_i) = y_{0i} \end{cases}, \quad \begin{cases} x_{pz}(t_i) = \frac{A_{xi}}{2} \cos(2\pi f_{xi} t_i) \\ y_{pz}(t_i) = \frac{A_{yi}}{2} \cos(2\pi f_{yi} t_i) \end{cases} \quad (5.3)$$

In the following sections, the advanced controller will be designed for the two scanners to track the assigned scan trajectories.

5.2 IMP based Adaptive Complementary Sliding Mode Control

The adaptive complementary sliding mode control (ACSMC) is an advanced control scheme, which combines the beneficial features of the adaptive control and complementary sliding mode control. The adaptive law provides the on-line estimation of the system parameters and adjusts the controller gain to deal with the modeling uncertainties and improve the performance. On the other hand, the complementary sliding mode control can improve the system robustness and reject the influence of



external disturbance effectively.

5.2.1 Problem formulation

During Lissajous hierarchical scanning process, the scan trajectories of the xy -electromagnetic scanner in both axes are cosine waveforms with different frequencies. The reference position vector X_{emr} of the xy -electromagnetic scanner in half-period scan time t_i of i -th scan layer will be one of the following forms:

$$X_{emr} = \left[x_{0i} + \frac{A_{xi}}{2} \cos(2\pi f_{xi} t_i) \quad y_{0i} + \frac{A_{yi}}{2} \cos(2\pi f_{yi} t_i) \right]^T \quad (5.4)$$

We can easily find that these reference position vectors satisfy the following dynamics:

$$\ddot{X}_{emr} + K_{emr} X_{emr} + C_{emr} = 0 \quad (5.5)$$

where $C_{emr} = \text{diag} \left[-x_{0i} (2\pi f_{xi})^2 \quad -y_{0i} (2\pi f_{yi})^2 \right]$ and $K_{emr} = \text{diag} \left[(2\pi f_{xi})^2 \quad (2\pi f_{yi})^2 \right]$ are diagonal matrices. Therefore, perfect tracking of the cosine waveform can be achieved by incorporating the reference model as an internal model into the closed-loop system of the xy -electromagnetic scanner according to internal model principle. Moreover, in consideration of system parameter uncertainties and external disturbance while scanning, we design an adaptive complementary sliding mode controller based on internal model principle (IMP) for the xy -electromagnetic scanner to track the cosine waveform trajectory precisely.

First, we divide the disturbance term D_{em} of Eq. (5.2) into constant uncertainty



and varying uncertainty terms, and rewrite the dynamic equation of the xy -electromagnetic scanner as follows:

$$\ddot{X}_{em} = K_{em}X_{em} + B_{em}\dot{X}_{em} + C_{em}U_{em} + D_c + D_v \quad (5.6)$$

where constant uncertainty $D_c = [d_{c1} \ d_{c2}]^T$ represents the model uncertainty, and time-varying uncertainty $D_v = [d_{v1} \ d_{v2}]^T$ represents the influence of external disturbance and coupling force from the piezoelectric scanner. Suppose the varying uncertainty is bounded and satisfy $\|D_v\|_\infty \leq \bar{d}$.

To begin with, incorporating the reference model in Eq. (5.5) as an internal model into the closed-loop system, the relationship between the tracking error vector E_{em} and the internal model state vector h_{em} can be obtained as follows:

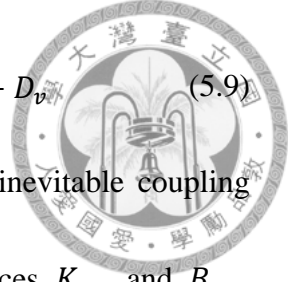
$$E_{em} = \dot{h}_{em} + K_{emr}h_{em} \quad (5.7)$$

The tracking error induced by the forced response of the reference trajectory with the form Eq. (5.5) would be zero according to Eq. (5.7). Hence, the rest of the problem is to design a controller to stabilize the closed-loop system with the internal model so that the tracking error induced by the natural response decays to zero as well.

Here, we define the tracking error vector without reference trajectory as:

$$E_{em} = 0 - X_{em} = [x_{em} \ y_{em}]^T \quad (5.8)$$

Substituting Eq. (5.8) into Eq. (5.6), we can obtain the error dynamics as below:



$$\ddot{E}_{em} = -\ddot{X}_{em} = -K_{em}X_{em} - B_{em}\dot{X}_{em} - C_{em}U_{em} - D_c - D_v \quad (5.9)$$

which shows that this plant is treated as an MIMO system. The inevitable coupling effect is regarded as the off-diagonal terms in the coefficient matrices K_{em} and B_{em} , which will be estimated by the adaptive algorithm. Substituting Eq. (5.9) into Eq. (5.7), the internal model state dynamics are obtained as:

$$\dot{h}_{em}^{(4)} = -K_{em}X_{em} - B_{em}\dot{X}_{em} - C_{em}U_{em} - D_c - D_v - K_{emr}\dot{h}_{em} \quad (5.10)$$

Next, we need to design a proper control input vector U_{em} such that the closed-loop system with the internal model is exponentially stable.

5.2.2 Control algorithm

The schematic diagram of the proposed IMP based ACSMC for cosine waveform tracking of the xy -electromagnetic scanner is shown in Fig. 5-1.

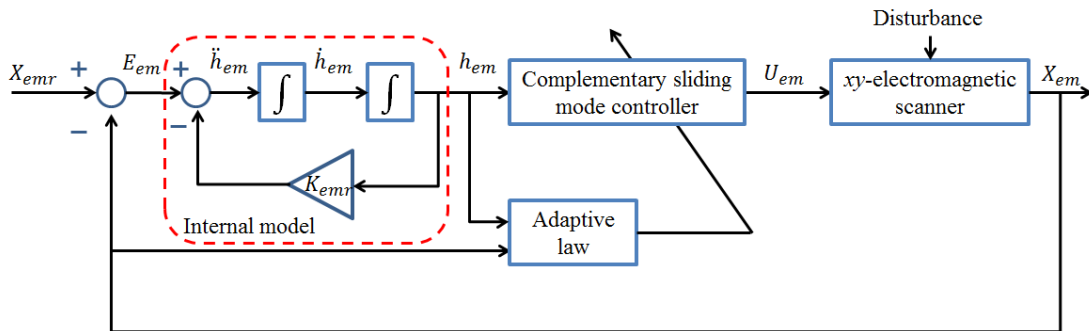


Fig. 5-1 The schematic diagram of internal model principle based adaptive complementary sliding mode control

First, we define the generalized sliding surface S_{em} and the complementary



sliding surface S_{emc} as the follows:

$$\begin{aligned}
 S_{em} &= \ddot{h}_{em} + 4\Lambda_{em}\dot{h}_{em} + 6\Lambda_{em}^2 h_{em} + 4\Lambda_{em}^3 h_{em} + \Lambda_{em}^4 H_{em} \\
 &= [S_{em1} \quad S_{em2}]^T
 \end{aligned} \tag{5.11}$$

$$\begin{aligned}
 S_{emc} &= \ddot{h}_{em} + 2\Lambda_{em}\dot{h}_{em} - 2\Lambda_{em}^3 h_{em} - \Lambda_{em}^4 H_{em} \\
 &= [S_{emc1} \quad S_{emc2}]^T
 \end{aligned} \tag{5.12}$$

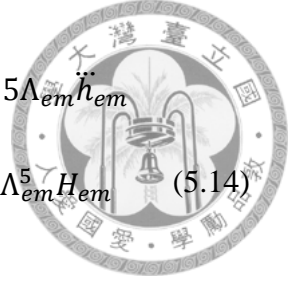
where $\Lambda_{em} = \text{diag}[\lambda_{em1} \quad \lambda_{em2}]$ is a positive diagonal matrix to be designed and

$H_{em}(t) = \int_0^t h_{em}(\tau) d\tau$. Here, S_{em} and S_{emc} have the following relationship:

$$\dot{S}_{emc} + \Lambda_{em}(S_{em} + S_{emc}) = \dot{S}_{em} \tag{5.13}$$

From Eq. (5.11) and Eq. (5.12), we can easily find that S_{em} and S_{emc} consist of the internal model state term, and its derivative as well as its integral terms. The main purpose is to drive both the sliding surface and complementary sliding surface variables to zero so that we can ensure h_{em} , \dot{h}_{em} and \ddot{h}_{em} will simultaneously converge to zero as well.

The developed ACSMC can provide on-line estimation of system parameters and tuning of controller gains to accommodate the environmental changes. According to the dynamics of sliding surface and complementary sliding surface, the control law is designed as



$$\begin{aligned}
U_{em} = \hat{C}_{em}^{-1} & [-\hat{K}_{em}X_{em} - \hat{B}_{em}\dot{X}_{em} - \hat{D}_c - K_{emr}\ddot{h}_{em} + 5\Lambda_{em}\ddot{h}_{em} \\
& + 10\Lambda_{em}^2\ddot{h}_{em} + 10\Lambda_{em}^3\dot{h}_{em} + 5\Lambda_{em}^4h_{em} + \Lambda_{em}^5H_{em} \\
& + G_{em}sgn(S_{em} + S_{emc})] \quad (5.14)
\end{aligned}$$

where \hat{C}_{em} , \hat{K}_{em} , \hat{B}_{em} , and \hat{D}_c are the estimated value of C_{em} , K_{em} , B_{em} , and D_c , respectively, $G_{em} \equiv \text{diag}[g_{em1} \ g_{em2}]$, $\forall g_{emi} > 0$, is the high gain such that $g_{em1}, g_{em2} > \bar{d}$.

However, the use of hard switching sign function $sgn(S_{em} + S_{emc})$ in the control law would lead to chattering phenomenon of the control input, which may excite resonant modes of the system. Hence, similarly we use a soft switching saturation function $sat(S_{em} + S_{emc})$ as defined in the following instead of the hard switching term:

$$sat(S_{em} + S_{emc}) \equiv [sat(s_{em1} + s_{emc1}) \quad sat(s_{em2} + s_{emc2})]^T \quad (5.15)$$

$$\text{where } sat(s_{emi} + s_{emci}) = \begin{cases} 1 & s_{emi} + s_{emci} > \varepsilon_{em} \\ \frac{s_{emi} + s_{emci}}{\varepsilon_{em}} & -\varepsilon_{em} \leq s_{emi} + s_{emci} \leq \varepsilon_{em} \text{ and } \varepsilon_{em} \\ -1 & s_{emi} + s_{emci} < -\varepsilon_{em} \end{cases}$$

is a small positive parameter to adjust the rate of switching operation. Eq. (5.14) then can be expressed as

$$\begin{aligned}
U_{em} = \hat{C}_{em}^{-1} & [-\hat{K}_{em}X_{em} - \hat{B}_{em}\dot{X}_{em} - \hat{D}_c - K_{emr}\ddot{h}_{em} + 5\Lambda_{em}\ddot{h}_{em} \\
& + 10\Lambda_{em}^2\ddot{h}_{em} + 10\Lambda_{em}^3\dot{h}_{em} + 5\Lambda_{em}^4h_{em} + \Lambda_{em}^5H_{em} \\
& + G_{em}sat(S_{em} + S_{emc})] \quad (5.16)
\end{aligned}$$



5.2.3 Stability analysis

Define a Lyapunov function candidate V_{em} with the following form, which is a positive definite function:

$$\begin{aligned}
 V_{em} = & \frac{1}{2} S_{em}^T S_{em} + \frac{1}{2} S_{emc}^T S_{emc} + \frac{1}{2} \text{tr} \left(\tilde{K}_{em}^T \Gamma_1^{-1} \tilde{K}_{em} \right) \\
 & + \frac{1}{2} \text{tr} \left(\tilde{B}_{em}^T \Gamma_2^{-1} \tilde{B}_{em} \right) + \frac{1}{2} \text{tr} \left(\tilde{C}_{em}^T \Gamma_3^{-1} \tilde{C}_{em} \right) \\
 & + \frac{1}{2} \text{tr} \left(\tilde{D}_c^T \Gamma_4^{-1} \tilde{D}_c \right)
 \end{aligned} \tag{5.17}$$

where $\Gamma_i = \text{diag}[\gamma_{i1}, \gamma_{i2}]$, $i = 1 \sim 4$, are all positive diagonal matrices, $\text{tr}(\cdot)$ is the trace of a matrix. \tilde{K}_{em} , \tilde{B}_{em} , \tilde{C}_{em} , and \tilde{D}_c are the estimation errors, which are defined as $\tilde{K}_{em} = K_{em} - \hat{K}_{em}$, $\tilde{B}_{em} = B_{em} - \hat{B}_{em}$, $\tilde{C}_{em} = C_{em} - \hat{C}_{em}$, and $\tilde{D}_c = D_c - \hat{D}_c$.

Take the time derivative of the Lyapunov function candidate, we can obtain

$$\begin{aligned}
 \dot{V}_{em} = & S_{em}^T \dot{S}_{em} + S_{emc}^T \dot{S}_{emc} + \text{tr} \left(\tilde{K}_{em}^T \Gamma_1^{-1} \dot{\tilde{K}}_{em} \right) \\
 & + \text{tr} \left(\tilde{B}_{em}^T \Gamma_2^{-1} \dot{\tilde{B}}_{em} \right) + \text{tr} \left(\tilde{C}_{em}^T \Gamma_3^{-1} \dot{\tilde{C}}_{em} \right) \\
 & + \text{tr} \left(\tilde{D}_c^T \Gamma_4^{-1} \dot{\tilde{D}}_c \right)
 \end{aligned} \tag{5.18}$$

According to Eq. (5.13), the first two terms of Eq. (5.18) can be rewritten as

$$\begin{aligned}
 & S_{em}^T \dot{S}_{em} + S_{emc}^T \dot{S}_{emc} \\
 = & S_{em}^T \dot{S}_{em} + S_{emc}^T \left[\dot{S}_{em} - \Lambda_{em} (S_{em} + S_{emc}) \right] \\
 = & (S_{em} + S_{emc})^T (\dot{S}_{em} - \Lambda_{em} S_{emc}) \\
 = & -(S_{em} + S_{emc})^T \Lambda_{em} (S_{em} + S_{emc})
 \end{aligned} \tag{5.19}$$



$$+(S_{em} + S_{emc})^T (\dot{S}_{em} + \Lambda_{em} S_{em})$$

Here, $\dot{S}_{em} + \Lambda_{em} S_{em}$ can be reformulated by Eq. (5.10), Eq. (5.11) and Eq. (5.16) as

$$\begin{aligned}
& \dot{S}_{em} + \Lambda_{em} S_{em} \\
&= h_{em}^{(4)} + 5\Lambda_{em} \ddot{h}_{em} + 10\Lambda_{em}^2 \dot{h}_{em} + 10\Lambda_{em}^3 h_{em} + 5\Lambda_{em}^4 h_{em} \\
& \quad + \Lambda_{em}^5 H_{em} \\
&= -K_{em} X_{em} - B_{em} \dot{X}_{em} - C_{em} U_{em} - D_c - D_v - K_{emr} \dot{h}_{em} + 5\Lambda_{em} \ddot{h}_{em} \\
& \quad + 10\Lambda_{em}^2 \dot{h}_{em} + 10\Lambda_{em}^3 h_{em} + 5\Lambda_{em}^4 h_{em} + \Lambda_{em}^5 H_{em} \\
&= -(\tilde{K}_{em} + \tilde{K}_{em}) X_{em} - (\tilde{B}_{em} + \tilde{B}_{em}) \dot{X}_{em} \\
& \quad - (\tilde{C}_{em} + \tilde{C}_{em}) \tilde{C}_{em}^{-1} [-\tilde{K}_{em} X_{em} - \tilde{B}_{em} \dot{X}_{em} - \tilde{D}_c + 5\Lambda_{em} \ddot{h}_{em} \\
& \quad + 10\Lambda_{em}^2 \dot{h}_{em} + 10\Lambda_{em}^3 h_{em} + 5\Lambda_{em}^4 h_{em} + \Lambda_{em}^5 H_{em} \\
& \quad + G_{em} \text{sat}(S_{em} + S_{emc})] - (\tilde{D}_c + \tilde{D}_c) - D_v - K_{emr} \dot{h}_{em} + 5\Lambda_{em} \ddot{h}_{em} \\
& \quad + 10\Lambda_{em}^2 \dot{h}_{em} + 10\Lambda_{em}^3 h_{em} + 5\Lambda_{em}^4 h_{em} + \Lambda_{em}^5 H_{em} \\
&= -\tilde{K}_{em} X_{em} - \tilde{B}_{em} \dot{X}_{em} - \tilde{C}_{em} U_{em} - \tilde{D}_c - D_v \\
& \quad - G_{em} \text{sat}(S_{em} + S_{emc})
\end{aligned} \tag{5.20}$$

Then, we can substitute Eq. (5.19) and Eq. (5.20) into Eq. (5.18), and applying the following trace operations:

$$a. \text{tr}(AB) = \text{tr}(BA), \quad \text{for any } A, B \in R^{n \times n}$$

$$b. \text{tr}(A + B) = \text{tr}(B + A), \quad \text{for any } A, B \in R^{n \times n}$$



$$c. \text{tr}(AB^T) = \text{tr}(BA^T) = A^T B = B^T A, \quad \text{for any } A, B \in \mathbb{R}^{n \times 1}$$

so that Eq. (5.18) can be rewritten as the following expression:

$$\begin{aligned} \dot{V}_{em} = & -(S_{em} + S_{emc})^T \Lambda_{em} (S_{em} + S_{emc}) \\ & -(S_{em} + S_{emc})^T [G_{em} \text{sat}(S_{em} + S_{emc}) + D_v] \\ & + \text{tr} \left[-\tilde{K}_{em}^T \left(\Gamma_1^{-1} \dot{\tilde{K}}_{em} + (S_{em} + S_{emc}) \dot{X}_{em}^T \right) \right] \\ & + \text{tr} \left[-\tilde{B}_{em}^T \left(\Gamma_2^{-1} \dot{\tilde{B}}_{em} + (S_{em} + S_{emc}) \dot{X}_{em}^T \right) \right] \\ & + \text{tr} \left[-\tilde{C}_{em}^T \left(\Gamma_3^{-1} \dot{\tilde{C}}_{em} + (S_{em} + S_{emc}) \dot{U}_{em}^T \right) \right] \\ & + \text{tr} \left[-\tilde{D}_c^T \left(\Gamma_4^{-1} \dot{\tilde{D}}_c + (S_{em} + S_{emc}) \right) \right] \end{aligned} \quad (5.21)$$

By using the σ -modification [49] to establish the boundedness in the presence of modeling error and choose the robust adaptive laws in the following form:

$$\begin{aligned} \dot{\hat{K}}_{em} = \dot{\tilde{K}}_{em} &= -\Gamma_1 (S_{em} + S_{emc}) X_{em}^T - \Gamma_1 \Sigma_1 \hat{K}_{em} \\ \dot{\hat{B}}_{em} = \dot{\tilde{B}}_{em} &= -\Gamma_2 (S_{em} + S_{emc}) \dot{X}_{em}^T - \Gamma_2 \Sigma_2 \hat{B}_{em} \\ \dot{\hat{C}}_{em} = \dot{\tilde{C}}_{em} &= -\Gamma_3 (S_{em} + S_{emc}) \dot{U}_{em}^T - \Gamma_3 \Sigma_3 \hat{C}_{em} \\ \dot{\hat{D}}_c = \dot{\tilde{D}}_c &= -\Gamma_4 (S_{em} + S_{emc}) - \Gamma_4 \Sigma_4 \hat{D}_c \end{aligned} \quad (5.22)$$

where $\Sigma_i = \text{diag}[\sigma_{i1}, \sigma_{i2}]$, $i = 1 \sim 4$, are all positive diagonal matrices. Substitute Eq.

(5.22) into Eq. (5.21), then we obtain

$$\begin{aligned} \dot{V}_{em} = & -(S_{em} + S_{emc})^T \Lambda_{em} (S_{em} + S_{emc}) \\ & -(S_{em} + S_{emc})^T [G_{em} \text{sat}(S_{em} + S_{emc}) + D_v] \end{aligned} \quad (5.23)$$

$$+ \sum_{i=1}^2 \sum_{j=1}^2 [\sigma_{1i} \tilde{k}_{ij} \hat{k}_{ij} + \sigma_{2i} \tilde{b}_{ij} \hat{b}_{ij} + \sigma_{3i} \tilde{c}_{ij} \hat{c}_{ij} + \sigma_{4i} \tilde{d}_{ij} \hat{d}_{ij}]$$

Here, we utilize completion of squares and then the sign indeterminate term in Eq. (5.23)

satisfies

$$\begin{aligned} \sigma_{1i} \tilde{k}_{ij} \hat{k}_{ij} &= \sigma_{1i} \tilde{k}_{ij} (k_{ij} - \tilde{k}_{ij}) \\ &\leq -\sigma_{1i} |\tilde{k}_{ij}|^2 + \sigma_{1i} |\tilde{k}_{ij}| \cdot |k_{ij}| \\ &\leq -\frac{\sigma_{1i}}{2} |\tilde{k}_{ij}|^2 - \frac{\sigma_{1i}}{2} (|\tilde{k}_{ij}| - |k_{ij}|)^2 + \frac{\sigma_{1i}}{2} |k_{ij}|^2 \\ &\leq \frac{\sigma_{1i}}{2} |k_{ij}|^2 \end{aligned} \quad (5.24)$$

A similar inequality can also be obtained for $\sigma_{2i} \tilde{b}_{ij} \hat{b}_{ij}$, $\sigma_{3i} \tilde{c}_{ij} \hat{c}_{ij}$ and $\sigma_{4i} \tilde{d}_{ij} \hat{d}_{ij}$, respectively. Substituting these inequalities into Eq. (5.23), we can find that \dot{V}_{em} satisfies the following inequality:

$$\begin{aligned} \dot{V}_{em} &\leq -\sum_{i=1}^2 \lambda_{emi} (s_{emi} + s_{emci})^2 \\ &\quad - \sum_{i=1}^2 (s_{emi} + s_{emci}) [g_{emi} \text{sat}(s_{emi} + s_{emci}) + d_{vi}] \\ &\quad + \frac{1}{2} \sum_{i=1}^2 \sum_{j=1}^2 [\sigma_{1i} |k_{ij}|^2 + \sigma_{2i} |b_{ij}|^2 + \sigma_{3i} |c_{ij}|^2 + \sigma_{4i} |d_{ij}|^2] \end{aligned} \quad (5.25)$$

Because complementary sliding mode control scheme with saturation function belongs to boundary layer control, the analysis of parameters $s_{emi} + s_{emci}$ inside or outside the boundary layer ε_{em} should be taken into consideration. To begin with, considering the complementary sliding variables are outside the boundary layer, i.e, $|s_{emi} + s_{emci}| > \varepsilon_{em}$, the saturation function can be readily replaced by the sign



function. So, the element of the second term in Eq. (5.25) can be expressed as follows

and satisfy the inequality:

$$\begin{aligned}
& (s_{emi} + s_{emci})[g_{emi} \text{sat}(s_{emi} + s_{emci}) + d_{vi}] \\
&= (s_{emi} + s_{emci})[g_{emi} \text{sgn}(s_{emi} + s_{emci}) + d_{vi}] \\
&= |s_{emi} + s_{emci}| g_{emi} + (s_{emi} + s_{emci}) d_{vi} \\
&\geq |s_{emi} + s_{emci}| (g_{emi} - \bar{d})
\end{aligned} \tag{5.26}$$

whereby, Eq. (5.25) can be rewritten as:

$$\begin{aligned}
\dot{V}_{em} &\leq -\sum_{i=1}^2 \lambda_{emi} (s_{emi} + s_{emci})^2 \\
&\quad - \sum_{i=1}^2 |s_{emi} + s_{emci}| (g_{emi} - \bar{d}) \\
&\quad + \frac{1}{2} \sum_{i=1}^2 \sum_{j=1}^2 [\sigma_{1i} |k_{ij}|^2 + \sigma_{2i} |b_{ij}|^2 + \sigma_{3i} |c_{ij}|^2 + \sigma_{4i} |d_{ij}|^2]
\end{aligned} \tag{5.27}$$

Since $g_{emi} > \bar{d}$, Eq. (5.27) becomes

$$\begin{aligned}
\dot{V}_{em} &\leq -\sum_{i=1}^2 \lambda_{emi} (s_{emi} + s_{emci})^2 \\
&\quad + \frac{1}{2} \sum_{i=1}^2 \sum_{j=1}^2 [\sigma_{1i} |k_{ij}|^2 + \sigma_{2i} |b_{ij}|^2 + \sigma_{3i} |c_{ij}|^2 + \sigma_{4i} |d_{ij}|^2]
\end{aligned} \tag{5.28}$$

Next, consider the complementary sliding variables which are inside the boundary layer, i.e. $|s_{emi} + s_{emci}| \leq \varepsilon_{em}$, the saturation function will be replaced by $\frac{s_{emi} + s_{emci}}{\varepsilon_{em}}$.

Hence, the element of the second term in Eq. (5.25) can be expressed as follows and satisfies the inequality:



$$\begin{aligned}
& (s_{emi} + s_{emci})[g_{emi} \text{sat}(s_{emi} + s_{emci}) + d_{vi}] \\
&= (s_{emi} + s_{emci}) \left[g_{emi} \left(\frac{s_{emi} + s_{emci}}{\varepsilon_{em}} \right) + d_{vi} \right] \\
&= \frac{g_{emi}}{\varepsilon_{em}} (s_{emi} + s_{emci})^2 + (s_{emi} + s_{emci}) d_{vi} \\
&\geq \frac{g_{emi}}{\varepsilon_{em}} |s_{emi} + s_{emci}|^2 - \bar{d} |s_{emi} + s_{emci}| \tag{5.29} \\
&= \frac{g_{emi}}{\varepsilon_{em}} |s_{emi} + s_{emci}|^2 - \bar{d} |s_{emi} + s_{emci}| + \frac{\varepsilon_{em}}{4g_{emi}} \bar{d}^2 - \frac{\varepsilon_{em}}{4g_{emi}} \bar{d}^2 \\
&= \left(\sqrt{\frac{g_{emi}}{\varepsilon_{em}}} |s_{emi} + s_{emci}| - \frac{1}{2} \sqrt{\frac{\varepsilon_{em}}{g_{emi}}} \bar{d} \right)^2 - \frac{\varepsilon_{em}}{4g_{emi}} \bar{d}^2
\end{aligned}$$

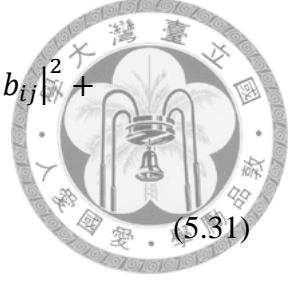
Thus, \dot{V}_{em} can be rewritten as:

$$\begin{aligned}
\dot{V}_{em} &\leq - \sum_{i=1}^2 \lambda_{emi} (s_{emi} + s_{emci})^2 \\
&\quad - \sum_{i=1}^2 \left[\left(\sqrt{\frac{g_{emi}}{\varepsilon_{em}}} |s_{emi} + s_{emci}| - \frac{1}{2} \sqrt{\frac{\varepsilon_{em}}{g_{emi}}} \bar{d} \right)^2 - \frac{\varepsilon_{em}}{4g_{emi}} \bar{d}^2 \right] \\
&\quad + \frac{1}{2} \sum_{i=1}^2 \sum_{j=1}^2 \left[\sigma_{1i} |k_{ij}|^2 + \sigma_{2i} |b_{ij}|^2 + \sigma_{3i} |c_{ij}|^2 + \sigma_{4i} |d_{ij}|^2 \right] \tag{5.30} \\
&\leq - \sum_{i=1}^2 \lambda_{emi} (s_{emi} + s_{emci})^2 + \sum_{i=1}^2 \left[\frac{\varepsilon_{em}}{4g_{emi}} \bar{d}^2 \right] \\
&\quad + \frac{1}{2} \sum_{i=1}^2 \sum_{j=1}^2 \left[\sigma_{1i} |k_{ij}|^2 + \sigma_{2i} |b_{ij}|^2 + \sigma_{3i} |c_{ij}|^2 + \sigma_{4i} |d_{ij}|^2 \right]
\end{aligned}$$

After considering two conditions about $s_{emi} + s_{emci}$ with respect to the boundary layer, we can conclude the most conservative stability by Eq. (5.28) and Eq. (5.30).

According to Lyapunov stability theorem, when

$$\begin{aligned} \sum_{i=1}^2 \lambda_{emi} (s_{emi} + s_{emci})^2 &\geq \frac{1}{2} \sum_{i=1}^2 \sum_{j=1}^2 \left[\sigma_{1i} |k_{ij}|^2 + \sigma_{2i} |b_{ij}|^2 + \right. \\ &\left. \sigma_{3i} |c_{ij}|^2 + \sigma_{4i} |d_{ij}|^2 + \frac{\varepsilon_{em}}{4g_{emi}} \bar{d}^2 \right] \end{aligned} \quad (5.31)$$



then

$$\dot{V}_{em} \leq 0$$

which implies that $V_{em}, \dot{V}_{em} \in L_\infty$ and thus $S_{em}, S_{emc}, \tilde{K}_{em}, \tilde{B}_{em}, \tilde{C}_{em}, \tilde{D}_c \in L_\infty$.

Hence, $\ddot{h}_{em}, \dot{h}_{em}, \dot{h}_{em}, h_{em} \in L_\infty$ and $E_{em}, \dot{E}_{em} \in L_\infty$ according to Eq. (5.9).

Moreover, we can further verify that $|E_{em}(t)|$ will converge to a residual set whose size is related to $\sigma_{ij}, \frac{\varepsilon_{em}}{g_{emi}}$.

5.3 IMP based Neural Network Complementary

Sliding Mode Control

The neural network complementary sliding model control (NNCSMC) is an advanced control scheme, which combines the advantages of two different control methods. The neural network is featured with the ability to model complex relationships between inputs and outputs and approximate nonlinear behaviors. On the other hand, the complementary sliding mode control can improve system robustness and then reduce the influence of external disturbance effectively. Furthermore, compared with



conventional sliding mode control [50], this control scheme can reduce the guaranteed ultimate bound of the tracking error by half and improve the tracking performance [51].

5.3.1 Problem formulation

During the Lissajous scanning process, the main task of xy -piezoelectric scanner is to track the motion of two single-frequency cosine waveforms while the xy -electromagnetic scanner is regulated at the desired position. Thus, the reference position vector of the xy -piezoelectric scanner will be one of the following forms:

$$X_{pZR} = \left[\frac{A_{xi}}{2} \cos(2\pi f_{xi} t_i) \quad \frac{A_{yi}}{2} \cos(2\pi f_{yi} t_i) \right]^T \quad (5.32)$$

It's easy to find that these reference position vectors satisfy the following dynamical equation:

$$\ddot{X}_{pZR} + K_{pZR} X_{pZR} = 0 \quad (5.33)$$

where $K_{pZR} = \text{diag} \left[(2\pi f_{xi})^2 \quad (2\pi f_{yi})^2 \right]$ is a diagonal matrix. Ideally, perfect tracking can be achieved by incorporating the reference model as an internal model into the closed-loop system according to internal model principle. However, since the piezoelectric scanner has hysteresis effect and external disturbance in the scanning process, we design a neural network complementary sliding model controller based on internal model principle to achieve precision tracking of the cosine waveform for the xy -piezoelectric scanner.



The hysteresis effect is caused by the nonlinear restoring force of piezoelectric actuator, which is an unknown variable since we do not have appropriate force sensor to measure it. Hence, we design a radial basis function neural network based model-free controller to compensate the hysteresis effect [52]. The radial basis function neural network is characterized by its simple structure, fast learning, and better approximation capabilities, which has been utilized widely in the fields of system modeling, identification, and nonlinear control. Hence, we employ the radial basis function neural network to provide on-line computation of the equivalent control input for the xy -piezoelectric scanner.

First, by incorporating the reference model in Eq. (5.33) as an internal model into the closed-loop system, the relationship between the tracking error vector E_{pz} and the internal model state vector h_{pz} can be obtained as below:

$$E_{pz} = \ddot{h}_{pz} + K_{pzt} h_{pz} \quad (5.34)$$

According to Eq. (5.34), the tracking error induced by the forced response of the reference trajectory with the form of Eq. (5.33) would be zero. Therefore, the remaining problem is to design a controller for stabilization of the closed-loop system with the internal model such that the tracking error induced by the natural response would decay to zero.



Here, we define the tracking error vector without reference trajectory as:

$$E_{pz} = 0 - X_{pz} = [x_{pz} \quad y_{pz}]^T \quad (5.35)$$

Substituting Eq. (3.8) into Eq. (5.35), we can obtain the error dynamics as below:

$$\ddot{E}_{pz} = -\ddot{X}_{pz} = -K_{pz}X_{pz} - B_{pz}\dot{X}_{pz} - C_{pz}U_{pz} + R_{pz} - D_{pz} \quad (5.36)$$

which implies that the plant is considered as a MIMO system. To simplify the

representation, define $f = -K_{pz}X_{pz} - B_{pz}\dot{X}_{pz} + R_{pz}$ to be an unknown time-varying

function of the system states, so that Eq. (5.36) can be simplified as:

$$\ddot{E}_{pz} = f - C_{pz}U_{pz} - D_{pz} \quad (5.37)$$

Note that $C_{pz} = \text{diag} \left[\frac{C_{pzx}}{m_{pz}}, \frac{C_{pzy}}{m_{pz}} \right] = \text{diag}[c_{pz1} \quad c_{pz2}]$ is a positive diagonal matrix

since the piezoelectric coefficients and equivalent mass of the piezoelectric scanner are

all positive values. Substituting Eq. (5.37) into Eq. (5.34), we can obtain the internal

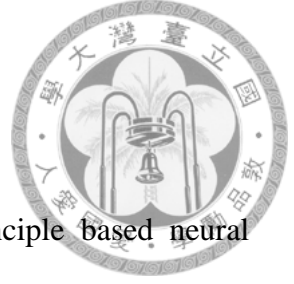
model state dynamics as shown below:

$$h_{pz}^{(4)} = f - C_{pz}U_{pz} - D_{pz} - K_{pzt}\dot{h}_{pz} \quad (5.38)$$

The main objective in the following controller design procedure is seeking a proper

control input vector U_{pz} such that the closed-loop system with the internal model is

exponentially stable.



5.3.2 Control algorithm

The schematic diagram of the proposed internal model principle based neural network complementary sliding mode control for cosine waveform tracking of the xy -piezoelectric scanner is shown in Fig. 5-2.

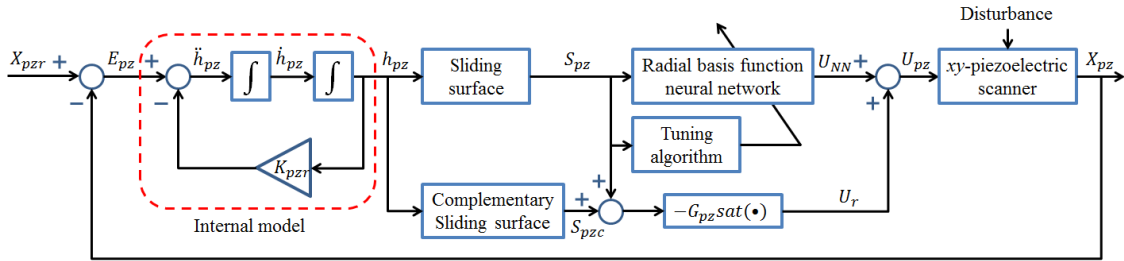


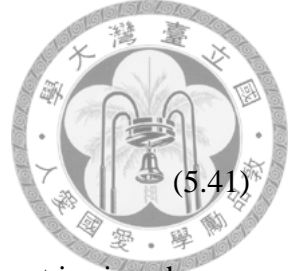
Fig. 5-2 The schematic diagram of internal model principle based neural network complementary sliding mode control

First, in order to develop the complementary sliding mode control, we define the generalized sliding surface S_{pz} and the complementary sliding surface S_{pzc} as the following form:

$$\begin{aligned}
 S_{pz} &= \ddot{h}_{pz} + 4\Lambda_{pz}\dot{h}_{pz} + 6\Lambda_{pz}^2 h_{pz} + 4\Lambda_{pz}^3 h_{pz} + \Lambda_{pz}^4 H_{pz} \\
 &= [S_{pz1} \quad S_{pz2}]^T
 \end{aligned}
 \tag{5.39}$$

$$\begin{aligned}
 S_{pzc} &= \ddot{h}_{pz} + 2\Lambda_{pz}\dot{h}_{pz} - 2\Lambda_{pz}^3 h_{pz} - \Lambda_{pz}^4 H_{pz} \\
 &= [S_{pzc1} \quad S_{pzc2}]^T
 \end{aligned}
 \tag{5.40}$$

where $\Lambda_{pz} = \text{diag}[\lambda_{pz1} \quad \lambda_{pz2}]$ is a positive diagonal matrix to be designed and $H_{pz}(t) = \int_0^t h_{pz}(\tau)d\tau$. And the relationship between S_{pz} and S_{pzc} is shown in the



following expression:

$$\dot{S}_{pzc} + \Lambda_{pz}(S_{pz} + S_{pzc}) = \dot{S}_{pz} \quad (5.41)$$

If all signals in Eq. (5.38) were known, a perfect equivalent control input is given by:

$$\begin{aligned} U_{eq} &= C_{pz}^{-1}(-h_{pz}^{(4)} + f - D_{pz} - K_{pzc}\ddot{h}_{pz} - \dot{S}_{pz} - \Lambda_{pz}S_{pz}) \\ &= [u_{eq1} \quad u_{eq2}]^T \end{aligned} \quad (5.42)$$

Substituting Eq. (5.42) into Eq. (5.38), we can find that:

$$\dot{S}_{pz} + \Lambda_{pz}S_{pz} = 0 \quad (5.43)$$

Since Λ_{pz} is a positive diagonal matrix, the sliding surface S_{pz} will converge to zero exponentially and the internal model state will converge to zero as well. However, we cannot obtain the signals of restoring force and scanning disturbance to obtain the equivalent control input in practice. Thus, we utilize the radial basis function neural network to approximate the equivalent control input U_{eq} by mapping the sliding variable S_{pz} into U_{eq} instead of model-based computation.

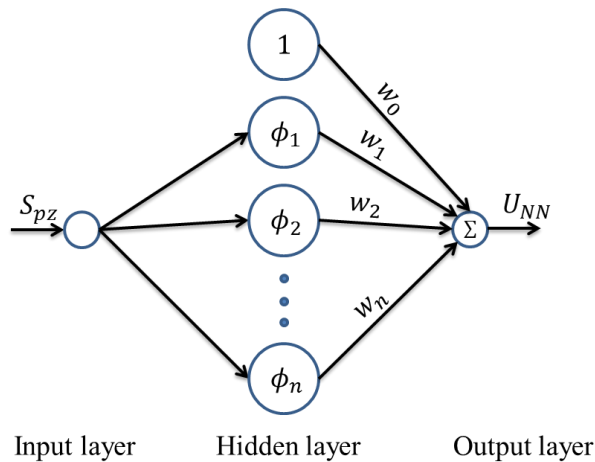
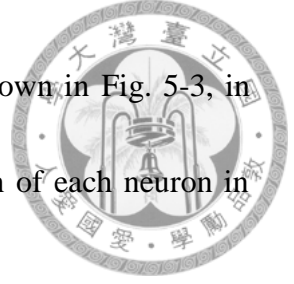


Fig. 5-3 Structure of the radial basis function neural network



The structure of the radial basis function neural network is shown in Fig. 5-3, in which the Gaussian function is employed as the activation function of each neuron in the hidden layer.

$$\phi_i = \exp\left(-\frac{\|S_{pz} - P_i\|_2^2}{\sigma_i^2}\right), \quad i = 0, 1, 2, \dots, n \quad (5.44)$$

where σ_i and $P_i = [p_{ix} \ p_{iy}]^T$ are the spread factor and central position of the i -th neuron, respectively. Here, P_0 is equal to S_{pz} so that $\phi_0 = 1$. The weighting factor $w_i = [w_{ix} \ w_{iy}]^T$ between hidden and output layer will be adjusted by the designed tuning algorithm. Thus, the output of the neural network U_{NN} can be expressed as below:

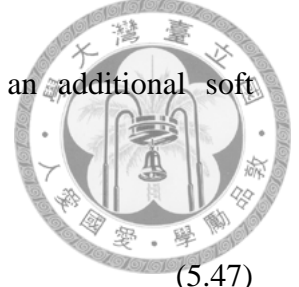
$$U_{NN} = \sum_{i=0}^n w_i \phi_i = W \Phi^T = [u_{NN1} \ u_{NN2}]^T \quad (5.45)$$

where $W = [w_0 \ w_1 \ \dots \ w_n] \in R^{2 \times n}$, $\Phi = [\phi_0 \ \phi_1 \ \dots \ \phi_n] \in R^{1 \times n}$.

Theoretically, the radial basis function neural network can approximate any nonlinear function with a reasonable accuracy and a basic assumption can be made for the stability analysis [53]: There exists an optimal weighting factor W^* such that the output U_{NN}^* approximate the equivalent control U_{eq} with an error smaller than δ .

$$\|U_{eq} - U_{NN}^*\|_{\infty} \leq \delta \quad (5.46)$$

where $U_{NN}^* = W^* \Phi^T$. Let $\tilde{W} = W - W^*$ so that $U_{NN} - U_{NN}^* = \tilde{W} \Phi^T$.



Moreover, in order to improve the robustness, we apply an additional soft switching input U_r which is given by:

$$U_r = -G_{pz} \text{sat}(S_{pz} + S_{pzc}) \quad (5.47)$$

where $G_{pz} = \text{diag}[g_{pz1} \ g_{pz2}]$ is a positive diagonal matrix and satisfies $g_{pz1}, g_{pz2} > \delta$. The saturation function $\text{sat}(S_{pz} + S_{pzc})$ is defined as following form:

$$\text{sat}(S_{pz} + S_{pzc}) \equiv [\text{sat}(s_{pz1} + s_{pzc1}) \ \text{sat}(s_{pz2} + s_{pzc2})]^T \quad (5.48)$$

where $\text{sat}(s_{pzi} + s_{pzci}) = \begin{cases} 1 & s_{pzi} + s_{pzci} > \varepsilon_{pz} \\ \frac{s_{pzi} + s_{pzci}}{\varepsilon_{pz}} & \text{if } -\varepsilon_{pz} \leq s_{pzi} + s_{pzci} \leq \varepsilon_{pz} \\ -1 & s_{pzi} + s_{pzci} < -\varepsilon_{pz} \end{cases}$ and ε_{pz} is a

small positive parameter adjusting the rate of switching operation. Hence, the overall control input is expressed as:

$$U_{pz} = U_{NN} + U_r = W\Phi^T - G_{pz} \text{sat}(S_{pz} + S_{pzc}) \quad (5.49)$$

5.3.3 Stability analysis

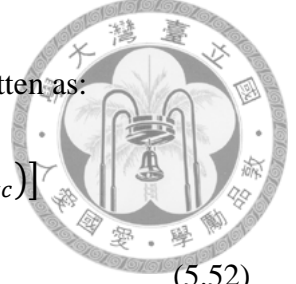
Define a Lyapunov function candidate V_{pz} , which is a positive definite function:

$$V_{pz} = \frac{1}{2} S_{pz}^T S_{pz} + \frac{1}{2} S_{pzc}^T S_{pzc} + \frac{1}{2} \text{tr}(\tilde{W}^T C_{pz}^T \Gamma^{-1} \tilde{W}) \quad (5.50)$$

where $\Gamma = \text{diag}[\gamma_1, \gamma_2]$ is a positive diagonal matrix, $\text{tr}(\cdot)$ is the trace of a matrix.

Taking the time derivative of the Lyapunov candidate function, we obtain:

$$\dot{V}_{pz} = S_{pz}^T \dot{S}_{pz} + S_{pzc}^T \dot{S}_{pzc} + \text{tr}(\tilde{W}^T C_{pz}^T \Gamma^{-1} \dot{\tilde{W}}) \quad (5.51)$$



According to Eq. (5.41), the first two term of Eq. (5.51) can be rewritten as:

$$\begin{aligned}
S_{pz}^T \dot{S}_{pz} + S_{pzc}^T \dot{S}_{pzc} &= S_{pz}^T \dot{S}_{pz} + S_{pzc}^T [\dot{S}_{pz} - \Lambda_{pz}(S_{pz} + S_{pzc})] \\
&= (S_{pz} + S_{pzc})^T (\dot{S}_{pz} - \Lambda_{pz} S_{pzc}) \\
&= -(S_{pz} + S_{pzc})^T \Lambda_{pz} (S_{pz} + S_{pzc}) + (S_{pz} + S_{pzc})^T (\dot{S}_{pz} + \Lambda_{pz} S_{pz})
\end{aligned} \tag{5.52}$$

Here, $\dot{S}_{pz} + \Lambda_{pz} S_{pz}$ can be reformulated by Eq. (5.42), Eq. (5.38) and Eq. (5.49) as following:

$$\begin{aligned}
\dot{S}_{pz} + \Lambda_{pz} S_{pz} &= -C_{pz} U_{eq} - h_{pz}^{(4)} + f - D_{pz} - K_{pzc} \ddot{h}_{pz} \\
&= -C_{pz} U_{eq} + C_{pz} U_{pz} \\
&= C_{pz} (U_{NN} + U_r - U_{eq}) \\
&= C_{pz} [(U_{NN} - U_{NN}^*) + U_r - (U_{eq} - U_{NN}^*)] \\
&= C_{pz} [\tilde{W} \Phi^T + U_r - (U_{eq} - U_{NN}^*)]
\end{aligned} \tag{5.53}$$

Substituting Eq. (5.52) and Eq. (5.53) into Eq. (5.51) we can obtain:

$$\begin{aligned}
\dot{V}_{pz} &= -(S_{pz} + S_{pzc})^T \Lambda_{pz} (S_{pz} + S_{pzc}) + (S_{pz} + S_{pzc})^T C_{pz} \tilde{W} \Phi^T \\
&\quad + (S_{pz} + S_{pzc})^T C_{pz} [U_r - (U_{eq} - U_{NN}^*)] \\
&\quad + tr(\tilde{W}^T C_{pz}^T \Gamma^{-1} \dot{\tilde{W}})
\end{aligned} \tag{5.54}$$

By applying the following trace operations:

$$a. tr(AB) = tr(BA), \quad \text{for any } A, B \in R^{n \times n}$$

$$b. tr(A + B) = tr(B + A), \quad \text{for any } A, B \in R^{n \times n}$$

$$c. \text{tr}(AB^T) = \text{tr}(BA^T) = A^T B = B^T A, \quad \text{for any } A, B \in \mathbb{R}^{n \times 1}$$



We can rewrite Eq. (5.54) in the following expression:

$$\begin{aligned} \dot{V}_{pz} = & -(S_{pz} + S_{pzc})^T \Lambda_{pz} (S_{pz} + S_{pzc}) \\ & + (S_{pz} + S_{pzc})^T C_{pz} [U_r - (U_{eq} - U_{NN}^*)] \\ & + \text{tr} \left[\tilde{W}^T C_{pz}^T \left((S_{pz} + S_{pzc}) \Phi + \Gamma^{-1} \dot{\tilde{W}} \right) \right] \end{aligned} \quad (5.55)$$

In order to cancel the last term in Eq. (5.55), we choose the tuning algorithm as:

$$\dot{W} = \dot{\tilde{W}} = -\Gamma (S_{pz} + S_{pzc}) \Phi \quad (5.56)$$

By Eq. (5.46), we can simplify Eq. (5.55) as below:

$$\begin{aligned} \dot{V}_{pz} \leq & -\sum_{i=1}^2 \lambda_{pzi} (s_{pzi} + s_{pzci})^2 \\ & - \sum_{i=1}^2 (s_{pzi} + s_{pzci}) c_{pzi} [g_{pzi} \text{sat}(s_{pzi} + s_{pzci}) - \delta] \end{aligned} \quad (5.57)$$

Because the saturation function is used in the control scheme, the analysis of parameters $s_{pzi} + s_{pzci}$ inside or outside the boundary layer ε_{pz} should be taken into account. First, consider the complementary sliding variables which are outside the boundary layer, i.e., $|s_{pzi} + s_{pzci}| > \varepsilon_{pz}$, so that the saturation function can be replaced by the sign function. Thus, the time derivative of the Lyapunov function \dot{V}_{pz} becomes:

$$\begin{aligned} \dot{V}_{pz} \leq & -\sum_{i=1}^2 \lambda_{pzi} (s_{pzi} + s_{pzci})^2 \\ & - \sum_{i=1}^2 (s_{pzi} + s_{pzci}) c_{pzi} [g_{pzi} \text{sgn}(s_{pzi} + s_{pzci}) - \delta] \\ \leq & -\sum_{i=1}^2 \lambda_{pzi} (s_{pzi} + s_{pzci})^2 \end{aligned} \quad (5.58)$$

$$\begin{aligned}
& - \sum_{i=1}^2 |s_{pzi} + s_{pzci}| c_{pzi} (g_{pzi} - \delta) \\
& < 0
\end{aligned}$$



Second, consider the complementary sliding variables which are inside the boundary layer, i.e. $|s_{pzi} + s_{pzci}| \leq \varepsilon_{pz}$, then, the saturation function will be replaced by $\frac{s_{pzi} + s_{pzci}}{\varepsilon_{pz}}$.

The time derivative of the Lyapunov function \dot{V}_{pz} becomes:

$$\begin{aligned}
\dot{V}_{pz} & \leq - \sum_{i=1}^2 \lambda_{pzi} (s_{pzi} + s_{pzci})^2 \\
& \quad - \sum_{i=1}^2 (s_{pzi} + s_{pzci}) c_{pzi} \left[g_{pzi} \left(\frac{s_{pzi} + s_{pzci}}{\varepsilon_{pz}} \right) - \delta \right] \\
& \leq - \sum_{i=1}^2 (s_{pzi} + s_{pzci})^2 \left[\lambda_{pzi} + \frac{c_{pzi} g_{pzi}}{\varepsilon_{pz}} - \frac{c_{pzi} \delta}{|s_{pzi} + s_{pzci}|} \right]
\end{aligned} \tag{5.59}$$

Thus, according to Lyapunov stability theorem, when

$$|s_{pzi} + s_{pzci}| > \frac{c_{pzi} \delta}{\lambda_{pzi} + c_{pzi} g_{pzi} / \varepsilon_{pz}}$$

then (5.60)

$$\dot{V}_{pz} < 0$$

which implies that $V_{pz}, \dot{V}_{pz} \in L_\infty$ and thus $S_{pz}, S_{pzc}, h_{pz}, \dot{h}_{pz}, \ddot{h}_{pz}, \ddot{h}_{pz}, \tilde{W} \in L_\infty$.

According to Eq. (5.60), it can be concluded that the internal model state will converge into a small error bound. Hence, the tracking error will also converge into to a small set according to internal model principle.



Chapter 6

Experiments



In this chapter, the experimental setup will be described at first. In order to validate the performance of the designed controllers, the experiments of hysteresis compensation and scan trajectory tracking at different scan frequencies are performed. And then the proposed hierarchical local scan based on Lissajous trajectory's methodology is employed to scan the human blood cells.

6.1 Experimental Setup

The photo of the overall implemented AFM system, including the measuring system and the scanning system, is shown in Fig. 6-1. In the measuring system, a commercial CD/DVD pickup head is fixed in the aluminum rectangle framework and the probe is mounted on the CD/DVD pickup head's lens below. The distance between the probe and the CD/DVD pickup head's lens is adjusted by a precision linear stage. In addition, the measured sample lies in the scanning system which is composed of the xy -hybrid scanner and the z -scanner. In the experiments, MATLAB xPC target is employed for real-time control. Besides, Agilent N1231b A/D card and MC1602/16 is for



laser interferometer and strain gauge sensing feedback, respectively. NI 6733 D/A card is for output control signals. Furthermore, the measured noises, including sensor noises and environmental disturbances, are shown in Fig. 6-2, and the measured noises of laser interferometer and strain gauge sensor are calculated to be 14.15 nm and 13.51 nm in rms error.

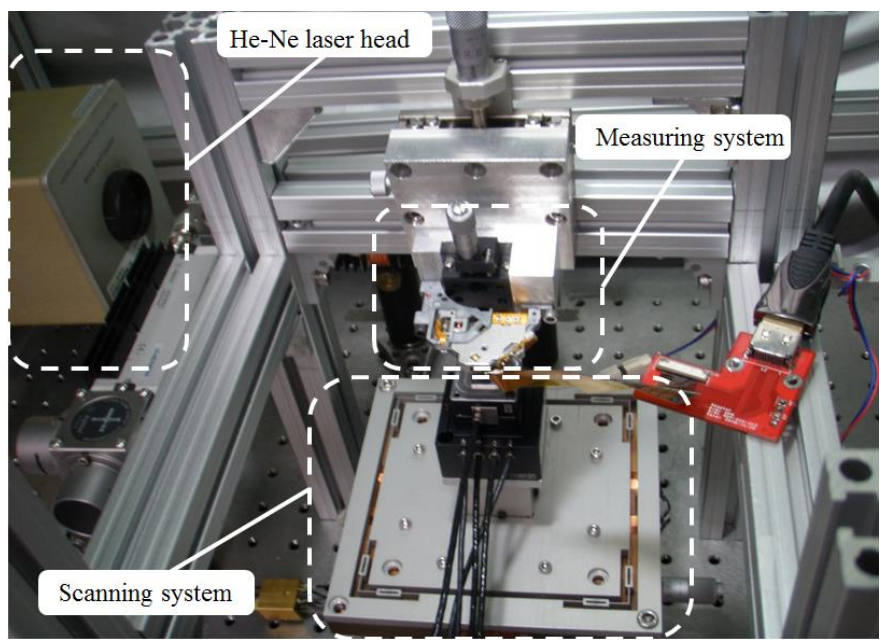


Fig. 6-1 Realization of the proposed AFM system

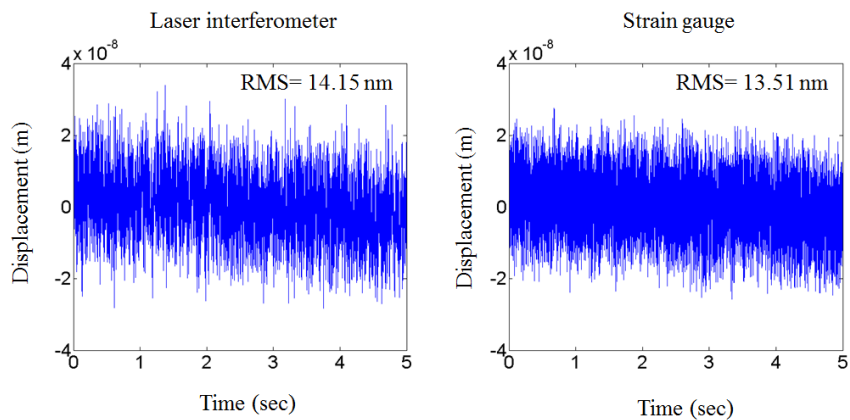


Fig. 6-2 The measured noises of laser interferometer and strain gauge sensor



6.2 Hysteresis Compensation

In this section, experiments of hysteresis compensation are performed to verify the performance of the proposed neural network complementary sliding mode control. Fig. 6-3 shows the hysteresis effect of xy -piezoelectric scanner in x -axis. For open loop tracking, the maximum displacement error is $h_{max} = 13.12\%$, which would affect the scanning precision significantly. When the proposed controller is employed, the maximum displacement error is decreased to $h_{max} = 0.87\%$.

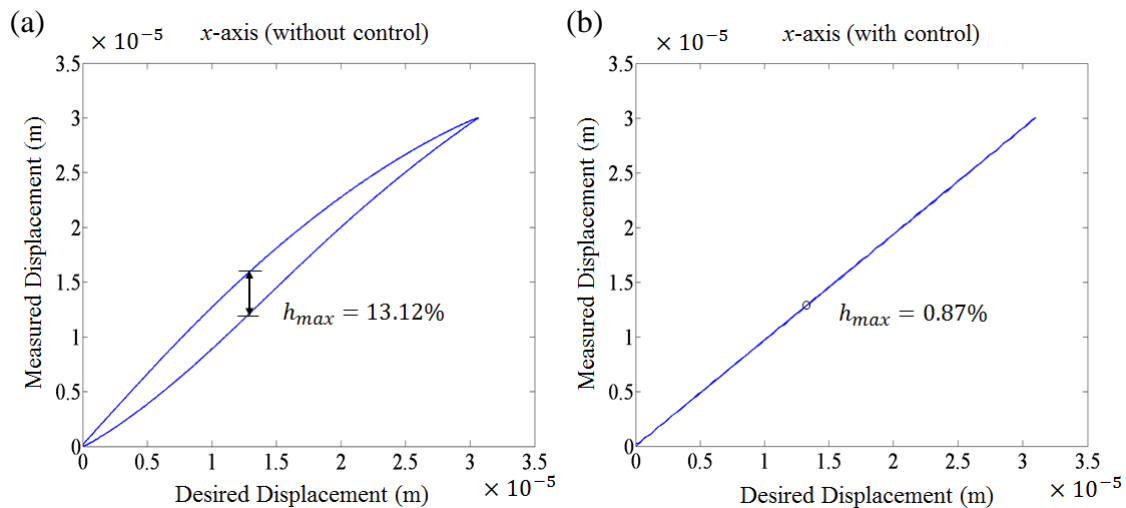


Fig. 6-3 The hysteresis effect of xy -piezoelectric scanner in x -axis (a) without control (b) with NNCSMC

Similarly, the hysteresis effect of xy -piezoelectric scanner in y -axis is shown in Fig. 6-4. The maximum displacement error without control is $h_{max} = 13.58\%$, which can be decreased to $h_{max} = 0.89\%$ when the proposed controller is applied. Therefore, the designed neural network complementary sliding mode controller can compensate the



hysteresis behavior effectively.

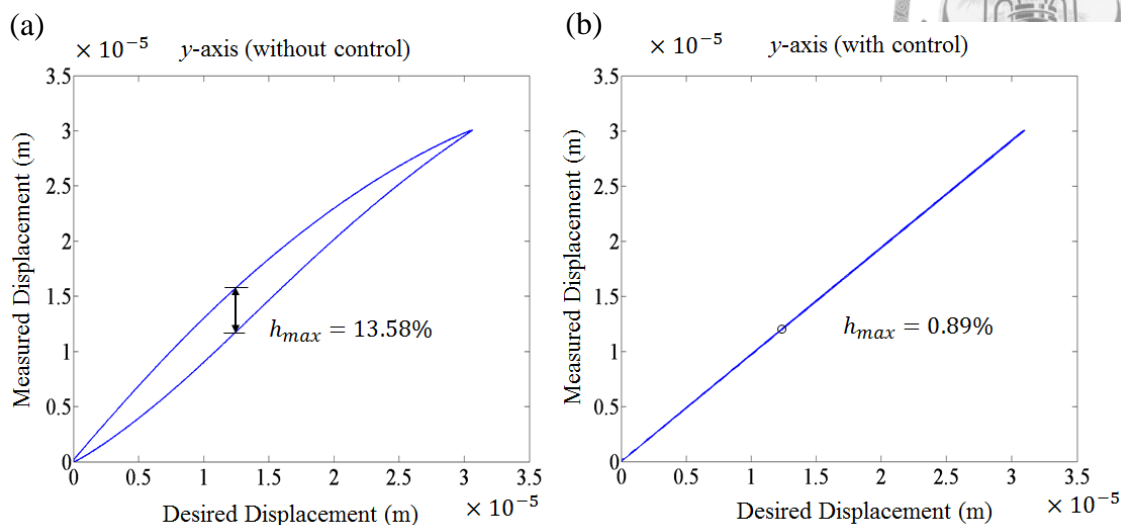



Fig. 6-4 The hysteresis effect of xy -piezoelectric scanner in y -axis (a) without control (b) with NNCSMC

6.3 Scan Trajectories Tracking

For the AFM system, the scan speed is mainly determined by the moving velocity of the scanner. In this section, three experiments of scan trajectory tracking including triangular waveform tracking with PI control, cosine waveform tracking with PI control, and cosine waveform tracking with the IMP based NNCSMC proposed in Section 5.3 are implemented to illustrate the improvement of the scan precision of the scan method and the proposed control scheme.

6.3.1 Triangular waveform with PI control

In conventional AFM system, the generally used scan trajectory and controller are



the raster pattern and PI controller, respectively. Here, the triangular waveforms with scan range of $\pm 5 \mu\text{m}$ and different frequencies are used for the x -axis motion of the piezoelectric scanner. As shown in Fig. 6-5, when the frequency of the triangular waveform is 10 Hz, which is about 1% of the scanner's bandwidth, the scanner can track the scan trajectory with acceptable tracking precision. However, the hysteresis effect of the piezoelectric scanner is obvious. As the frequency is increased to 50 Hz, the high frequency harmonic signals of the triangular waveform will start to have sufficiently large amplitude to excite the mechanical vibration of the scanner, where results will induce a large scan trajectory tracking error and distort the scanning image. When the frequency is further increased to 100 Hz, the aroused mechanical vibration will be even serious. From these experimental results, we can find that the conventional non-smooth scan trajectory would cause the scan frequency of AFM to be limited to just about 1 % of the scanner's bandwidth. Moreover, the generally used PI controller will have difficulty to handle the hysteresis problem of piezoelectric scanner.

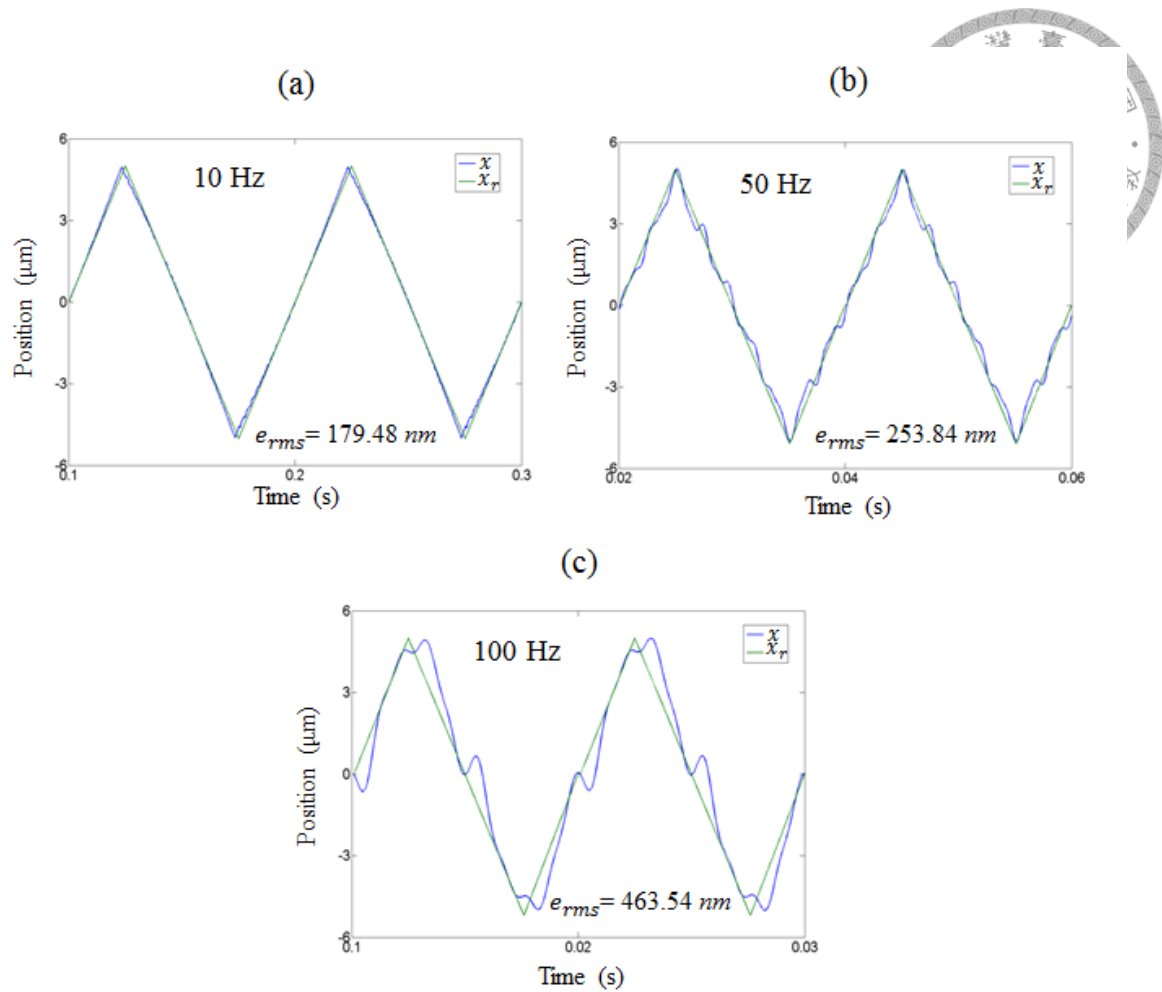


Fig. 6-5 Triangular waveform tracking performance with frequency of (a) 10 Hz, (b) 50 Hz, and (c) 100 Hz using PI control

6.3.2 Cosine waveform with PI control

In order to show the effect of scan trajectory on AFM scanning precision, we replace the triangular waveform with cosine waveform while the control scheme is still PI control. Thus, cosine waveforms with the same scan range of $\pm 5 \mu\text{m}$ and scan frequencies are applied to the x -axis motion of the piezoelectric scanner. As shown in Fig. 6-6, since the tracking trajectory contains only a single-frequency signal, there is no



aroused mechanical vibration during the scanning process. Furthermore, the scanning precision can be improved significantly by only changing the non-smooth scan trajectory to a smooth one. Hence, the scan speed of AFM can be easily increased in software aspect but at no price of modifying any hardware.

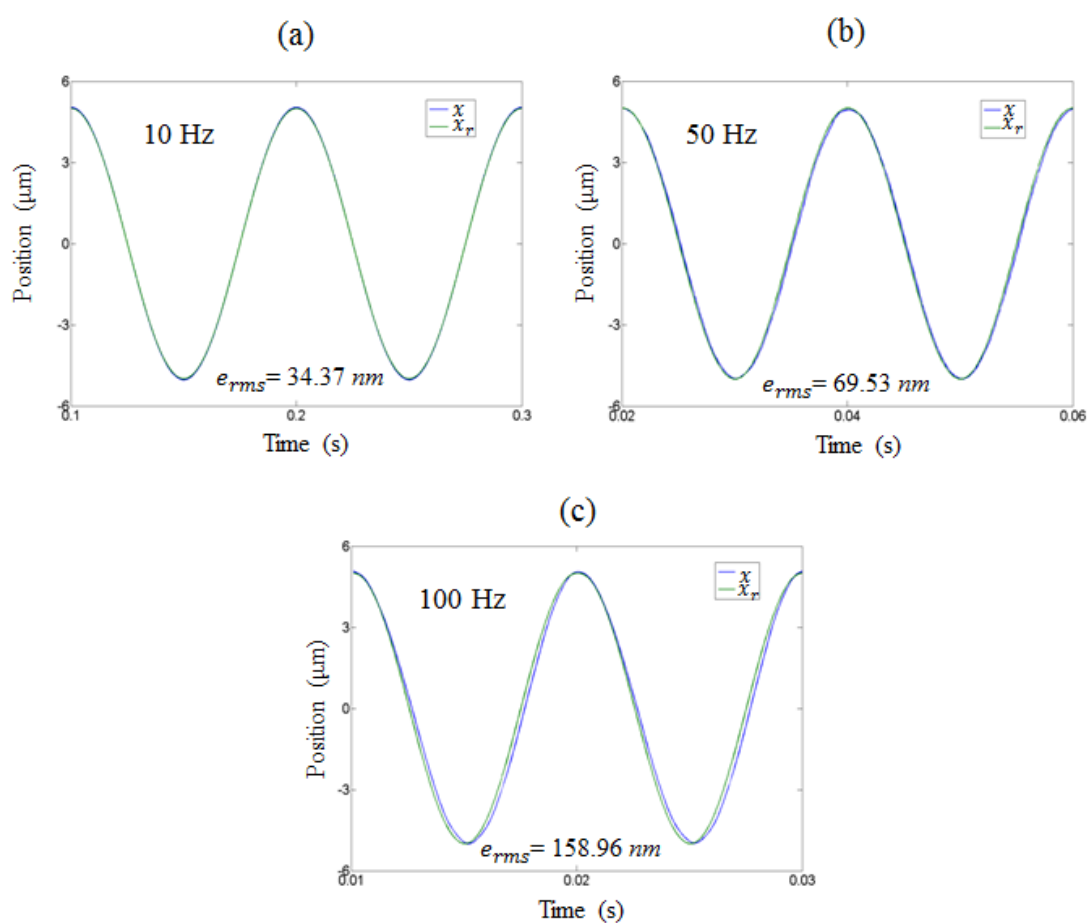


Fig. 6-6 Cosine waveform tracking performance with frequency of (a) 10 Hz, (b) 50 Hz, and (c) 100 Hz using PI control

6.3.3 Cosine waveform with IMP based NNCSMC

For the experiments in this section, the same cosine waveforms are employed to



the x -axis motion of the piezoelectric scanner with the designed IMP based NNCSMC proposed in Section 5-3. The tracking results are shown in Fig. 6-7, in there we can find that the tracking errors are reduced by the proposed control scheme significantly. In comparison with the triangular waveforms using PI control, the cosine waveform using the proposed controller permits one order increase in scan rate under the identical hardware conditions.

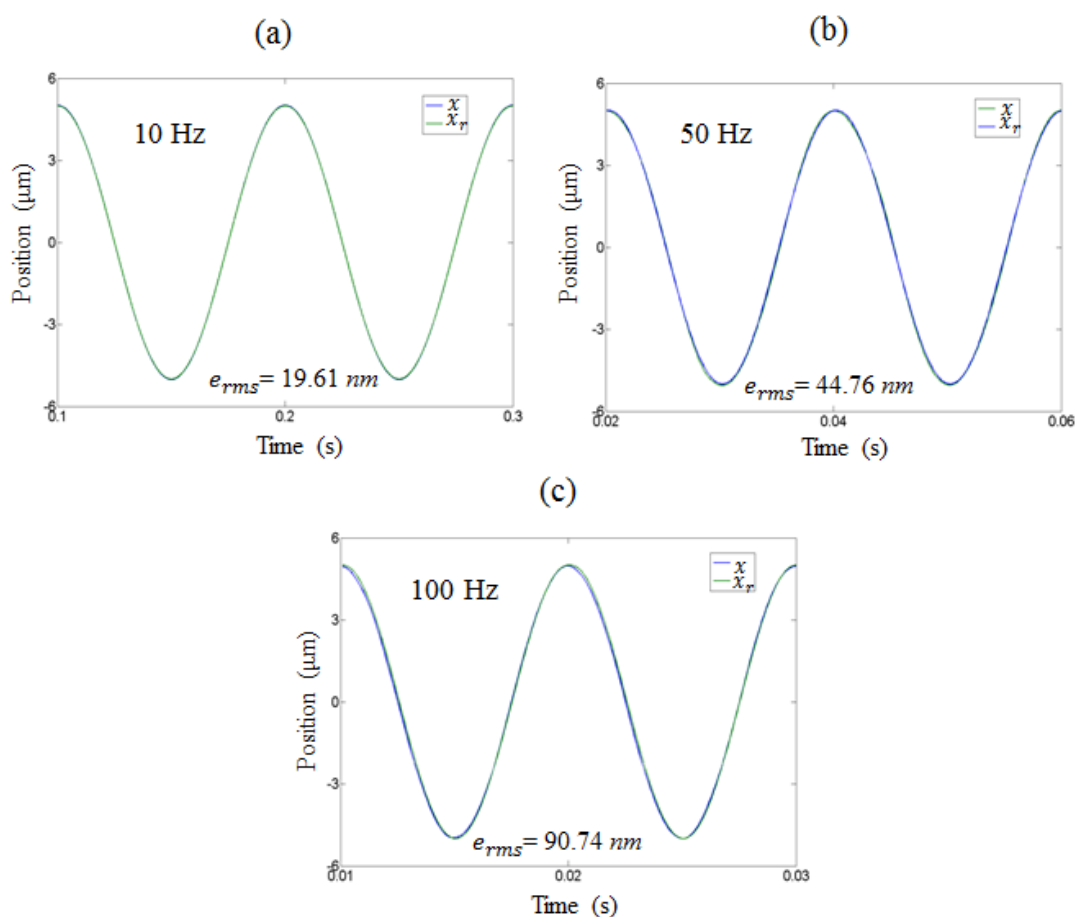


Fig. 6-7 Cosine waveform tracking performance with frequency of (a) 10 Hz, (b) 50 Hz, and (c) 100 Hz using IMP based NNCSMC

6.4 Numerical Simulation of Lissajous



Hierarchical Local Scan

In this section, the Matlab Simulink is used to simulate the performance of the proposed hierarchical local scan algorithm. We use Eqs. (3.16) and (3.17) as the plants of the xy -scanner and adopt our proposed ACSMC with the following parameters:

$$\Lambda_{em} = \text{diag}[5000 \quad 5000], \quad \varepsilon_{em} = \text{diag}[10^{-5} \quad 10^{-5}], \quad G_{em} = \text{diag}[0.1 \quad 0.1]$$

Besides, referring to sweep-sine identification experiment, the transfer function of the plant of the z -scanner is shown below:

$$G_z(s) = \frac{3.127 \times 10^{-5}s + 21.461}{s^2 + 9514.258s + 4.916 \times 10^9}$$

In order to show the hierarchical local scan performance, we design a hexagon shaped samples. The width of the sample is $30 \mu\text{m}$ and the length of the sample is also $30 \mu\text{m}$.

In the first layer scan simulation, the scan area is set as $100 \mu\text{m} \times 100 \mu\text{m}$, there are three samples for scanning, as shown in Fig. 6-8 (a). The structure of the scan sample is trapezium-shaped, the height of the trapezium is $3.2 \mu\text{m}$, the width of a trapezium is $2 \mu\text{m}$, and distance between two trapeziums is $4 \mu\text{m}$, as show in Fig. 6-8 (b). The purpose of this numerical simulation is to achieve the desired resolution $\Delta_d = 160 \text{ pixels} \times 160 \text{ pixels}$ in the scan area of $30 \mu\text{m} \times 30 \mu\text{m}$ by a permissible maximum scan frequency



$f_{threshold1} \leq 1\text{Hz}$, and minimum frequency difference $f_{threshold2} \geq 0.025\text{ Hz}$. Notice that $f_{threshold2}$ will affect the period of the second or higher layer scan. If $f_{threshold2} = 0.025\text{ Hz}$, the scan time of each area (Δ_t) is equal to 20 seconds, which can be obtained by Eq. (4.5). However, if $f_{threshold2} > 0.025\text{ Hz}$, one finds that the Δ_t will be less than 20 seconds.

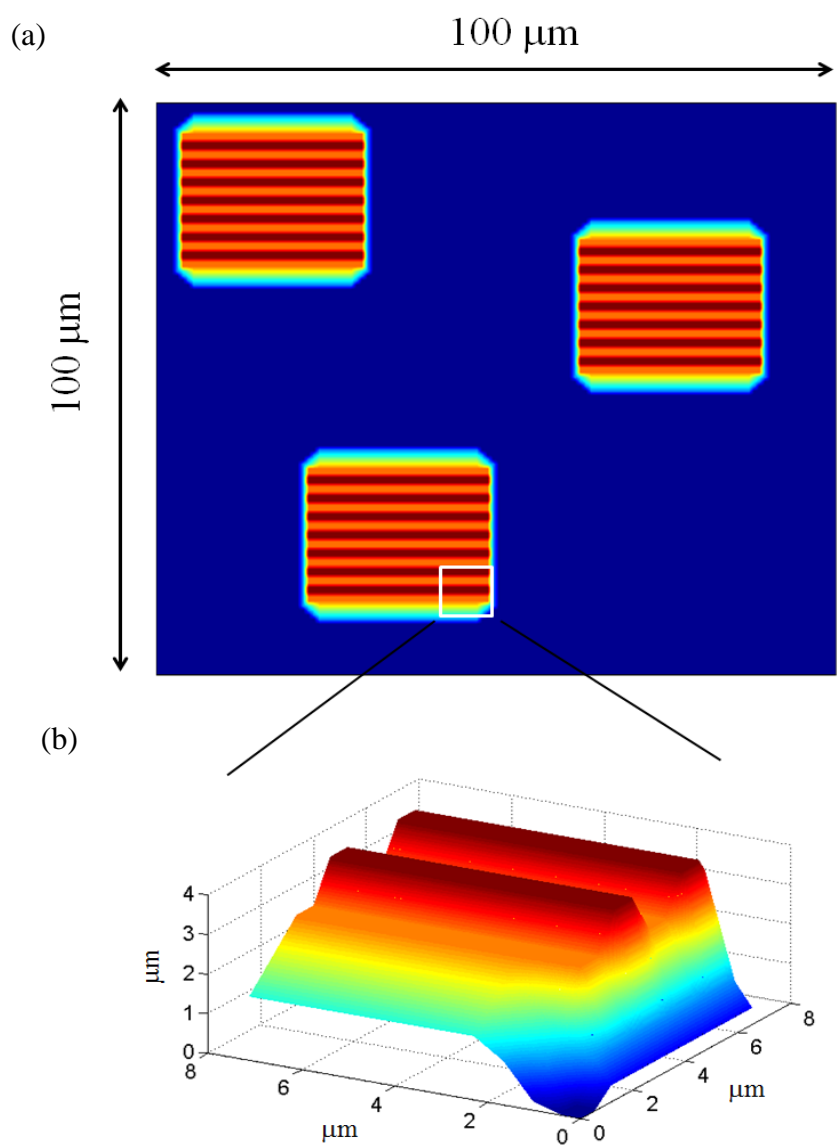


Fig. 6-8 The overall structure of the scan sample (a) 2D image (b) 3D image



First layer scan

In the first layer scan, in order to satisfy Eq. (4.11) with the minimum size of the interested sample ($\Delta_s = 30 \mu\text{m}$), the maximum scan frequency ($f_{threshold1} \leq 1\text{Hz}$), and the scan amplitudes ($A_{x1} = A_{y1} = 100 \mu\text{m}$). Therefore, the scan parameters of f_x and f_y are chosen as 1 Hz and 0.95 Hz, respectively, and the scan results can be found in Fig. 6-9, in this first layer scan which takes 10 seconds for scan time. Next, we want to remove the uninterested scan areas and determine the amplitudes of second layer scan (A_{x2}, A_{y2}).

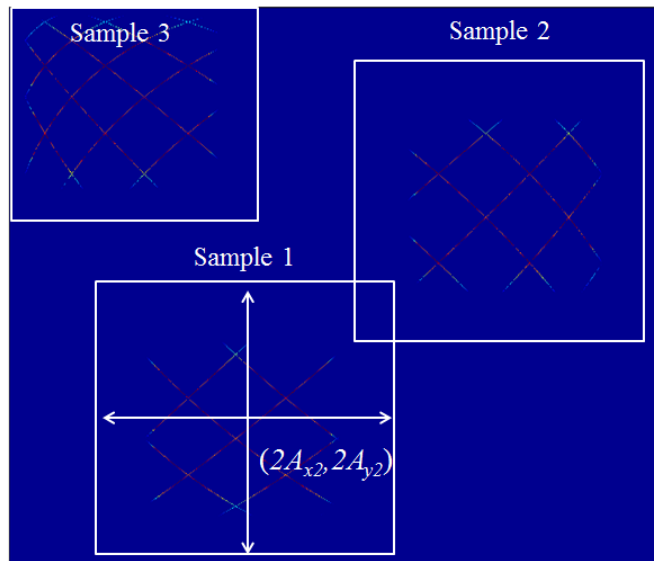


Fig. 6-9 The results of first layer scan

Second layer scan

In the second layer scan, there exists a sample nearest to the ending point of first layer scan and name it sample 1. In order to briefly display the performance of the



proposed scan algorithm, we just show the scan results for sample 1. Fig. 6-10 (a) show that sample 1 is divided into four scan areas by aforementioned region growing method.

Our mission is to satisfy the desired resolution (Δ_d) given the acceptable maximum scan frequency ($f_{threshold1} \leq 1\text{Hz}$) and the minimum frequency difference ($f_{threshold2} \geq 0.025\text{ Hz}$). Ideally, we will just choose the scan frequency $f_{x2}= 1\text{ Hz}$ and $f_{y2}= 0.9875\text{ Hz}$. However, the scan algorithm considering the constraint of $f_{threshold2}$, so that it regulates the scan frequency by $f_{x2}= 1\text{ Hz}$ and $f_{y2}= 0.975\text{ Hz}$, so that the result of Lissajous scan pattern are shown in Fig. 6-10 (a). The total scan time is 80 seconds and the image resolution is 120 pixels \times 80 pixels in this layer scan. Since the scan resolution cannot meet the Δ_d requirement, By comparing the 3D scan image (as shown in Fig. 6-10 (b)) with the original image (as shown in Fig. 6-8 (b)), it is obvious that second layer scan fails to have good image quality. This should be expected results

because the image resolution does not meet the preset value (Δ_d). Consequently, the hierarchical local scan algorithm will perform third layer scan.

Third layer scan

In the third layer scan, the sample will be divided into sixteen scan areas. For satisfying the Δ_d requirement given $f_{threshold1}$ and $f_{threshold2}$, the scan frequency can be met by choosing the $f_{x2}= 1\text{ Hz}$ and $f_{y2}= 0.975\text{ Hz}$, and the associated Lissajous



scan pattern is shown in Fig. 6-11 (a). The total scan time is 320 seconds and the image resolution is 480 pixels× 160 pixels in this layer scan. By comparing the second and third layer scan results, we find that the scan resolution will be enhanced 8 times when the scan time is increased 4 times. Fig. 6-11 (b) shows the 3D scan image of third layer scan, which exhibits obvious improvement in the image quality. Because the pre-specified Δ_d requirement has been satisfied, the Lissajous hierarchical local scan algorithm will not perform the next layer scan.

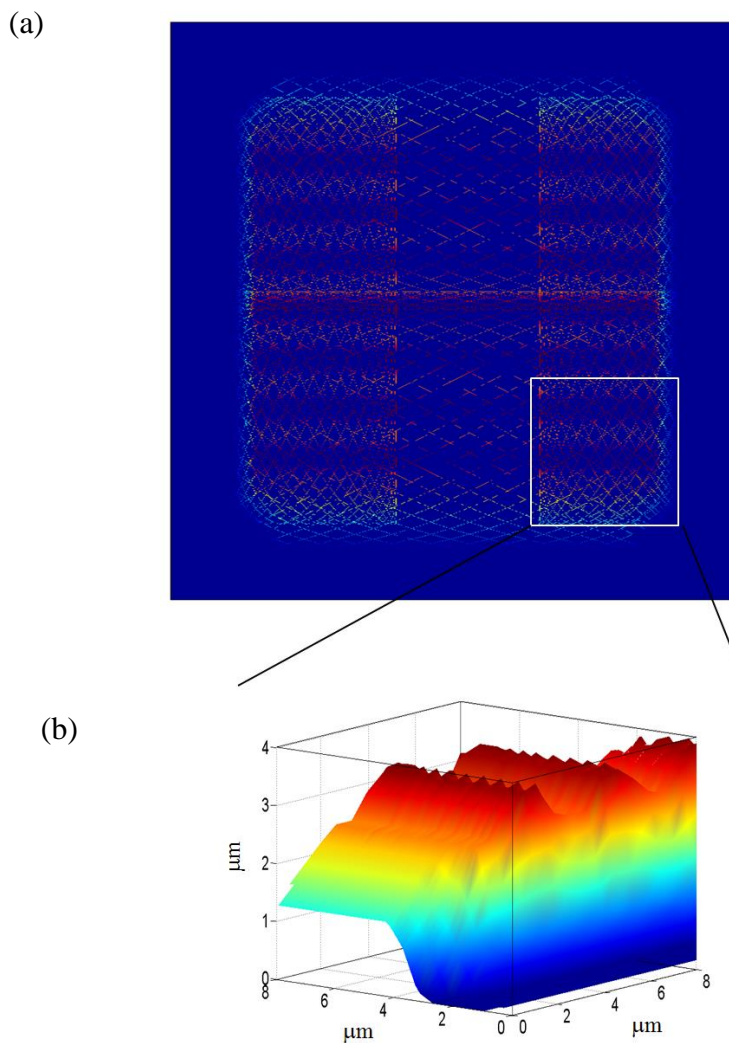


Fig. 6-10 The results of second layer scan (a) 2D Lissajous scan pattern (b) 3D image



To sum up from the simulation results by our proposed Lissajous hierarchical local scan algorithm, the uninterested scan areas can be removed by the first layer scan. In addition, for adding one more layer scan, the scan time will be increased 4 times, but the image resolution can be increased at least 4 times.

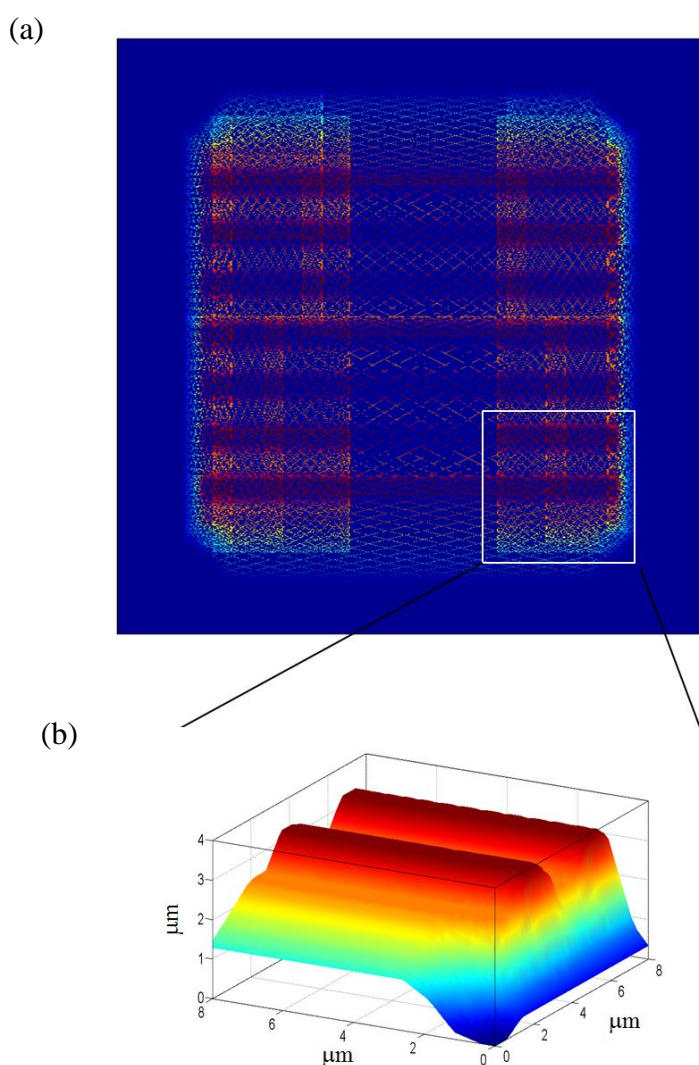


Fig. 6-11 The results of third layer scan (a) 2D Lissajous scan pattern (b) 3D image



6.5 AFM Scanning Application

For the experiments of AFM scanning, first, we will make a comparison of the imaging performance between raster scan and Lissajous scan by scanning a standard grating at different scan frequency. As shown in Fig. 6-12, the pitch and height of the standard grating are $10\ \mu\text{m}$ (peak : valley = 7 : 3) and the height of $1.5\ \mu\text{m}$, respectively. Then we apply the proposed Lissajous hierarchical local scan method to scanning of biological cells, and construct the unknown the 3D topography of each cell in an efficient way.

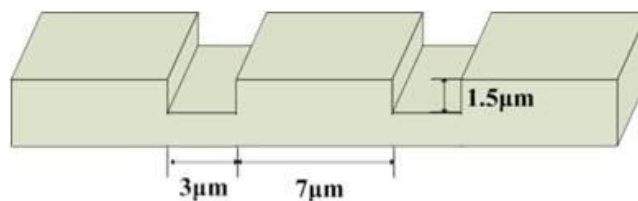


Fig. 6-12 The dimensions of standard grating

6.5.1 Standard grating with raster scan

In the first part of AFM scanning experiments, we scanned the standard grating with the most commonly used raster scan method and PI control at three different scan speeds. The scanned range is $30\ \mu\text{m} \times 25\ \mu\text{m}$ and the image resolution is 900×750 pixels. The scanned images are shown in Fig. 6-13, and the imaging distortions can be observed at average scan speeds of $900\ \mu\text{m/s}$ and $1500\ \mu\text{m/s}$ due to lack of appropriate



trajectory tracking at high speed scanning. Moreover, the behavior of scan probe will be affected by the severe scan oscillation at high scan frequencies, which also leads to incorrect height information.

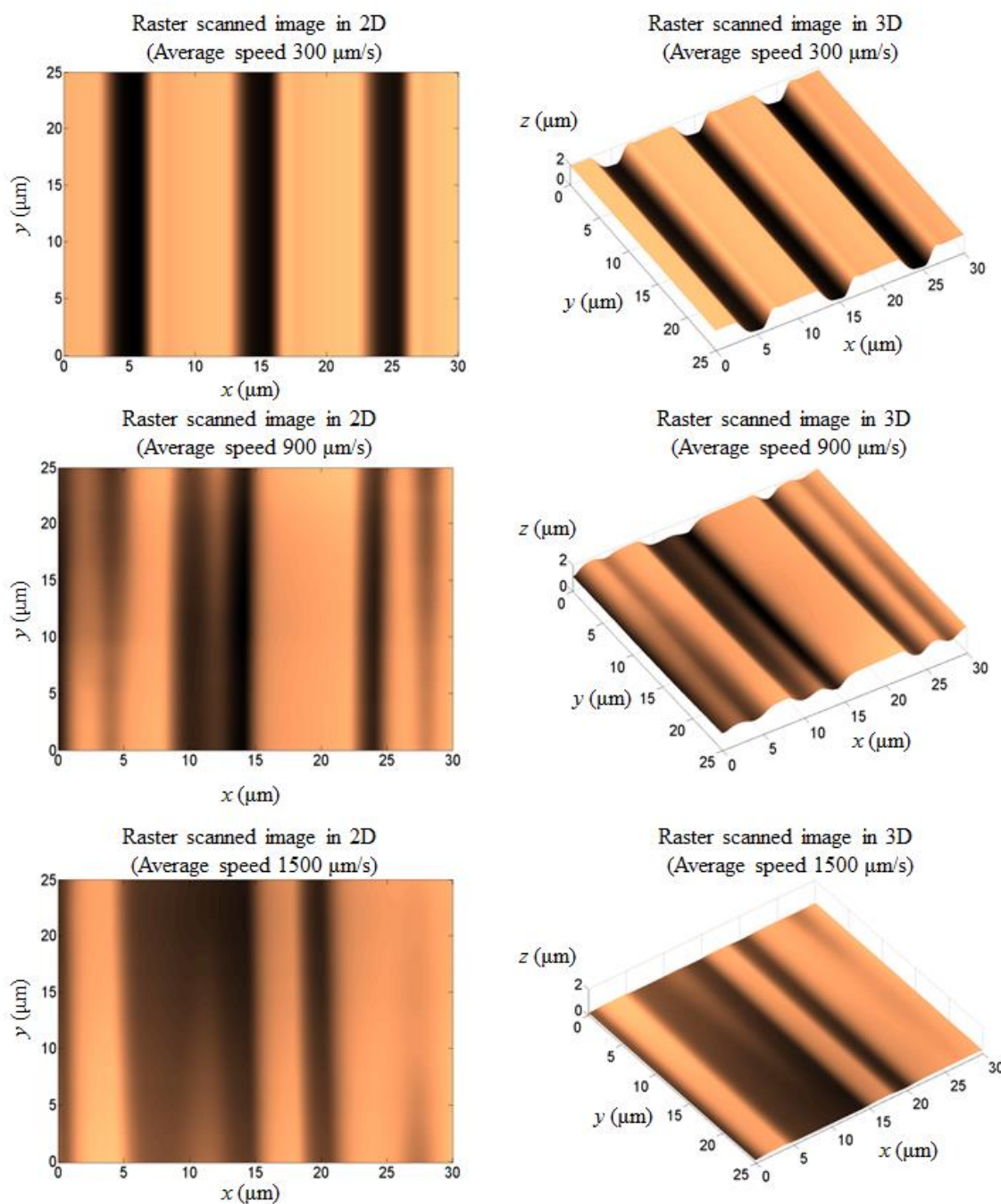


Fig. 6-13 Scanned images of standard grating with raster scan and PI control at different scan frequencies

6.5.2 Standard grating with Lissajous scan



Here, the same standard grating is scanned with the same hardware equipment using Lissajous scan method and the proposed IMP based NNCSMC. The scanned images are shown in Fig. 6-14, and we can find that by simply replacing the raster scan trajectory with a Lissajous one and applying the proposed controller, the scan-induced vibration can be avoided and high precision imaging of AFM can be achieved. As the scan average speed is increased from 300 $\mu\text{m/s}$ to 1500 $\mu\text{m/s}$, there is no severe oscillation occurred in the obtained image. However, it is obvious that the obtained height information of the sample tends to be distorted as the average scan speed is increased, which is due to the limited bandwidth of our z -scanner. Since the change rate of the sample surface topography will become rapid as the scan frequency is increased, the overall imaging performance at high scan speed is also determined by the response time of z -scanner. Nevertheless, the scan rate of AFM can still be increased by half-order with the proposed scan method compared with the conventional raster scan under the same hardware conditions.

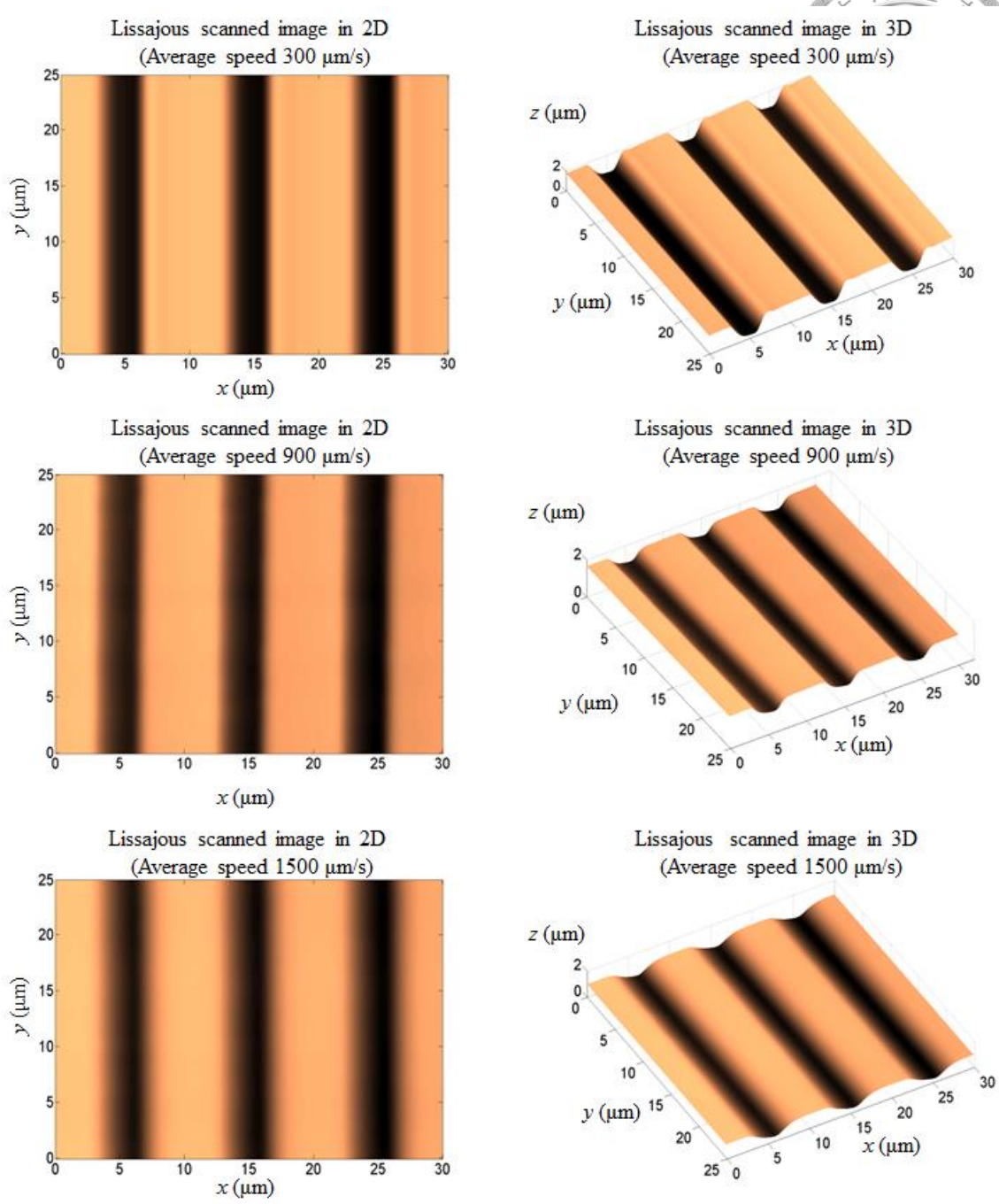


Fig. 6-14 Scanned images of standard grating with Lissajous scan and the proposed IMP based controllers at different scan frequencies

6.5.3 Human blood cells with Lissajous



hierarchical local scan

In this experiment, the human blood cells are scanned by the proposed Lissajous hierarchical local scan, which include the red and white blood cells, respectively. The red blood cell is disk-shaped and the size average from $6\ \mu\text{m}$ to $8\ \mu\text{m}$ in diameter. Different from red blood cells, the white blood cell is ellipse-shaped and has the larger size from $10\ \mu\text{m}$ to $16\ \mu\text{m}$. Besides, since the white blood cell has the nucleus, its cell's height is higher than that of red blood cell. Here, we apply the proposed scan methodology to scan the samples with the desired resolution ($\Delta_d = 2250\ \text{pixels} \times 2250\ \text{pixels}$) in a large scan range of $90\ \mu\text{m} \times 90\ \mu\text{m}$. Since the scan range greater than $32\ \mu\text{m} \times 32\ \mu\text{m}$, thus we use the electromagnetic stage for the first layer scan, and Fig. 6-15 (a) shows the scanned image result. In order to satisfy the minimum size requirement $\Delta_s = 6\ \mu\text{m}$ by Eq. (4.11) and provide the good scan performance of the electromagnetic scanner, the scan frequencies of first layer in f_{x1} and f_{y1} are 1.1 Hz and 1.09 Hz. The scan time of the image is about 50 seconds. By employing our proposed scan algorithm, the interested sample will be covered with the white rectangular frame, which is shown in Fig. 6-15 (b). After the first layer scan, we can



remove the most of uninterested scan area, which is 92.46 % of the total area (the outsides of the white rectangular frames from Fig. 6-16) taking 50 second scan time if it is actually scanned.

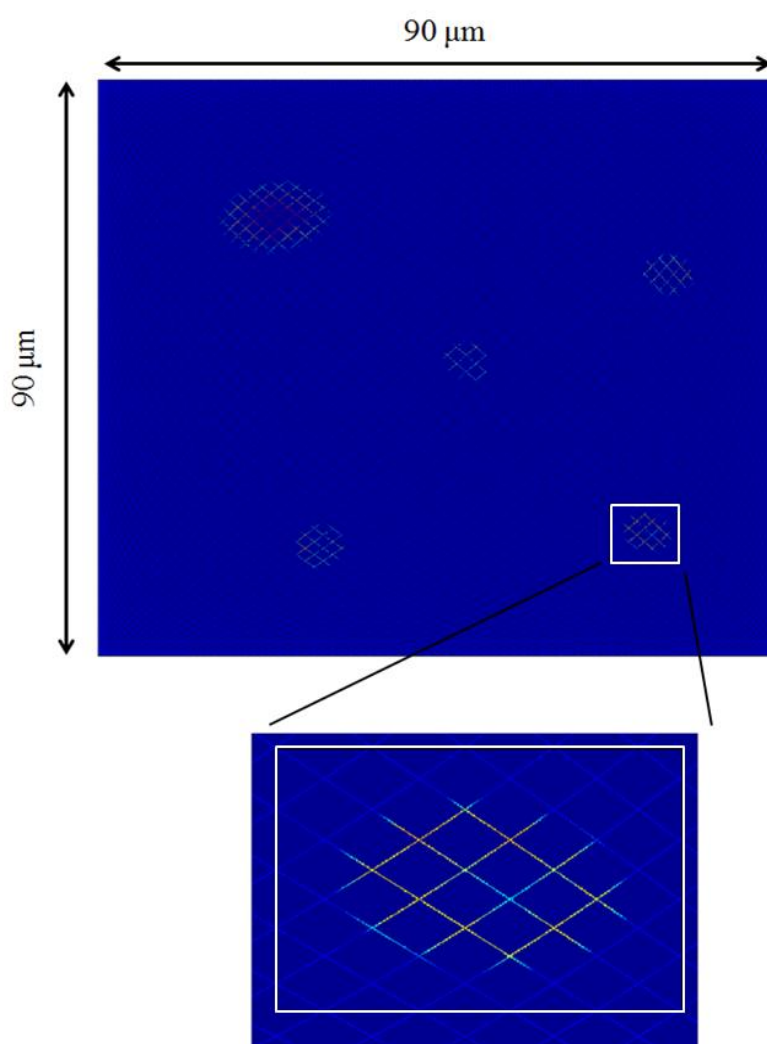


Fig. 6-15 (a) First layer scan result with a large scan range of $90\ \mu\text{m} \times 90\ \mu\text{m}$ (b) partial enlarged in the scan area

Fig. 6-16 shows the scan algorithm to calculate the height weighting (H_{sd}) of scan samples. In this case, we set the weighting threshold ($\Delta_{threshold}$) equal to 1.5 for



providing different scan strategy in each interested sample. In the sample 1, 2, 3, 5, they have approximate weightings and scan amplitudes (A_{x2}, A_{y2}), as shown in table of Fig. 6-16, which indicates that the samples probably belong to same category. Therefore, the algorithm will adopt the same scan strategy for them.

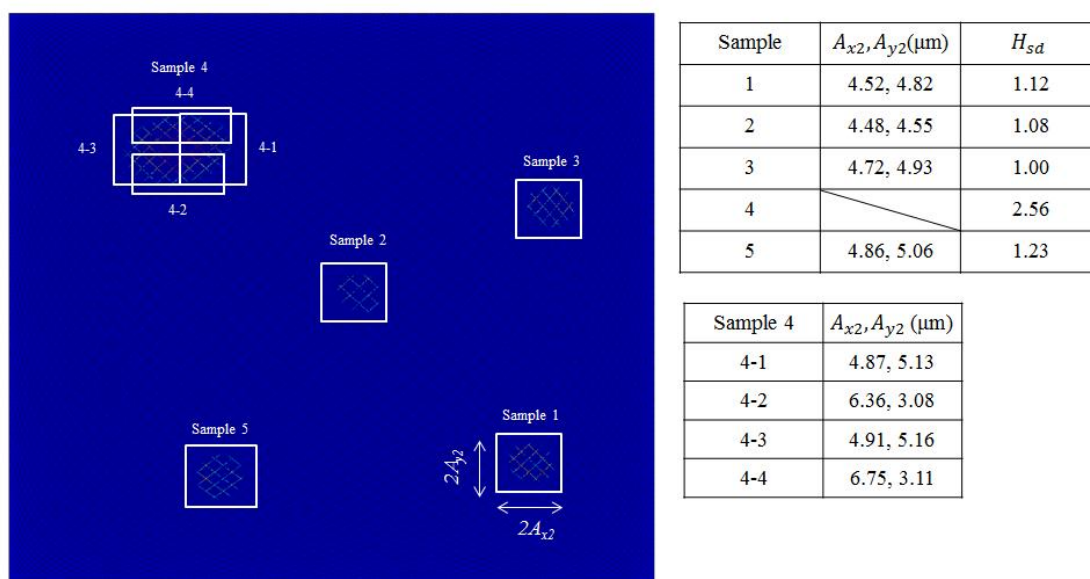


Fig. 6-16 Decide the rectangular scan area in the interested samples by weighting

Notice that, sample 4 displays a higher weighting (H_{sd}) and larger scan amplitude (is also shown in table of Fig. 6-16), and thus in order to obtain a good image quality for this sample, the proposed scan algorithm will further calculate the total weighting of the sample (W_{total}) by Eq. (4.22). By region growing method, the sample will be divided into four sub-blocks for providing next layer scan in order to gain higher image resolution. In second layer scan, since the sizes of all samples are less than $32 \mu\text{m}$, all samples will be scanned by the piezoelectric scanner.

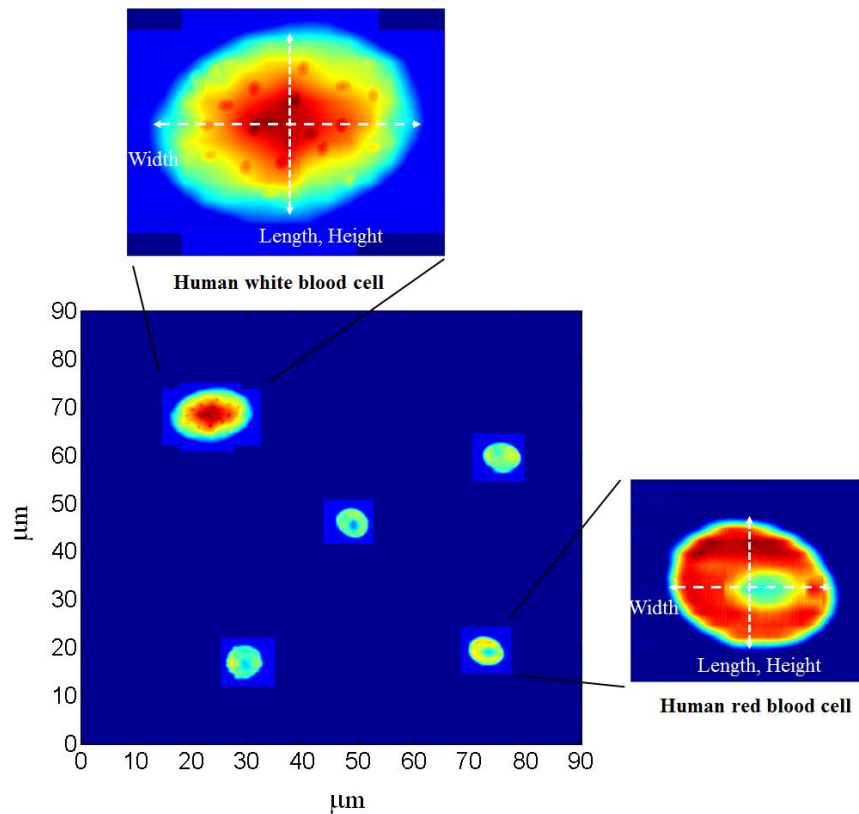


Fig. 6-17 AFM scanned image of human blood cells in 2D by the proposed Lissajous hierarchical local scan

The overall 2D scan results are shown in Fig. 6-17 by the scan frequency of $f_{x2} = 15$ Hz and $f_{y2} = 14.95$ Hz, and scan time for each rectangular frame scan time is 10 seconds. The resolution of the scanned image is 2250 pixels \times 2500 pixels, which has satisfied the demand of preset resolution. Therefore, the scan algorithm will not perform the third layer scan. Furthermore, by observing the imaging result and compare it against the topography of human blood cells, we can confirm that samples 1, 2, 3, 5 are indeed red blood cells whereas sample 4 is white blood cell. More specifically, we measure length, width, and height of the cell images in sample 1 and sample 4, and find



the data are $6.69\ \mu\text{m}$, $6.16\ \mu\text{m}$, and $2.35\ \mu\text{m}$, respectively, for sample 1 (as shown in Fig. 6-17), which are reasonably region to the physical size of a human red blood cell. In the sample 4, the length, width, and height are $13.75\ \mu\text{m}$, $10.23\ \mu\text{m}$ and $5.16\ \mu\text{m}$, respectively (as also shown in Fig. 6-17), which are also reasonably region to the physical size of a human white blood cell.

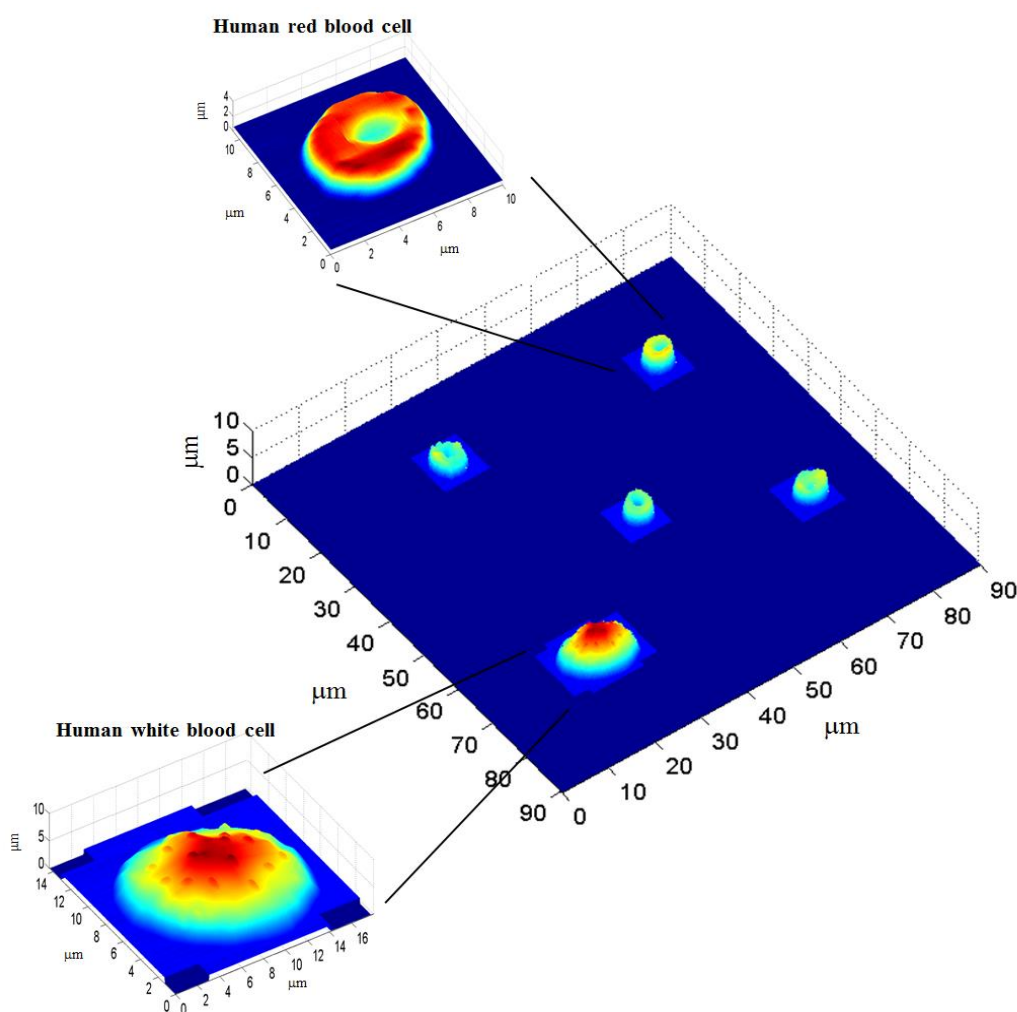


Fig. 6-18 AFM scanned image of human blood cells in 3D by the proposed Lissajous hierarchical local scan

Fig. 6-18 shows the AFM scanned image of human blood cells in 3D by the

proposed Lissajous hierarchical local scan. Generally speaking, the human red blood cell has the cave feature at the center and the human white blood cell has the structure of tentacles in the surface. From the scanned image of sample 1, which shown a cave at the center, we can further confirm that the sample is truly the human red blood cell (as shown in Fig. 6-18). Likewise, the sample 4 is truly a human white blood cell which has many similar tentacles in the surface (is also shown in Fig. 6-18). Such results can indeed verify that the proposed scan methodology in our self-designed AFM system has the ability to scan different biological cells with a large scan range, a superior scan rate, and without damage on the cells.



Chapter 7

Conclusions



In this research, we have developed the Lissajous hierarchical local scan method to improve AFM scan speed. Since the Lissajous scan trajectory contains only two single-frequency signals, the scan rate can be increased without inducing scanner vibration compared with the conventional raster scan method. Exploiting the well-known dynamics of the Lissajous trajectory, the internal model principle based control strategy is designed to achieve precision tracking of this scan pattern. In order to take advantage of both the high bandwidth of piezoelectric scanner and the large traveling range of electromagnetic scanner, the scan region is divided into 32 μm up and down for xy -hybrid scanner. For xy -electromagnetic scanner, the internal model principle based on adaptive complementary sliding mode controller is designed to track the scan trajectory precisely and to deal with the cross-coupling, system parameter uncertainties and external disturbance. For xy -piezoelectric scanner, the internal model principle based on neural network complementary sliding mode controller is designed to track the scan trajectory precisely and to deal with the cross-coupling, system parameter uncertainties, external disturbance and unknown nonlinear hysteresis effect. To verify

effectiveness of the proposed scan trajectory and control scheme, we provide some experiments to demonstrate the hysteresis compensation for piezoelectric scanner, scan trajectories tracking comparison between the proposed one and the conventional one.

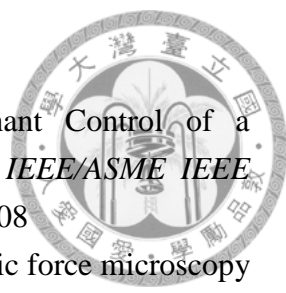


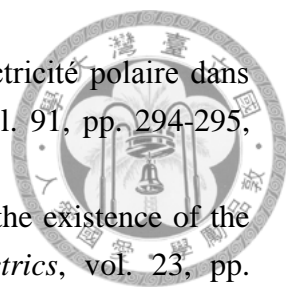
From the experimental results, the proposed Lissajous scan with the proposed control scheme can achieve superior imaging performance when comparison with results from raster scan is made, and thus the scan rate can be greatly increased. Furthermore, based on the characteristics of the Lissajous scan trajectory, we proposed a hierarchical local scan algorithm. By employing the sampled height information after the probe crosses the sample, we can appropriately remove the unnecessary scan areas, which saves significantly amount of scan time. On the other hand, by considering the varying condition of the interested sample topography, we design several layer scan which allows one to achieve the desired scan image resolution but only at the price of taking just enough local scans, which also helps to improve scan time. Finally, verification of the proposed scan methodology by numerical simulation and by actual biological scan applications has been performed, and our proposed solution is shown to be effectively for improving the scan rate in a larger scan region without any hardware modification.

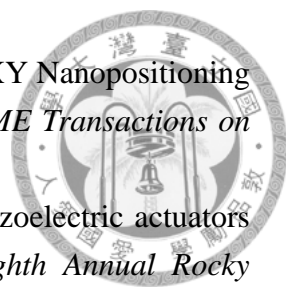
Reference

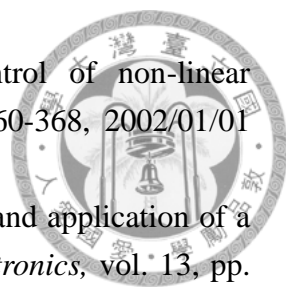


- [1] G. Binning, C. F. Quate, and C. Gerber, "Atomic force microscope," *Physical Review Letters*, vol. 56, pp. 930-933, 1986.
- [2] F. de Lange, A. Cambi, R. Huijbens, B. de Bakker, Wouter Rensen, Maria Garcia-Parajo, Niek van Hulst and Carl G. Figdor, "Cell biology beyond the diffraction limit: near-field scanning optical microscopy, " *Journal of Cell Science*, 114, 4153-4160, 2001.
- [3] H. Yamashita, A. Taoka, T. Uchihashi, T. Asano, T. Ando, and Y. Fukumori, "Single-Molecule Imaging on Living Bacterial Cell Surface by High-Speed AFM," *Journal of Molecular Biology*, vol. 422, pp. 300-309, 2012.
- [4] J. Rouhi, S. Mahmud, S. D. Hutagalung, and N. Naderi, "Field emission in lateral silicon diode fabricated by atomic force microscopy lithography," *Electronics Letters*, vol.48, pp.712 -714, 2012.
- [5] B. P. Lathi, *Linear Systems and Signals*, 2nd ed. London, U.K.: Oxford Univ. Press, 2004.
- [6] D. Croft, G. Shed, and S. Devasia, "Creep, Hysteresis, and Vibration Compensation for Piezoactuators: Atomic Force Microscopy Application," *Journal of Dynamic Systems Measurement and Control*, vol. 123, pp.35-43, 2001.
- [7] A. Sinno, P. Ruaux, L. Chassagne, S. Topcu, Y. Alayli, G. Lerondel, S. Blaize, A. Bruyant, and P. Royer, "Enlarged atomic force microscopy scanning scope: Novel sample-holder device with millimeter range," *Review of Scientific Instruments*, vol. 78, pp. 095107-7, 2007.
- [8] J. E. Brian, "Design of a large measurement-volume metrological atomic force microscope (AFM)," *Measurement Science and Technology*, vol. 20, p. 084003, 2009.
- [9] C. Werner, P. C. J. N. Rosielle, and M. Steinbuch, "Design of a long stroke translation stage for AFM," *International Journal of Machine Tools and Manufacture*, vol. 50, pp. 183-190, 2010.
- [10] Gaoliang Dai, Helmut Wolff, Frank Pohlenz, and Hans-Ulrich Danzebrink, "A metrological large range atomic force microscope with improved performance," *Review of Scientific Instruments*, 80, 043702, 2009.
- [11] Tong Guo, Longlong Wang, Jinping Chen, Xing Fu and Xiaotang Hu, "Development of a large-range atomic force microscope measuring system for optical free form surface characterization," *Measurement Science and Technology*,

- 
- 23, 115401, 2012.
- [12] B. Bhikkaji and S. O. Reza Moheimani, Integral Resonant Control of a Piezoelectric Tube Actuator for Fast Nanoscale Positioning, *IEEE/ASME IEEE Transactions on Mechatronics*, VOL. 13, NO. 5, OCTOBER 2008
- [13] Yuen K. Yong, Bilal Ahmed, and S. O. Reza Moheimani, Atomic force microscopy with a 12-electrode piezoelectric tube scanner, *Review of Scientific Instruments* 81, 033701, 2010.
- [14] Takeshi Fukuma, Yasutaka Okazaki, Noriyuki Kodera, Takayuki Uchihashi, and Toshio Ando, High resonance frequency force microscope scanner using inertia balance support, *Applied Physics Letters*, 92, 243119, 2008.
- [15] Brian J. Kenton and Kam K. Leang, Design and Control of a Three-Axis Serial-Kinematic High-Bandwidth Nanopositioner, *IEEE/ASME IEEE Transactions on Mechatronics*, VOL. 17, NO. 2, 2012.
- [16] Y.K. Yong, S.O.R. Moheimani, and I.R. Petersen, " High-speed cycloid-scan atomic force microscopy," *Nanotechnology*, vol. 21, 365503, 2010.
- [17] Shao-Kang Hung, "Spiral Scanning Method for Atomic Force Microscopy," *Journal of Nanoscience and Nanotechnology*, vol.10, no.7, pp.4511-4516, 2010.
- [18] T. Tuma, J. Lygeros, V. Kartik, A. Sebastian, and A. Pantazi " High-speed multiresolution scanning probe microscopy based on Lissajous scan trajectories," *Nanotechnology*, vol. 23, 185501, 2012.
- [19] B. Song, N. Xi, R. Yang, K. Wai, C. Lai, and C. Qu, "On-line sensing and visual feedback for atomic force microscopy (AFM) based nano-manipulations," *2010 IEEE Nanotechnology Materials and Devices Conference (NMDC)*, vol., no., pp.71,74, 12-15 Oct. 2010.
- [20] P. I. Chang, H. Peng, J. Maeng, and S. B. Andersson, "Local raster scanning for high-speed imaging of biopolymers in atomic force microscopy," *Review of Scientific Instruments* , vol.82, no.6, pp.063703,063703-7, Jun 2011.
- [21] G. Li, Y. Wang, and L. Liu, "Drift Compensation in AFM-Based Nanomanipulation by Strategic Local Scan," *IEEE Transactions on Automation Science and Engineering*, vol.9, no.4, pp.755,762, Oct. 2012.
- [22] Hui Xie and S. Régnier, "High-Efficiency Automated Nanomanipulation With Parallel Imaging/Manipulation Force Microscopy," *IEEE Transactions on Nanotechnology*, vol.11, no.1, pp.21,33, Jan. 2012.
- [23] Jim-Wei Wu, Kuan-Chia Huang, Ming-Li Chiang, Mei-Yung Chen, and Li-Chen Fu, "Modeling and Controller Design of a Precision Hybrid Scanner for Application in Large Measurement-Range Atomic Force Microscopy," *IEEE Transactions on Industrial Electronics*, In press.

- 
- [24] J. Curie and P. Curie, "Développement, par pression, de l'électricité polaire dans les cristaux hémicèdres à faces inclinées," *Comptes rendus*, vol. 91, pp. 294-295, 1880.
- [25] P. J. Chen and S. T. Montgomery, "A macroscopic theory for the existence of the hysteresis and butterfly loops in ferroelectricity," *Ferroelectrics*, vol. 23, pp. 199-207, 1980.
- [26] Y.-K. Wen, "Method for Random Vibration of Hysteretic Systems," *Journal of the Engineering Mechanics Division*, vol. 102, pp. 249-263, 1976.
- [27] M. J. Todd and K. L. Johnson, "A model for coulomb torque hysteresis in ball bearings," *International Journal of Mechanical Sciences*, vol. 29, pp. 339-354, 1987.
- [28] B. D. Coleman and M. L. Hodgdon, "A constitutive relation for rate-independent hysteresis in ferromagnetically soft materials," *International Journal of Engineering Science*, vol. 24, pp. 897-919, 1986.
- [29] F. Preisach, "Über die magnetische Nachwirkung," *Zeitschrift für Physik A Hadrons and Nuclei*, vol. 94, pp. 277-302, 1935.
- [30] M. Goldfarb and N. Celanovic, "Modeling piezoelectric stack actuators for control of micromanipulation," *IEEE Transactions on Control Systems*, vol. 17, pp. 69-79, 1997.
- [31] E.-T. Hwu, K.-Y. Huang, S.-K. Hung, and I.-S. Hwang, "Measurement of Cantilever Displacement Using a Compact Disk/Digital Versatile Disk Pickup Head," *Japanese Journal of Applied Physics*, vol. 45, pp. 2368-2371, 2006.
- [32] P. K. Hansma, J. P. Cleveland, M. Radmacher, D. A. Walters, P. E. Hillner, M. Bezanilla, M. Fritz, D. Vie, H. G. Hansma, C. B. Prater, J. Massie, L. Fukunaga, J. Gurley, and V. Elings, "Tapping mode atomic force microscopy in liquids," *Applied Physics Letters*, vol. 64, pp. 1738-1740, 1994.
- [33] B. Francis and W. Wonham, "The internal model principle of control theory," *Automatica*, vol. 12, pp. 457-465, 1976.
- [34] Y.-S. Lu, "Sliding-Mode Disturbance Observer with Switching-Gain Adaptation and Its Application to Optical Disk Drives," *IEEE Transactions on Industrial Electronics*, vol.56, no.9, pp.3743-3750, Sept. 2009.
- [35] S. Galeani, L. Menini, and A. Potini, "Robust Trajectory Tracking for a Class of Hybrid Systems: An Internal Model Principle Approach," *IEEE Transactions on Automatic Control*, vol.57, no.2, pp.344-359, Feb. 2012.
- [36] R. Doraiswami and L. Cheded, "Kalman filter for parametric fault detection: an internal model principle-based approach," *IET Control Theory & Applications*, vol.6, no.5, pp.715-725, March 15 2012.

- 
- [37] S. Polit, and J. Dong, "Development of a High-Bandwidth XY Nanopositioning Stage for High-Rate Micro-/Nanomanufacturing," *IEEE/ASME Transactions on Mechatronics*, vol.16, no.4, pp.724,733, Aug. 2011.
- [38] P. R. Dahl, and R. Wilder, "Math model of hysteresis in piezoelectric actuators for precision pointing system," in *Proceedings of the Eighth Annual Rocky Mountain Conference*. Keystone, CO, UNITED STATES: Guidance and control 1985, Feb 1985, pp. 61–88.
- [39] B. Cappella and G. Dietler, "Force-distance curves by atomic force microscopy," *Surface Science Reports*, vol. 34, pp. 1-104, 1999.
- [40] B. V. Derjaguin, V. M. Muller, and Y. P. Toporov, "Effect of contact deformations on the adhesion of particles," *Journal of Colloid and Interface Science*, vol. 53, pp. 314-326, 1975.
- [41] J. N. Israelachvili, *Intermolecular and surface forces / Jacob N. Israelachvili*. London ; San Diego: Academic Press, 1991.
- [42] S. Ciraci, E. Tekman, A. Baratoff, and I. P. Batra, "Theoretical study of short- and long-range forces and atom transfer in scanning force microscopy," *Physical Review B*, vol. 46, pp. 10411-10422, 1992.
- [43] 范光照 and 張郭益, "精密量測, 5th ed.," 高立, 2007.
- [44] C. D. Frank, "High-resolution, high-speed, low data age uncertainty, heterodyne displacement measuring interferometer electronics," *Measurement Science and Technology*, vol. 9, p. 1024, 1998.
- [45] L.-S. Chen, "Servo System Design and Analysis for Fabricating Large Area Sub-Micron-Period Interference Gratings," MS, NTU, 2008.
- [46] A. Bazaie, Y. K. Yong, and S. O. Reza Moheimani, "High-speed Lissajous-scan atomic force microscopy: Scan pattern planning and control design issues," *REVIEW OF SCIENTIFIC INSTRUMENTS*, 83, 063701 2012.
- [47] S. Moon, S-W Lee, M. Rubinstein, Brian J. F. Wong, and Z. Chen, "Semi-resonant operation of a fiber-cantilever piezotube scanner for stable optical coherence tomography endoscope imaging," *Opt. Express*, 18, 21183, 2010.
- [48] S. A. Hojjatoleslami and J. Kittler, "Region Growing: A New Approach," *IEEE TRANSACTIONS ON IMAGE PROCESSING*, VOL. 7, NO. 7, 1998.
- [49] P. A. Ioannou and J. Sun, *Robust adaptive control*: PTR Prentice-Hall, 1996.
- [50] Kuan-Lin Hung, Yuan-Zhi Peng, Jim-Wei Wu, Mei-Yung Chen, and Li-Chen Fu, "Design and implementation of an electromagnetically damped positioner with flexure suspension," *2011 IEEE International Conference on Control Applications (CCA)*, , 2011, pp. 1062-1067.

- 
- [51] J.-P. Su and C.-C. Wang, "Complementary sliding control of non-linear systems," *International Journal of Control*, vol. 75, pp. 360-368, 2002/01/01 2002.
- [52] S.-J. Huang, K.-S. Huang, and K.-C. Chiou, "Development and application of a novel radial basis function sliding mode controller," *Mechatronics*, vol. 13, pp. 313-329, 2003.
- [53] M. Chen and W.-H. Chen, "Sliding mode control for a class of uncertain nonlinear system based on disturbance observer," *International Journal of Adaptive Control and Signal Processing*, vol. 24, pp. 51-64, 2010.

List of Publication



➤ International Journal

[1] Jim-Wei Wu, Kuan-Chia Huang, Ming-Li Chiang, Mei-Yung Chen, and Li-Chen Fu, "Modeling and Controller Design of a Precision Hybrid Scanner for Application in Large Measurement-Range Atomic Force Microscopy," *IEEE Transactions on Industrial Electronics*, (SCI) (accepted)

[2] Jim-Wei Wu, Jyun-Jhih Chen, Ming-Li Chiang, Jen-Te Yu, and Li-Chen Fu, "Design and Control of Phase-Detection Mode Atomic Force Microscopy for Reconstruction of Cell Contours in Three-Dimensions," *IEEE Transactions on Nanotechnology*, (SCI) (submitted)

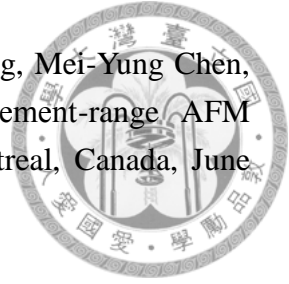
[3] Chih-Lieh Chen, Jim-Wei Wu, Yi-Ting Lin, Li-Chen Fu, and Mei-Yung Chen, "Precision Sinusoidal Local Scan for Large Range Atomic Force Microscopy with Auxiliary Optical Microscopy," *IEEE Transactions on Mechatronics*, (SCI) (submitted)

➤ International Conference

[1] Chih-Lieh Chen, Jim-Wei Wu, Yi-Ting Li, and Li-Chen Fu, "Precision Sinusoidal Local Scan for Large Range Atomic Force Microscopy with Auxiliary Optical Microscopy," *Proc. of 52nd IEEE Conference on Decision and Control*, Hawaii, USA, Dec. 10-13, 2013 (accepted)

[2] Jim-Wei Wu, Jyun-Jhih Chen, Kuan-Chia Huang, Chih-Lieh Chen, Yi-Ting Lin, Mei-Yung Chen, and Li-Chen Fu, "Design and Control of Phase-Detection Mode Atomic Force Microscopy for Cells Precision Contour Reconstruction under Different Environments," *Proc. of American Control Conference*, Washington DC, USA, June 17-19, 2013

[3] Kuan-Chia Huang, Jim-Wei Wu, Jyun-Jhih Chen, Chih Lieh Chen, Mei-Yung Chen, and Li-Chen Fu, "Development of a large scanning-range atomic force microscope with adaptive complementary sliding mode controller," *Proc. of 51st IEEE Conference on Decision and Control*, Hawaii, USA, Dec. 10-13, 2012.



[4] Jim Wei Wu, Yuan-Zhi Peng, Jyun-Jhih Chen, Kuan-Chia Huang, Mei-Yung Chen, Li-Chen Fu, “Design and Implementation of a Large Measurement-range AFM Scanning System,” *Proc. of American Control Conference*, Montreal, Canada, June 27-29, 2012

[5] Yuan-Zhi Peng, Jim-Wei Wu, Kuan-Chia Huang, Jyun-Jhih Chen, Mei-Yung Chen, and Li-Chen Fu, “Design and Implementation of an Atomic Force Microscope with Adaptive Sliding Mode Controller for Large Image Scanning,” *Proc. of 50th IEEE Conference on Decision and Control*, Orlando, Florida, USA, December 12-15, 2011.

[6] Kuan-Lin Huang, Yuan-Zhi Peng, Jim-Wei Wu, Mei-Yung Chen, and Li-Chen Fu, “Design and Implementation of an Electromagnetically Damped Positioner with Flexure Suspension,” *Proc. of IEEE Multi-Conference on Systems and Control*, Denver, USA, September 28-30, 2011.

[7] Jim-Wei Wu, Mei-Yung Chen, Shao-Kang Hung, Li-Chen Fu, “A Compact Tapping Mode AFM with Sliding Mode Controller for Precision Image Scanning,” *Proc. of 8th Asian Control Conference*, Kaohsiung, Taiwan, May 15-18, 2011.

[8] Shan-Tsung Lee, Kuan-Lin Huang, Jim-Wei Wu, and Li-Chen Fu, “Design and Control of Long Travel Range Electromagnetically Actuated Positioning Stage with Application to Precise Machining,” *Proc. of IEEE Multi-Conference on Systems and Control*, pp.2219-2224, Yokohama, Japan, September, 8-10, 2010.

[9] Shih-Hsun Yen, Jim-Wei Wu, and Li-Chen Fu, “Apply Tapping Mode Atomic Force Microscope with CD/DVD Pickup Head in Fluid,” *Proc. of American Control Conference*, pp. 6549-6554, Baltimore, MD, U.S.A., June 30-July 2, 2010.